Diss. ETH No.

PHYSICAL AND CHEMICAL CHARACTERIZATION OF NON-VOLATILE AIRCRAFT ENGINE EXHAUST

A dissertation submitted to ETH Zurich for the degree of Doctor of Sciences

Presented by

Manuel Abegglen, MSc

Born 17 March 1983

Citizen of Iseltwald (BE), Switzerland

Accepted on the recommendation of

Prof. Dr. Ulrike Lohmann, examiner

Dr. Andreas Petzold, co-examiner

Dr. Berko Sierau, co-examiner

2016

ABSTRACT

Soot particles, formed by incomplete combustion of hydrocarbon fuels, affect the global radiation budget directly due to their strong light-absorbing nature and indirectly by interacting with clouds as cloud condensation nuclei and ice nucleating particles, consequently altering climate. Both the direct and the indirect effect result in radiative forcing components important to predict global warming. Moreover, these particles pose a risk to human health upon inhalation. These climate and health effects strongly depend on the physical and chemical properties of the soot particles such as size, mass, density, morphology, aerosol mixing state and chemical composition. Soot particles consist of chain-like fractal coagulations of small, nearly spherical particles, which are referred to as primary particles. Hence, the morphology of soot agglomerates depends on the number and size of the primary particles as well as on the degree of compaction. Fractal particles are described by the effective density and the fractal dimension. This thesis aims to provide information on unaltered, fresh soot particles emitted over the entire operating range by different aircraft engines using experimental research focusing on their physical and chemical characterization. Aircraft emissions are an important anthropogenic source of soot particles near airports and in the upper troposphere where most of them are emitted.

The measurements on aircraft soot were conducted in the framework of the Aviation Particulate Regulatory Instrumentation Demonstration Experiment (A-PRIDE) campaigns. These campaigns were initiated in the course of the development of a new International Civil Aviation Organization (ICAO) certification standard for aircraft engine particulate matter exhaust. The experiments were performed at the Zurich Airport in an aircraft turbine test facility not usually accessible for research. They offered a rare opportunity to sample and study aircraft engine combustion products directly after emission, with data collected over the entire operating range of the engines. Observations were made using an Aerosol Time-of-Flight Mass Spectrometer (ATOFMS) and a Centrifugal Particle Mass Analyzer (CPMA).

The ATOFMS provides information on the chemical composition of single particles and their aerodynamic size. The measurements performed during the A-PRIDE campaigns are the first comprehensive mass spectrometric measurements on individual freshly

emitted exhaust particles from aircraft engines. The recorded data was used to gain a more complete picture of the mixing state of the particles and to identify different particle compositions. The CMPA classifies particles according to their mass-to-charge ratio. The combined knowledge on mass and size of the soot particles allows to determine their effective density and mobility-based fractal dimension.

Depending on engine type, 94.5 % to 97.5 % of the particles contained elemental carbon, with elemental carbon to total carbon ratios ranging from 0.83 to 0.99. Since the ATOFMS is able to resolve refractory material, it was possible to detect metallic compounds present in the exhaust. All detected metals were found to be internally mixed with the soot particles, and more than 36 % of the analyzed particles contained at least one metallic compound. The occurrence of metallic compounds is important because some have found to improve the particle's ability to act as cloud condensation nuclei and ice nucleating particles. In addition, they probably affect the toxicity of aerosol particles, with implications for human health. The detected metallic elements were Cr, Fe, Mo, Na, Ca, Al, V, Ba, Co, Cu, Ni, Pb, Mg, Mn, Si, Ti and Zr. These results suggest that aircraft engine emissions are a considerable source of potential ice nucleating particles in the upper troposphere.

Investigations were made in order to identify and/or exclude potential sources of metallic compounds inside the engine, which would assist in reducing the emission of metallic compounds. To do so samples were collected from kerosene and lubricant oil as well as debris from wearing components, which were considered as potential sources, and then quantitatively analyzed using Inductively Coupled Plasma Mass Spectrometry (ICP-MS). Many of these elements were detected in multiple samples, making an unambiguous source assignment impossible. Therefore, the metals were assigned to their probable sources based on their concentrations in the samples and their appearance in the engine. Only Co and Zr were not found in both the kerosene and lubricant oil and could therefore be clearly assigned to wearing engine components. Thus, they can probably serve as tracers for Particulate Matter (PM) aircraft engine emissions.

The PM emission from a widely used aircraft engine was investigated using the CPMA. These measurements were the first comprehensive dataset of particle mass values, enabling the description of the particle morphology over the entire operating range of this aircraft engine. At constant engine thrust, the effective density decreased with increasing particle size and generally increased with increasing thrust. For particles with a mobility size (d_m) of 30 nm and 75 nm, it ranged from 1075 kg/m^3 to 1490 kg/m^3 and

530 kg/m^3 to 1020 kg/m^3 respectively. Measurements of particles larger than 100 nm were only possible at thrusts ≥67 %, due to the lack these particle sizes at lower thrust, and the effective density approached ~800 kg/m^3 for d_m = 150 nm. The fractal dimension can be derived from the change of the effective density with particle size. The fractal dimensions obtained from our measurements ranged from 1.85 to 2.32 for thrust levels <30 % and from 2.54 to 2.79 for thrust levels >30 %, which implies more closely packed soot agglomerates at higher engine thrust. The measured effective densities and fractal dimensions were further compared to values obtained for exhaust particles emitted by a different engine type. These values were recorded earlier with a similar experimental set-up in the same test cell at the Zurich Airport published by Johnson et al. (2015).

Using the effective density and the measured particle size distribution, PM mass concentrations at the instruments and the total PM mass emissions at the engine exit were estimated. The estimates of the PM mass concentrations were in good agreement with values obtained using the widely assumed unit density (1000 kg/m^3) as well as with real-time black carbon mass measurements. Thus, for this engine, the unit particle density is a good approach to convert the measured particle size distributions into PM mass. The measured effective density distribution and the unit density were further used to predict PM mass losses in the sampling system. Line losses are important to determine the PM mass emission actually emitted which is crucial for climate and air quality models. The loss of PM mass predicted using the effective density distribution was ~60 % at idle and decreased to ~27 % for thrust ≥80 %. Compared to the predicted PM loss using unit density, these values were within 20 % and 5 % at idle and high thrust, respectively. The results could be used in the future ICAO emission database.

ZUSAMMENFASSUNG

Russpartikel, welche durch unvollständige Verbrennung von Kohlenwasserstoffbrennstoffen entstehen, beeinflussen direkt das globale Strahlungsgleichgewicht der Erde aufgrund ihrer ausgeprägten Eigenschaft, Licht zu absorbieren, und indirekt durch ihre Interaktion mit Wolken, was in der Folge das Klima beeinflusst. Der direkte und der indirekte Effekt resultieren in Strahlungsantriebskomponenten, welche wichtig sind, die globale Erwärmung vorauszusagen. Darüber hinaus stellen diese Partikel ein Risiko für die Gesundheit dar, wenn sie eingeatmet werden. Die Auswirkungen auf das Klima und die Gesundheit hängen stark von den physikalischen und chemischen Eigenschaften der Russpartikel wie Grösse, Masse, Dichte, Morphologie, Mischungszustand des Aerosols und chemische Zusammensetzung ab. Rußpartikel sind fraktale Aggregate, bestehend aus kettenartigen Strukturen, welche sich wiederum aus koagulierten, kleinen und nahezu kugelförmigen Partikeln, den sogenannten Primärpartikeln, zusammensetzen. Daher hängt die Morphologie von Russagglomeraten von der Anzahl und Größe der Primärpartikel sowie dem Grad der Verdichtung ab. Fraktale Partikel werden mit der effektiven Dichte und der fraktalen Dimension beschrieben. Die vorliegende Arbeit liefert mittels experimenteller Forschung Informationen über physikalische und chemische Eigenschaften von in verschiedenen Flugzeugturbinen über deren gesamten Betriebsbereich frisch emittierten Russpartikel. Flugzeugemissionen sind eine wichtige Quelle von Russpartikel in der Nähe von Flughäfen und in der oberen Troposphäre, wo die meisten ausgestossen werden.

Die Messungen der Flugzeugabgase wurden im Rahmen der Aviation Particulate Regulatory Instrumentation Demonstration Experiment (A-PRIDE) Kampagnen durchgeführt. Diese Kampagnen wurden im Zuge der Entwicklung eines neuen ICAO (International Civil Aviation Organization) Zertifizierungsstandards für Feinstaub im Abgas von Flugzeugtriebwerken ins Leben gerufen. Die Experimente wurden am Flughafen Zürich in einer Testzelle für Flugzeugturbinen durchgeführt, welche normalerweise nicht für die Forschung zugänglich ist. Sie boten eine seltene Gelegenheit, Verbrennungsprodukte von Flugzeugtriebwerken direkt nach ihrer Emission zu sampeln und zu studieren. Die Daten wurden über den gesamten Betriebsbereich bezüglich der Schubleistung der Triebwerke aufgenommenen. Dazu wurden ein Einzelpartikel Flugzeitmas-

senspektrometer (ATOFMS) und ein Zentrifugal Partikelmassen Analysegerät (CPMA) verwendet.

Das ATOFMS liefert Informationen über die chemische Komposition einzelner Partikel und deren aerodynamischen Grössen. Die während der A-PRIDE Kampagnen durchgeführten Messungen sind die ersten umfassenden massenspektrometrischen Messungen von einzelnen, frisch ausgestoßenen Abgaspartikel von Flugzeugtriebwerken. Die aufgenommenen Daten wurden benutzt, um ein vollständigeres Bild über den Mischzustand der Partikel zu gewinnen und um verschiedene Partikelzusammensetzungen zu identifizieren. Der CPMA klassiert Partikel nach ihrem Masse-zu-Ladung Verhältnis. Das kombinierte Wissen über Masse und Grösse der Russpartikel erlaubt, die effektive Dichte und die mobilitätsbasierende fraktale Dimension zu bestimmen.

Je nach Turbinentyp enthielten 94,5 % bis 97,5 % der Partikel elementaren Kohlenstoff und das Verhältnis von elementarem zu totalem Kohlenstoff betrug zwischen 0,83 und 0,99. Da das ATOFMS hitzebeständiges Material messen kann, war es möglich metallische Verbindungen im Abgas zu identifizieren. Alle gefundenen Metalle waren intern gemischt mit den Russpartikeln und mindestens 36 % der untersuchten Partikel enthielten wenigstens eine metallische Verbindung. Kenntnis über das Auftreten von Metallverbindungen in Aerosolpartikel ist wichtig, weil gezeigt wurde, dass einige Metalle dazu beitragen, dass sich die Fähigkeit der Partikel erhöht, als Wolkenkondensationskeime und Eiskeime zu agieren. Darüber hinaus haben metallische Verbindungen wahrscheinlich Einfluss auf die Toxizität von Aerosolpartikel. Die detektierten metallischen Elemente waren Cr, Fe, Mo, Na, Ca, Al, V, Ba, Co, Cu, Ni, Pb, Mg, Mn, Si, Ti und Zr. Diese Ergebnisse legen nahe, dass Flugzeugmotoremissionen eine beträchtliche Quelle potentieller Eiskeime in der oberen Troposphäre darstellen.

Untersuchungen wurden gemacht, um die gefundenen metallischen Verbindungen ihren entsprechenden Quellen in der Turbine zuzuordnen. Dies ist relevant, um die Emissionen von Metallverbindungen zu reduzieren. Dazu wurden Proben von Kerosin, Getriebeöl und Ablagerungen von Turbinenverschleisskomponenten, welche als potentielle Quelle betrachtet werden, gesammelt. Diese Proben wurden dann mittels quantitativer induktiv gekoppelter Plasma-Massenspektrometrie (ICP-MS) untersucht. Viele dieser Elemente konnten in zwei oder sogar allen drei Proben festgestellt werden, was eine eindeutige Zuordnung verunmöglichte. Daher wurden die Metalle aufgrund ihrer Konzentrationen in den Proben und ihrem Vorkommen in der Turbine ihren wahrscheinlichen Quellen zugeordnet. Einzig Co und Zr wurden weder im Kerosin noch im

Getriebeöl gefunden und konnten daher eindeutig den Verschleisskomponenten im Triebwerk zugewiesen werden. Somit können Co und Zr wahrscheinlich als Tracer für Feinstaub aus Triebwerksemissionen herangezogen werden.

Die Feinstaubemissionen einer weit verbreiteten Flugzeugturbine wurden mit dem CPMA untersucht. Aus diesen Messungen resultierte der erste umfassende Datensatz von Werten, welche wichtig sind, um die Morphologie von emittierten Rußpartikel über den gesamten Leistungsbereich dieser Flugzeugturbine zu beschreiben. ==Bei konstanter Schubleistung nahm die effektive Dichte mit zunehmender Partikelgrösse ab.== Für eine bestimmte Partikelgrösse nahm die effektive Dichte mit zunehmender Schubleistung generell zu. Für Partikel mit einem Mobilitätsdurchmesser (d_m) von 30 nm reichte sie von 1075 kg/m^3 bis 1490 kg/m^3 und für Partikel $d_m = 75$ nm von 530 kg/m^3 bis 1020 kg/m^3. Messungen von Partikel mit $d_m \geq 100$ nm konnten nur bei einer Schubleistung $\geq 67\%$ gemacht werden und die effektive Dichte für Partikel mit $d_m = 150$ nm näherte sich einem Wert von ~800 kg/m^3. Die fraktale Dimension kann aus der Änderung der effektiven Dichte mit der Partikelgröße abgeleitet werden. Die aus unseren Messungen errechneten Werte der fraktalen Dimensionen lagen zwischen 1,85 und 2,32 bei einer Schubleistung <30 % und zwischen 2,54 und 2,79 bei höherer Schubleistung, dies deutet auf generell kompaktere Russagglomerate bei höherem Schub hin. Ferner wurden die gemessenen effektiven Dichten und fraktalen Dimensionen mit Werten verglichen, welche für Abgaspartikel eines anderen Turbinentyps ermittelt wurden. Diese Werte wurden zu einem früheren Zeitpunkt mit einem ähnlichen Versuchsaufbau in der gleichen Testzelle am Flughafen Zürich gemessen und durch Johnson et al. (2015) veröffentlicht.

Die effektive Dichte und die Partikelgrößenverteilungen wurden verwendet, um die Feinstaubmassenkonzentrationen bei den Instrumenten und die Gesamtmasse der Feinstaubemissionen hinter der Turbine abzuschätzen. Die geschätzten Werte der Feinstaubmassenkonzentrationen waren in guter Übereinstimmung mit den Werten, die unter Verwendung der weithin angenommen Einheitsdichte (1000 kg/m^3) sowie mit Echtzeitmessungen der Russmasse ermittelt wurden. Für diese Turbine ist die Einheitsdichte somit ein guter Ansatz, um die gemessenen Partikelgrößenverteilungen in Feinstaubmasse umzurechnen. Die gemessene Verteilung der effektiven Dichten und die Einheitsdichte wurden weiter verwendet, um Massenverluste des Feinstaubs im Probenahmesystem vorherzusagen. Verluste im Probenahmesystem sind wichtig, um die Emissionen hinter der Turbine zu bestimmen, was entscheidend für Modelle ist,

welche Luftqualität und Klima berechnen. Der vorhergesagte Verlust der Feinstaubmasse betrug ~60 % im Bodenleerlauf und sank auf ~27 % bei einer Schubleistung ≥80 %. Im Vergleich zu dem vorhergesagten Verlust mittels der Einheitsdichte waren diese Werte innerhalb von 20 % für Bodenleerlauf und 5 % bei hohen Schubleistungen. Diese Ergebnisse könnten in der zukünftigen ICAO Emissionsdatenbank verwendet werden.

TABLE OF CONTENTS

LIST OF FIGURES

LIST OF TABLES

ABBREVIATIONS AND SYMBOLS

AFL	Aerodynamic focussing lens
AFR	Air-to-fuel ratio
APC	AVL particle counter
APM	Aerosol particle mass analyzer
A-PRIDE	Aviation particle regulatory instrumentation demonstration experiment
ATOFMS	Aerosol time-of-flight mass spectrometer
BC	Black carbon
eBC	Equivalent black carbon mass concentration
rBC	Refractory black carbon mass concentration
CCN	Cloud condensation nuclei
CPC	Condensation particle counter
CPMA	Centrifugal particle mass analyzer
CS	Catalytic stripper
DMA	Differential mobility analyser
EC	Elemental carbon
EEPS	Engine exhaust particle sizer
EI_m	Mass-based emission indices
ENCHILADA	Environmental chemistry through intelligent atmospheric data analysis
FMPS	Fast mobility particle sizer
FOCA	Federal office of civil aviation
GI	Ground idle
GMD	Geometric mean diameter
GSD	Geometric standard deviation
ICAO	International civil aviation organization
ICP-MS	Inductively coupled plasma mass spectrometry
INP	Ice nucleating particle
(I)PSD	(Integrated) Particle size distribution
ISA	International standard atmosphere
MSS	Micro soot sensor
OC	Organic carbon
(nv)PM	(Non-volatile) Particulate matter
PMT	Photomultiplier tube
PSL	Polystyrene latex
PTFE	Polytetrafluoroethylene
RF	Radiative forcing

RH	Relative humidity
SMPS	Scanning mobility particle sizer
T	Temperature
TC	Total carbon
TEM	Transmission electron microscopy
TPM	Total particulate matter mass concentration
TRD	Time resolved data
UTRC	United technologies research center
VMD	Volume median diameter
WU	Warm-up
C	Mass-mobility prefactor
C'	Density-mobility prefactor
D_f	Fractal dimension
D_m	Mobility-based fractal dimension *or* mass-mobility scaling exponent
d	Particle diameter
d_m	Electrical mobility diameter
d_{pp}	Diameter of primary particle
d_{va}	Particle vacuum aerodynamic diameter
F_c	Centrifugal force
F_e	Electrostatic force
m_p	Particle mass
m/z	Mass to charge ratio
N_{pp}	Number of primary particles
ε	Mass-mobility exponent
λ	Wavelength
ρ_0	Unit density
ρ_{eff}	Effective density
ρ_p	Particle density
ω	Angular speed
χ_v	Dynamic shape factor in the vacuum or free molecular regime

1 INTRODUCTION

1.1 Atmospheric aerosol

The term aerosol is defined as a two-phase system consisting of solid and/or liquid particles suspended in the surrounding gaseous medium. The aerosol particles are synonymously termed Particulate Matter (PM). Depending on the source, it is divided into primary and secondary PM. Primary PM is directly emitted into air and originates mainly from combustion and fragmentation processes such as wind-driven suspension of dust into air, sea spray and volcanic eruptions, whereas secondary PM is formed in the air due to gas-to-particle conversion (Lushnikov, 2010). Secondary aerosol particles originate from photochemical and chemical reactions due to oxidation of precursor gases such as organic compounds, sulfur dioxide, dimethyl sulfide (DMS), carbonyl sulfide and other gases (Ivlev, 2010). The oxidized gases can then either condense onto existing particles or nucleate and form new particles. Once a particle is suspended or formed in the air, it grows by condensation of vapors and coagulation with other particles until it is removed by dry deposition due to gravitation or wet deposition due to scavenging. Scavenging includes in-cloud scavenging (rainout) resulting from water condensing onto the particle as well as below-cloud scavenging (washout) due to the interaction with a falling droplet.

Aerosol particles are often characterized by their size, shape and chemical composition. The most important property of a particle governing its transport behavior in a gas is size (Hinds, 1999). Particle sizes typically range from 1 nm (1 nm = 10^{-9} m) to 100 μm (1 μm = 10^{-6} m), and the particles can be classified according to their size. Primary PM comprises relatively larger particles than secondary PM. Two commonly used systems to classify aerosol particles according to their size are mentioned in the following. Junge (1955) introduced a classification according to the particle diameter (d) and defined giant particles, $d \geq 2$ μm; medium particles (also called *Junge* particles), with 0.2 μm $< d < 2$ μm; and small/fine particles (also called *Aitken* particles), with $d \leq 0.2$ μm (Ivlev, 2010). The second classification depicted in Figure 1.1 was suggested by Whitby (1978). It divides particles into 1) coarse mode ($d > 2.5$ μm), accumulation mode (0.1 μm $< d < 2.5$ μm) and nucleation mode ($d < 0.1$ μm) particles. Liquid particles are often quite spherical because they grow by condensation of liquid from the

1

gas phase (Kulkarni et al., 2011). For solid particles however, a wide variety of forms can be observed in the atmosphere such as plates, fibres and chains (Ivlev, 2010). Another shape-based class of particles are the so-called fractal aggregates. Because unaltered particles emitted by aircraft turbines are fractal aggregates (cf. 1.2.2), their nature is discussed in more detail in section 1.2. The chemical components of aerosol particles often comprise a mixture of water-soluble and water-insoluble substances (Pruppacher & Klett, 2010a). The most abundant species are sulfates, nitrates and organics, but chlorides, ammonium, water, carbon and soil dust represent a considerable fraction, too (Jimenez et al., 2009). Sulfates, nitrates and organics are either co-emitted with primary PM or formed via oxidation of gaseous precursors. Precursors for sulfate and nitrate are sulfur dioxide and DMS, and nitrogen dioxide, respectively.
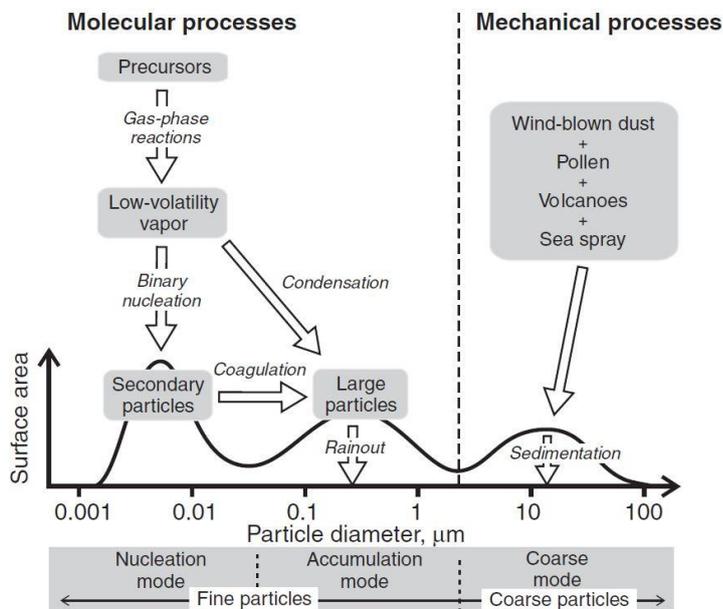
Figure 1.1   Classification of aerosol particles according to their size and the corresponding processes of formation and removal (Lamb & Verlinde, 2011).

Atmospheric aerosol particles are important because they can facilitate the formation and nucleation of cloud droplets and ice crystals, respectively. However, the ability to do so strongly differs among the different aerosol particles. The nucleation of the liquid phase and the solid phase have to be treated separately. They both can occur homogeneously or heterogeneously. In general, nucleation describes the formation of a thermodynamically stable phase within a metastable phase.

Homogeneous nucleation of cloud droplets describes the phase change from vapor to liquid, where the (liquid) cloud droplet forms in the (water) vapor. Water droplet formation starts with a cluster of few water molecules. The vapour pressure over such a small cluster however, is much larger than over a flat surface of water because of the curvature effect, the so-called Kelvin effect. This can explained by the fact, that the vapor pressure is determined by the energy needed to release a water molecule from the bulk phase. This energy is lower over curved surfaces (as this is the case for a small cluster) compared to flat surfaces because the molecules have less neighbour molecules and thus experience less attractive forces. Thus, the formation of cloud droplets by homogenous nucleation of water requires a relative humidity of several hundred percent. Such supersaturations do not exist in the atmosphere and can only be achieved in the laboratory. In the atmosphere, cloud droplet formation usually takes place by hygroscopic growth of soluble material, leading to the deliquescence of the material. This results in the formation of a solution droplet followed by its activation into a cloud droplet (Pruppacher & Klett, 2010b). The aerosol particles that can form cloud droplets are Cloud Condensation Nuclei (CCN) if they are aerosol particles that are able initiate drop formation at supersaturations observed in the atmosphere.

The formation of ice can occur either by freezing of clouds and solution droplets or directly due to the deposition (nucleation) of water vapor to the ice phase. This requires an energy barrier to be overcome. Under atmospheric conditions, this energy barrier is too high in the case of homogeneous deposition nucleation (vapor to solid). Contrary, homogeneous freezing of the liquid phase is more likely to take place than nucleation from the vapor phase because the water molecules in a droplet have a lower entropy and thus the energy barrier to be overcome is lower (Lamb & Verlinde, 2011). The term homogeneous ice nucleation further comprises the freezing of aqueous solution droplets. A solution droplet is an aqueous solution mostly consisting of water and a dissolved salt. The solute causes a lower freezing point due to a change in the water activity. This effect is called the freezing point depression.

Heterogeneous nucleation of ice describes the formation of ice at temperatures higher than it would be required for homogeneous freezing to take place, involving a foreign, non-aqueous phase (Lamb & Verlinde, 2011). An aerosol particle involved in the nucleation of ice is called an Ice Nucleating Particle (INP). Four different possible mechanism exist: immersion freezing, deposition nucleation, contact freezing and condensation freezing. Immersion freezing is the freezing of a cloud droplet with an immersed

INP. This particle then initiates the freezing if the droplet experiences low enough temperatures. Deposition nucleation occurs when water vapor deposits onto a particle as ice. Contact freezing occurs when a supercooled droplet freezes upon collision with an INP. Condensation freezing describes the mechanism where water saturation is reached prior to freezing, i.e. a liquid phase is formed on the INP, which subsequently freezes.

1.2 Soot

Carbon is the element that represents the largest fraction of mass of atmospheric aerosol, however only a minor subset thereof is referred to as soot or Elemental Carbon (EC) (Gelencser, 2004). In this study, the focus is on soot and EC particles and the associated chemical compounds. Soot particles consist of EC and Organic Carbon (OC) (Petzold et al., 2013), and because there is a smooth transition between EC and OC the corresponding definitions are usually operationally derived (Gelencser, 2004). EC is often defined as the solid form of pure carbon that absorbs radiation. Due to this light-absorbing characteristic, the term Black Carbon (BC) is often used. BC has more properties which together makes it unique and thus can be used to distinguish BC from other aerosol particles. BC is refractory and only vaporizes at temperatures ~4000 K; it is insoluble in water, methanol and acetone; and a BC particle is an aggregate of smaller spherules. These spherules are called primary particles. EC mostly is a product of incomplete combustion that occurs if not enough oxygen is available to react with the fuel to form CO_2 and water. OC is a mixture of carbon with other organic elements, e.g. hydrogen and oxygen; it can be co-emitted with BC from incomplete combustion as primary PM or be formed by oxidation from volatile OC as secondary PM.

The term soot is useful to describe carbonaceous particles from combustion processes (Petzold et al., 2013). Herein, the terms Equivalent Black Carbon (eBC) and Refractory Black Carbon (rBC) are also used depending on the instrument applied to measure BC concentrations. eBC concentration is derived from the measured absorption coefficient using a mass absorption coefficient. Because the absorption is not completely caused by BC, Petzold et al. (2013) suggested to refer to eBC instead of BC if data was derived with optical absorption methods. rBC should be reported if incandescence methods were used to determine the concentration; e.g. in Laser Induced Incandescence measurements where the carbon is heated by a laser until the soot particles start to incandesce, which is then measured using detectors. For measurements using Aerosol Time-

of-Flight Mass Spectrometry as in the study presented in section 2, it is recommended to report EC when referring to the carbon content.

1.2.1 Sources and impact of BC on climate and human health

The sources of BC are of both natural and anthropogenic nature. Natural sources are mainly wildfires whereas anthropogenic sources include biomass burning of solid fuel in residential and fossil fuel combustion in diesel engines and industry. The total global emission of BC in the year 2000 was 7.5×10^6 tons (with an uncertainty range of 2.0×10^6 to 28.2×10^6 tons), of which $\sim 63\%$ are from activities related to energy use; and the largest contribution is from open burning of forests and savannas (Bond et al., 2013). In Figure 1.2, the global BC emissions are shown depending on latitude. The most important sources in the northern hemisphere are on- and off-road diesel engines, industrial coal, and biofuel cooking. Diesel engines globally contribute to the transport sector with $\sim 80\%$ (Gelencser, 2004). The amount and the sources of the emissions regionally differ largely and depend on the development status of a country. Coal and biomass contribute to 60–80 % in Asia and Africa whereas in Europe, North and Latin America $\sim 70\%$ are from diesel engines (Bond et al., 2013). In equatorial regions and the southern hemisphere most BC emissions are from open burning including mainly forests and grass- and woodlands, and the fraction of biofuel cooking decreases towards south.
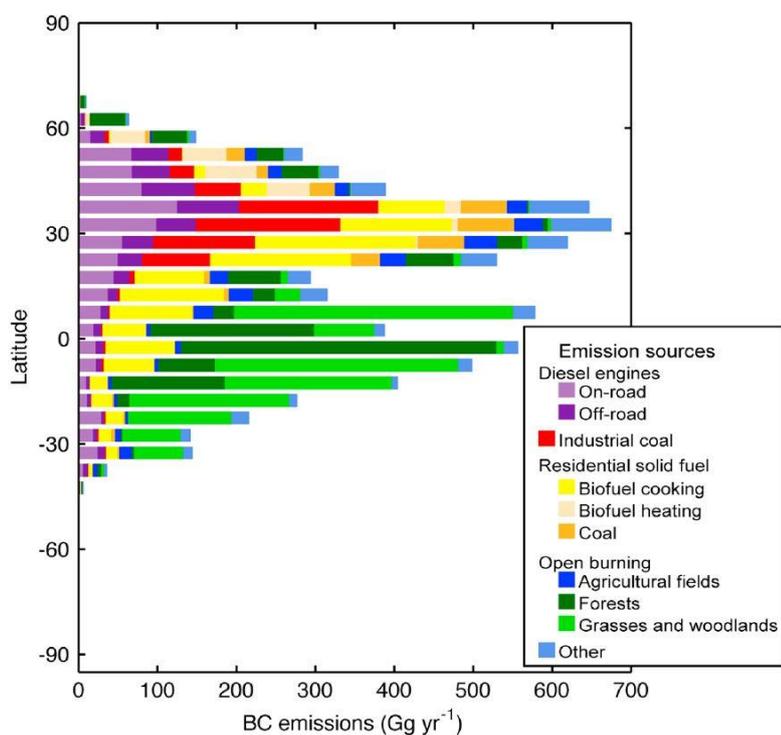
Figure 1.2   Major global BC emission sources by latitude (Bond et al., 2013).

BC influences the climate directly by absorbing and scattering solar radiation. In order to describe changes in the global radiation budget due to changes in concentrations of aerosol particles, gases or other factors the term Radiative Forcing (RF) is commonly used. RF is the difference in the radiation budget before and after a change when equilibrium is reached. It is measured in Wm^{-2} and quantified at the tropopause. The values of the RF given in the following correspond to values derived for the industrial era, which takes into account the time between the year 1750 and 2005, and the 90 % uncertainty ranges are given in parenthesis.

Because BC mainly absorbs solar and terrestrial radiation, it warms the surrounding air. Additionally, BC reduces the solar radiation reaching the Earth's surface. These effects are called direct RF. The BC direct RF was estimated to be $+0.71$ Wm^{-2} ($+0.08$ Wm^{-2} to $+1.27$ Wm^{-2}), of which $+0.51$ Wm^{-2} are due to fossil and bio fuel burning; however, the total RF differs regionally and reach values up to ~ 10 Wm^{-2} (Bond et al., 2013).

Furthermore, BC influences clouds and thereby changes their properties and occurrence. These effects are dived into the semi-direct and the indirect radiative effect. Semi-indirect effects have implication on the atmospheric temperature structure due to the warming of the BC-surrounding air leading to changes in cloud distribution (Bond et al., 2013). The indirect radiative effect results from changes in the number of droplets and

ice crystals in the atmosphere. If more particles are present in liquid clouds then consequently more droplets are formed. Due to the limited water content, these droplets are smaller than without the additional particles which may lead to a decrease in precipitation. Such clouds have a higher optical depth and persists for a relatively longer time because precipitation is delayed (IPCC, 2007) leading to a cooling of the Earth's surface. In mixed-phase clouds, additional BC particles can result in more frequent glaciation of the cloud if these particles act as INP and thereby increase precipitation (IPCC, 2007). Bond et al. (2013) estimated the RF from influences of BC on clouds to be $+0.23$ Wm^{-2} (-0.47 Wm^{-2} to $+1.0$ Wm^{-2}).

An additional climate effect of BC results from its deposition on ice- and snow-covered regions resulting in a decrease of the surface albedo in these regions and thus in a warming the Earth's surface. The surface albedo is the value of the ratio of the backscattered radiation to the incoming radiation measured above the area under investigation. Although this is the smallest of the mentioned radiative effects, it still contributes considerably to the total RF with a value of $+0.13$ Wm^{-2} ($+0.04$ Wm^{-2} to $+0.33$ Wm^{-2}) (Bond et al., 2013). The deposition of BC onto snow and ice additionally increases the melting rates of these snow and ice masses important to predict changes in terms of their areas covering the Earth.

BC can directly cause adverse health issues and premature death. Both, physical and chemical properties of BC influence its implications on human health. The smaller the particles are the deeper they are transported into the respiratory system and the less likely they can be removed again. Terzano et al. (2010) pointed out that particles smaller than 100 nm may even enter the blood stream where they can cause diverse harmful effects; e.g. thrombus formation, accumulation in other organs and transport to the brain (Gilmour et al., 2004; Highwood & Kinnersley, 2006). Also, the deposition efficiency of agglomerates was shown to be larger than for spherical particles of the same size (Scheckman & McMurry, 2011). The surface area of a particle plays an important role, too. A soot aggregate (cf. 1.2.2) has a larger surface area than spherical particles of the same mass and thus depends on its morphology. It determines the potential of free radical (associated with cancer) production (Highwood & Kinnersley, 2006) potentially initiated by BC (Knaapen et al., 2004) when a particle is deposited on lung tissue. The chemical composition of BC can alter its influence on health as well. The toxicity of BC was found to vary depending on its source and might mainly be caused by other substances such as trace metals and hydrocarbons in these particles (EPA, 2010; Janssen

et al., 2012). Pagan et al. (2003) for example showed that metals present in aerosol particles such as vanadium, iron, copper and nickel can cause epithelial injuries.

1.2.2 Physical and chemical properties of BC particles

This chapter focusses on physical and chemical properties of BC particles that were investigated and discussed in this thesis. Soot particles are aggregates consisting of primary particles. Figure 1.3 exemplarily shows a freshly emitted soot particle from an aircraft engine. The primary particles can clearly be recognized by their nearly spherical form. The primary particles emerge due to nucleation. They coagulate and form open fractal-like aggregates consisting of branched chain-like structures. Soot particles from other combustion sources can differ in number and size of the primary particles as well as in the degree of compaction. These differences are attributed to variations in the fuel and engine type i.e. combustion technology (Gelencser, 2004). Moreover, changes in agglomerate size and primary particle size are observed for the same engine when changing the applied power (Liati et al., 2014; Vander Wal et al., 2014). When reporting densities of fractal aggregates, the effective density is a convenient quantity because it can be determined experimentally as presented in chapter 3. Effective densities can be derived using a power-law relationship between particle mass and particle electrical mobility size (see section 3.2). A fractal object shows a so-called self-similarity, thus its form contains patterns that repeat themselves at any size-scale. This concept and associated observations in nature is described in detail by Mandelbrot (1982) in the book "The fractal geometry of nature". As soot agglomerates show self-similarity over a certain size scale, this concept can be applied to describe their morphology. For this, the fractal dimension (D_f) is often used (Maricq, 2007; Shapiro et al., 2012). The value of D_f ranges from 1 to 3 where 1 theoretically corresponds to the extreme form of a one-dimensional structure and 3 to a compact sphere (Friedlander, 2000). D_f in that sense is the dimension of the an object that however can have non-integer value. For soot agglomerates, D_f relates the number of primary particles to the radius of gyration (Friedlander, 2000) (cf. 3.2). So broadly speaking, it relates mass to size.
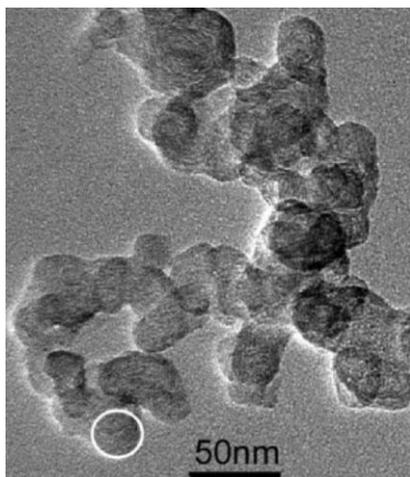
Figure 1.3   Example of a freshly emerged soot particle from an aircraft engine. The white circle indicates a primary particle (Liati et al., 2014).

The morphology of a freshly emerged soot particle is not fixed and may change over time due to atmospheric aging processes that often result in more compact structures (Figure 1.4). For atmospheric aerosol, the aging is a result of oxidation processes (e.g. due to reactions wit OH radicals) as well as condensation or uptake of water (e.g. in cloud processes) and/or secondary PM. It has been showed, for example, that soot particles collapse and lose their chain-like structures if water (which initially condensed onto the particles) evaporates (Ma et al., 2013). Soot agglomerates were also shown to collapse into a more compact form after exposure to sulfuric acid (Zhang et al., 2008). Knowledge on D_f is important to describe the interaction of a soot agglomerate with radiation because more compact particles scatter more light than less compact ones (Zhang et al., 2008).
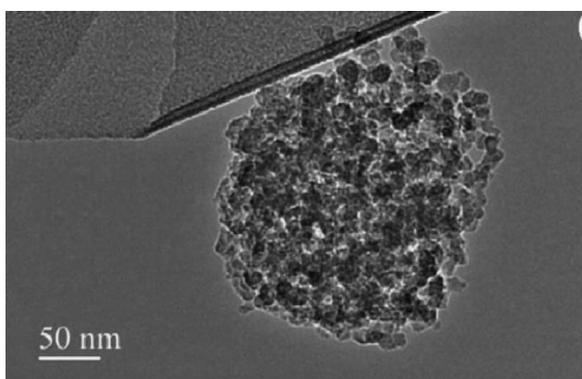
Figure 1.4   Example of a collapsed soot particle from a diffusion burner (Ma et al., 2013).

The state-of-mixing of aerosol particles can be either external or internal. Figure 1.5 illustrates the possible mixing states of a soot particle. An external mixture of aerosol is the coexistence of different particle types in an aerosol of a certain volume whereas an aerosol particle is called internally mixed if two or more PM species form one aerosol particle.

As mentioned, BC consists mainly of EC and OC and might be mixed with other chemical constituents during atmospheric aging. However, depending on its source, the fresh soot particles might already be internally mixed with compounds other than EC and OC, i.e. inorganic matter. Diesel vehicles, for example emit soot particles of which a substantial fraction contain a combination of phosphate, sulfate, calcium and nitrate (Toner et al., 2006), additionally traces of metallic compounds were also detected (Okada et al., 2003). These inorganic compounds are supposed to origin from the fuel, lubricant oil and possibly engine wear. More than 90 % of the soot particles emitted due to the combustion of biomass were shown to be internally mixed with potassium (Silva et al., 1999; Corbin et al., 2015). Potassium is absorbed into woody material as an important plant nutrient where it can remain even after clearing and drying of the plant (Jones et al., 2007). During combustion, it is released into the gas-phase and can condense onto pre-existing soot particles. The chemical composition of soot particles can further influence their ability to act as CCN and INP. However, the ice-nucleating efficiency of soot particles is not yet well understood (Zhou & Penner, 2014).
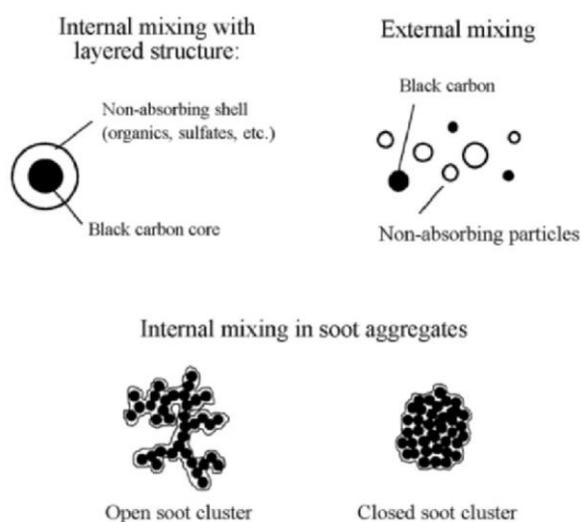
Figure 1.5   Examples of internally and externally mixed soot particles (Martins et al., 1998).

1.2.3 Aircraft turbine PM emissions

BC emitted by aircraft engines have attracted an increased attention over the last few decades because air traffic is steadily growing. The revenue passenger kilometres from commercial air traffic are predicted to increase from 5 billion to 13 billion between 2010 and 2030 (ICAO, 2013). For the year 2006, the estimated fuel used in aviation was ~188 million tons from which >90 % was burned in the northern hemisphere (Wilkerson et al., 2010). Aviation contributes to the global fossil fuel usage with about 2 % to 3 % from which ~80 % can be attributed to civil aviation (IPCC, 1999). Herein, emphasis lays on the associated PM emissions mainly consisting of soot particles. The formation of aircraft soot particles is complex and not well understood because it is influenced by the combustion technology that involves inhomogeneous flow and temperature fields which vary for different engine types (Gelencser, 2004). Thus, it is important to investigate these particles experimentally.

The contribution of aircraft soot emission to the total emitted soot globally by all sources is less than 1 % (Bond et al., 2013). Nevertheless, they represent a unique anthropogenic source of BC in the high altitudes during flight. Also, the emitted particles are important due to their long residence time of 10–15 days in the upper troposphere up to 50 days in the lower stratosphere combined with their impacts on radiation and the potential to act as INP (Kärcher et al., 1996; Gelencser, 2004).

Soot particles emitted by aircraft engines impact the Earth's climate in different ways. In addition to the direct radiative effect, they can form condensation trails (contrails) which alter the radiation budget. The commonly observed linear contrails form just behind the engine. A global linear contrail coverage of 0.07 % was reported by Duda et al. (2013) for the year 2006 but varies depending on region; a value of 0.5 % was given for central Europe during daytime (IPCC, 1999). The linear contrail coverage was modelled to increase by a factor between 3 and 9 between 1992 and 2050 depending on the assumed growth of air traffic (IPCC, 1999). Linear contrail form due to the emissions of heat and water vapor by the aircraft. Depending on the ambient and exhaust temperature, humidity and mixing processes water vapor condenses onto a fraction of the emitted particles due to the cooling of the exhaust stream. Subsequently, droplets freeze if the temperature is sufficiently low. Linear contrails result in a positive radiative forcing due to their small vertical extent and their occurrence in high altitudes. There, they mainly absorb terrestrial infrared radiation and reflect only a small fraction of the incoming solar radiation back to space. Whether a contrail persist depends on ambient

relative humidity with respect to ice (Heymsfield et al., 2010). Persisting contrails can spread horizontally and thereby lose their initial shape and may even become indistinguishable from natural cirrus clouds. This process of cirrus formation is known as induced cirrus cloudiness (Burkhardt & Kärcher, 2011), and it is not well understood and poorly described in climate models (Heymsfield et al., 2010). As shown in Figure 1.6, induced cirrus cloudiness causes the largest radiative forcing effect among all aviation-caused RF components. The combined contribution from soot aerosol and linear contrail to total aviation including induced cirrus cloudiness derived from the best estimates is in the order of ~13 % whereas includes cirrus cloudiness contributes with ~30 %.

In addition, the emitted soot particles can influence natural cirrus cloud properties if they act as INP (Burkhardt & Kärcher, 2011; Hendricks et al., 2011). Cziczo et al. (2013) showed that a dominant fraction of Ice Residuals (IR) collected in cirrus clouds contain metal compounds such as sodium, potassium, copper, lead and iron which implies that these compounds can enhance the efficiency of soot particles to act as INP. This process can also take place in the absence of contrail formation (Kärcher et al., 2007). If heterogeneous freezing is initiated by the additional INP the water content will decrease because the ice particles grow by the uptake of water vapor (IPCC, 1999) inhibiting homogeneous freezing of the background aerosol particles. This leads to changes in optical properties of the affected clouds and delays of freezing onsets (Burkhardt & Kärcher, 2011). However, not sufficient observations exist yet to quantify this impact on radiative forcing (IPCC, 1999), and thus it is not included in Figure 1.6.

Aviation Radiative Forcing Components in 2005

RF Terms		(W m⁻²)	Spatial scale	LOSU
Carbon dioxide		**0.0280** (0.0253)	Global	High
NOₓ — Ozone production		**0.0263** (0.219)	Continental to hemispheric	Med -Low
NOₓ — Methane reduction		**-0.0125** (-0.0104)	Global	Med -Low
Total NOₓ		**0.0138** (0.0115)	Global	Med -Low
Water vapour		**0.0028** (0.0020)	Hemispheric to global	Low
Sulphate aerosol		**-0.0048** (-0.0035)	Local to global	Low
Soot aerosol		**0.0034** (0.0025)	Local to global	Low
Linear contrails		**0.0118** (0.010)	Local to continental	Low
Induced cirrus cloudiness		**0.033**	Local to hemispheric	Very Low
Total aviation (Excl. induced cirrus)		**0.055** (0.0478)	Global	Low
Total aviation (Incl. induced cirrus)		**0.078**	Global	Low

Legend: Best estimate; Estimate; (IPCC AR4 values); 90% confidence

Radiative Forcing (W m⁻²): -0.08, -0.04, 0, 0.04, 0.08, 0.12

Figure 1.6   Radiative forcing components from preindustrial times to 2005. The Level of scientific understanding (LOSU) is shown to the right (Lee et al., 2009).

As pointed out in section 1.2.1, chemical compounds other than carbon in BC particles are probably responsible for impact on human health when inhaled. In addition, size plays an important role. Aircraft soot emissions comprise mainly particles with a diameter well below 100 nm (Petzold & Schröder, 1998; Rogers et al., 2005; Corporan et al., 2008; Herndon et al., 2008; Onasch et al., 2009; Lobo et al., 2015) and contain a substantial fraction of metal-containing particles (see chapter 2). It is therefore not surprising that these particles were shown to cause respiratory health effects (Ferry et al., 2011) in the vicinity of airports (Touri et al., 2013). However, these emissions can cause health effects also on larger spatial scales (Yim et al., 2015).

As the implications of soot particles probably depend on the source, a physical and chemical characterization of soot particles from individual sources on a single particle basis is crucial. Aircraft soot emissions are important because they impact the Earth's climate and human health in several ways. Given the large uncertainties in the radiative forcing components associated with BC, there is the need for further investigations in order to better quantify the involved mechanisms. Aircraft PM emissions are purely anthropogenic and reductions thereof would rapidly result in changes of the associated impacts due to their short life-time compared to greenhouse gases. This makes these

emissions interesting for investigations regarding BC mitigation options with short-term effects. The studies presented in the following focus on aircraft turbine and aim to provide fundamental information on the chemical and physical properties of the associated fresh PM emissions. The emitted soot particles from widely used engine types were investigated experimentally and characterized. The initial morphology of a soot particle is important for its transport behavior and deposition efficiency as well as to predict possible changes of its shape and chemical composition. The chemical composition of a soot particle can influences its toxicity and potentially its ability to act as CCN and INP as well as its optical properties (Zhang et al., 2008). Regarding the physical properties of the soot particles, the presented results provide data on size, fractal dimension and effective density. The effective density was further used to determine PM mass concentrations and to estimate PM mass emissions of the aircraft turbine. The mean effective density was derived in order to estimate particle losses in the used experimental set-up. The chemical composition of the emission is discussed and the identified particle types are described. Emphasis is put on metallic compounds detected in the particles. Additionally, an analysis of the elemental carbon to total carbon ratio of the soot particles is given.

1.3 Measurement campaigns and instrumentation

The measurements presented in this thesis were carried out in the framework of the Aviation Particle Regulatory Instrumentation Demonstration Experiment (A-PRIDE) campaigns. The superior goal of A-PRIDE was to examine and evaluate a new regulatory standard for civil aircraft turbine emissions, which is being developed by the International Civil Aviation Organization (ICAO).

The focus of the measurements discussed herein was to analyze and interpret the obtained data mainly from an atmospheric science point of view however, technical aspects such as the source apportionment of trace metals detected in the exhaust particles were important, too. The instruments used for the studies presented in this thesis were the Aerosol Time-of-Flight Mass Spectrometer (ATOFMS) and the Centrifugal Particle Mass Analyzer (CPMA), and will be introduced in the following chapters. These two instruments were used in the framework of this thesis to characterize aircraft exhaust particles according to physico-chemical properties. The ATOFMS provided information on the chemical composition of the sampled particles (cf. chapter 2). The CPMA was used to measure the size-resolved particle mass to derive effective densities

and fractal dimensions in order to gain insight on the particle morphology (cf. chapter 3). The effective density was then further used to determine PM mass concentrations, to estimate the total PM mass emissions and to predict PM mass losses in the sampling system (cf. chapter 4). Both, the chemical and the physical properties are important to characterize the PM in aircraft exhaust. The ability of a particle to act as CCN and IN, and also its optical properties depend on both the mixing state and chemical composition as well as on size and morphology. In addition, they might influence each other. For example, a larger particle surface might lead to an increased atmospheric aging process because more area is available where oxidation can take place.

1.3.1 Location of the engine test cell

The A-PRIDE campaigns were conducted in a test cell from SR Technics at the Zurich Airport. SR Technics is a company that commercially controls the performance of aircraft turbines and provides technical solutions for airlines. The left map depicted in Figure 1.7 shows the area of the airport Zurich and the engine test cell located in the southeastern corner of the airport. As seen on the zoomed in right map, the facility where the test cell is situated is close to the perimeter of the airport. A tram route and a road at a distance of <50 m and a freeway at ~100 m are located to the east of the test cell.
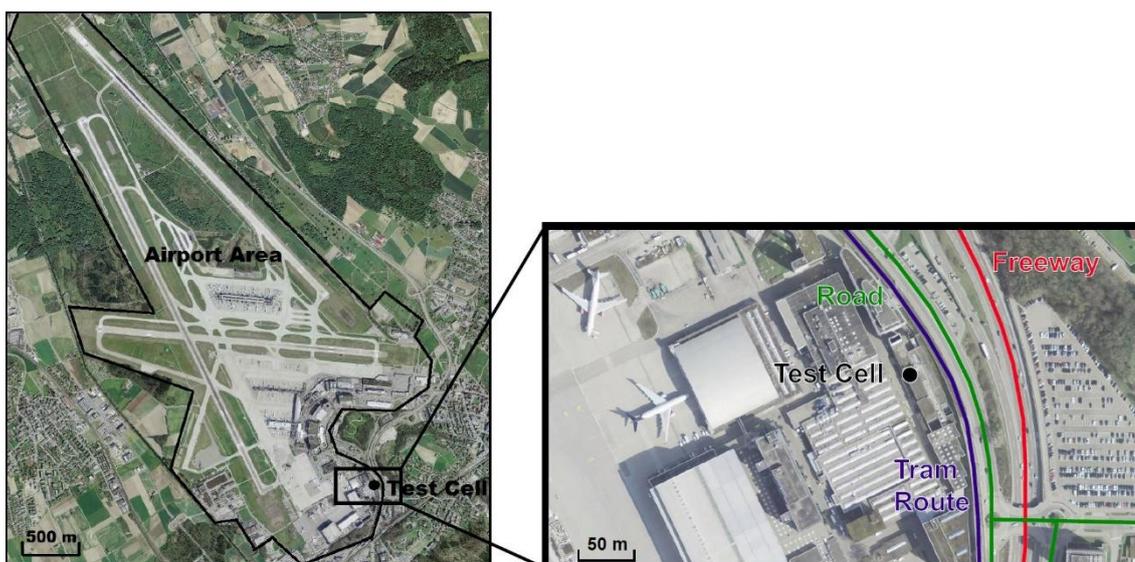
Figure 1.7   Overview of the Zurich Airport area and the location of the engine test cell from SR Technics (left), and a more detailed cut out of test cell and its near surrounding (Aerial images modified from https://map.geo.admin.ch).

A schematic of the test cell is shown in Figure 1.8. The engine was dismounted from the aircraft and placed on a rack in the test room where it was operated by technicians from SR Technics. The air sucked into the running engine enters the test cell by an open vertical shaft at the inlet section and then through the screen while the shutters were open. The exhaust is guided to the exhaust stack through a basket and an augmenter tube with an airflow straightener where it is finally released. The working platform was used prior to engine operation to install the sampling probe. During engine operation, no one is allowed to be present in the test room. The instrumentation was placed in a room next to the test cell.
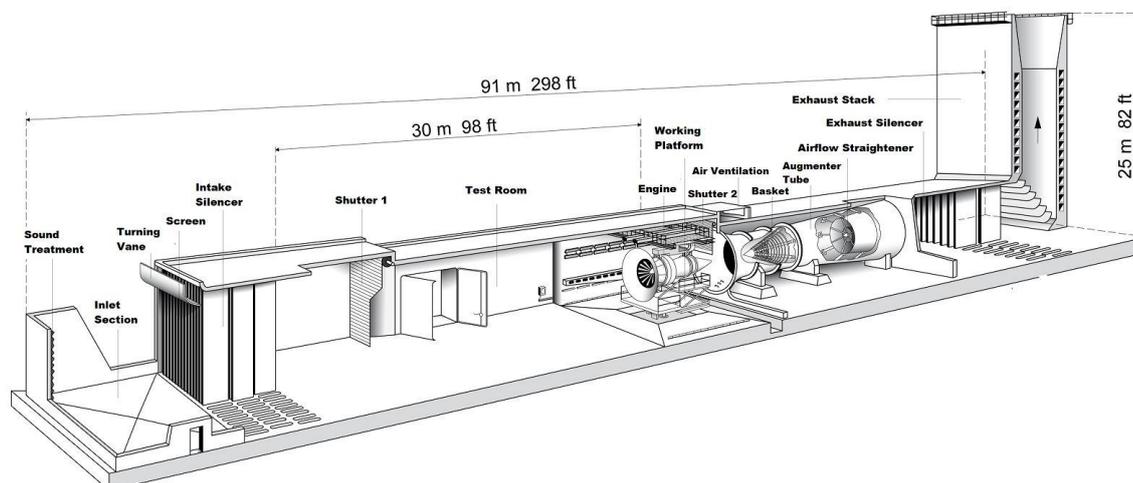
Figure 1.8   Schematic of the SR Technics engine test cell (copyright by SR Technics).

1.3.2 Sampling system

The sampling probe was installed directly behind the engine at a distance of ~0.7 m. The inlet of the probe (8 mm inner diameter) was oriented perpendicular to the engine exit plane such that the sampling was performed parallel to the exhaust stream. The probe consisted of Inconel 600 alloy to stand the high temperatures during engine operation. The emissions were then guided to the sampling system through a stainless steel pipe, which was heated to 160 °C to avoid condensation of volatile species onto the sampled particles.

A tee was used to split the sample flow into the two main measurement lines referred to as the PM line and the Annex 16 line (cf. Figure 2.1, Figure 3.1 and Figure 4.1). The PM line was mainly used for measurements of non-volatile PM number and mass whereas the Annex 16 line was primarily used to measure gaseous species. The term Annex 16 refers to the standards and procedures specified for the certification of aircraft emissions described in the "International Civil Aviation Organization Annex 16: Environmental Protection, Vol. 2 – Aircraft Engine Emissions" (ICAO, 2008). Both lines were ~25 m in length and consisted of conductive polytetrafluoroethylene (PTFE) tubing. PTFE tubing was chosen because of its dielectric property and its ability to withstand the temperature of 160 °C. The conditions for such condensation were monitored by measuring temperature and relative humidity in the sampling line. The PM line was diluted with synthetic air by a factor of 10 ±2 using an ejector dilutor. At the dilution point, the temperature was reduced from 160 °C to 60 °C. The Annex 16 line was not diluted and kept at 160 °C. Please refer to Lobo et al. (2015) for more details on the experimental set-up and the other instruments employed not described herein.

The A-PRIDE campaigns were carried out over three years during which a couple of campaigns were conducted. An overview of the A-PRIDE campaigns and the corresponding dates important for this thesis is given in Table 1.1. It also shows whether the CPMA and/or the ATOFMS was employed. Two types of measurements were conducted at the SR Technics test cell facility: the dedicated measurements (labelled "A-PRIDE") and the so-called piggyback measurements. For the dedicated measurement runs, the engine was leased by the campaign's participants and run according to their needs. Piggyback denotes measurements conducted during commercial engine tests and operations performed by SR Technics. However, the start, duration, applied thrust and engine type when performing piggyback measurements was usually not known in advance. As a consequence, these measurements were limited in their duration, and the amount of data collected was substantially less than during the dedicated ones.

Table 1.1   Measurement campaigns at the Zurich Airport, during which measurements with the CPMA and/or the ATOFMS were conducted.

Campaign	Date	CPMA	ATOFMS
A-PRIDE 4	November 2012	✓	✗
Piggyback	June 2013	✓	✓
A-PRIDE 5	July/June 2013	✓	✓
A-PRIDE 7	October 2014	✗	✓
Piggyback	May 2015	✗	✓

1.3.3 Aerosol time-of-flight mass spectrometry

1.3.3.1 Working principle

The Aerosol Time-of-Flight Mass Spectrometer (ATOFMS, TSI Model 3800-030) is an instrument capable to measure the chemical composition of single particles and their vacuum aerodynamic diameter (d_{va}) (Gard et al., 1997). ATOFMS measurements reveal important chemical properties of the investigated aerosol particles in PM aircraft exhaust. It was used because of its ability to resolve refractory material such as EC and metallic compounds and to gain insight on the mixing state of the aerosol particles. A schematic of the ATOFMS is depicted in Figure 1.9. It consists of three main regions with decreasing working pressures: 1) the particle sampling region ($\sim$270 Pa), 2) the particle sizing region ($\sim$10^{-3} Pa), and 3) the mass spectrometry region ($\sim$10^{-6} Pa).
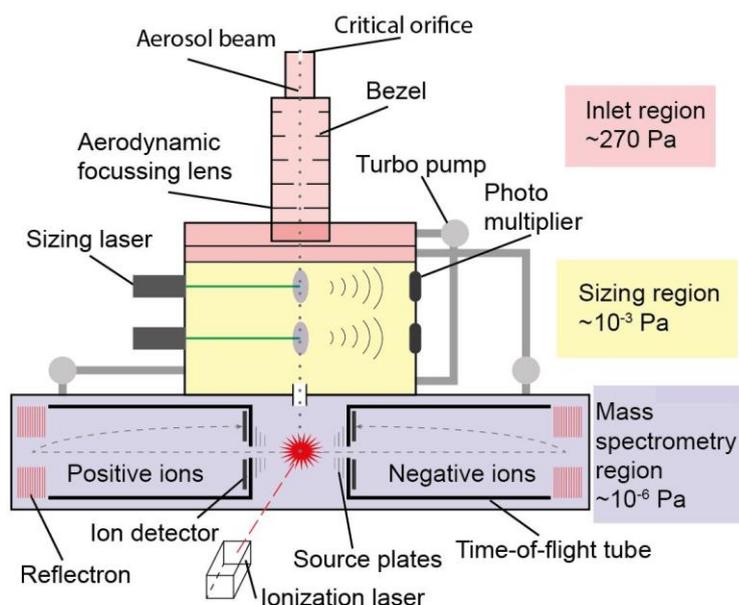
Figure 1.9   Schematic of the ATOFMS (adopted with courtesy from F. Mahrt).

The aerosol particles enter the ATOFMS via the inlet system. The inlet system consists of a critical orifice, a relaxation region and an Aerodynamic Focusing Lens (AFL). The critical orifice is a plate with a centred hole limiting the flow into the instrument to a rate of 0.1 l/min. Thus, the pressure in the inlet region is reduced to ~270 Pa. In the subsequent relaxation region, the particles are decelerated to minimize wall losses. In the AFL, the particles pass through a sequence of thin plate orifices, also called aerodynamic lenses or bezels. The bezels are of decreasing size from top to bottom and they are designed such that particles in a certain size range will exit the AFL in the form of a narrow particle beam. Two AFL are commercially available that are designed for particles with an aerodynamic size from 30 nm to 300 nm and 100 nm to 3000 nm, respectively (TSI, 2004b). During the A-PRIDE campaigns, the AFL optimized for an aerodynamic particle size range from 30 nm to 300 nm was used (TSI, 2004b). The AFL needs to be aligned prior to the measurements in order to maximize the particle transmission through the instrument. The particles exit the AFL through an acceleration nozzle and pass two differential pumping systems where the aerosol experiences supersonic expansion due to the pressure drop to $\sim10^{-3}$ Pa. Consequently, the particles are accelerated and reach a terminal velocity that depends on their aerodynamic size. The size-dependent acceleration is the basis for determining the aerodynamic size of the sampled particles (Gard et al., 1997). Smaller particles reach higher terminal velocities than larger particles.

In the sizing region, two orthogonally oriented continuous wave diode-pumped lasers detect the particles. The two sizing lasers are mounted at a vertical distance of 6 cm. A particle that passes a laser beam generates a scattered light pulse, which is detected in a photomultiplier tube (PMT) mounted orthogonally to the beam. In order to maximize light collection efficiency of the PMT an elliptical mirror focusses the scattered light towards the PMT detector. The sizing lasers have to be manually adjusted off-line such that the beams are horizontally aligned to keep the distance at exactly 6 cm. The duration between the two sequential signals registered by the PMTs if one particle passes through both laser beams one after the other is recorded as particle transit time. Knowing the transit distance (6 cm) the aerodynamic size of the particle can be determined. An exact measurement of transit time is crucial because it is further used to trigger the ionization laser. If a particle causes a signal when it passes the first sizing laser, a timing circuit blocks further signals from being processed until either the ionization laser is triggered or after 800 µs. This prevents false assignments of the detection signals to the

corresponding particles due to overlapping signals if more than one particle are coincidently located between the sizing lasers.

The particles then enter the mass spectrometry region where the pressure is further reduced to $\sim 10^{-6}$ Pa by two molecular pumps. An ionization laser (a neodymium: yttrium-aluminium-garnet laser (Nd:YAG, $\lambda = 266$ nm)) located at a distance of 12 cm from the second sizing laser is triggered by the timing circuit in order to hit the particle. The ionization laser needs to be aligned in order to enhance the rate of hit particles. The time when the ionization laser is triggered is derived from the particle transit time between the sizing lasers by simply doubling it (because of the doubled transit distance). The energy of the ionization laser is variable and can be adjusted. It was always set to ~ 1 mJ/pulse during our experiments. Because the ionization process depends (among other factors) on the laser energy it is important to keep it constant during measurements to ensure comparability of the obtained data. If the ionization laser hits the particle, it is ablated and ionized, resulting in charged ions. Ions can be either molecules or molecules. The event of the ionization pulse starts the data logging of the measured current from the ion detectors generating the mass spectra. Once ionized, the ions are accelerated by the potential of the two source plates. The source plates have a potential of $+10$ kV and -10 kV, respectively. The ions are first separated according to their polarity into the negative and positive flight tube. After acceleration, the ions and molecules reach a constant terminal velocity depending on their mass. The heavier ions reach a smaller terminal velocity than lighter ones. Consequently, they are separated according to their mass-to-charge ratio (m/z). At the end of the flight tube a reflectron (also called ion mirror) forces the ions to reverse their direction of travel due to an electric field. This doubles the distance the ions have to travel compared to a design without a reflectron and thus enhances the resolution of the recorded data in terms of m/z values. The reflectron additionally decreases the potential spread of flight times of ions with the same mass. Such a spread can be caused by small differences in their kinetic energy after acceleration due to differences in initial kinetic energy, different starting location and initial directions of motions (Gross, 2011). As ions with more kinetic energy penetrate the reflectron deeper the flight path and thus the time of flight is slightly longer, which compensates for the higher velocity compared to particles with less kinetic energy (Gross, 2011). The time (of flight) the individual ions and molecules need to travel through the flight tubes until they reach the detector plates is recorded and converted into m/z values. The output is one positive and one negative mass spectrum for each

ionized particle, representing the chemical composition of this particle. Figure 1.10 exemplary depicts a positive (above) and a negative (below) mass spectrum of an aircraft engine exhaust particle recorded by the ATOFMS. The x- and the y-axis show the *m/z* values and the measured intensity based on the current produced by the ions at the detectors. Ions of the same charge and mass result in a peak at the corresponding *m/z* value, which can then be attributed to potential ions. The spectra in Figure 1.10 for example both show a distinct pattern with peaks at *m/z* = 12, 24, 36, etc. from EC.
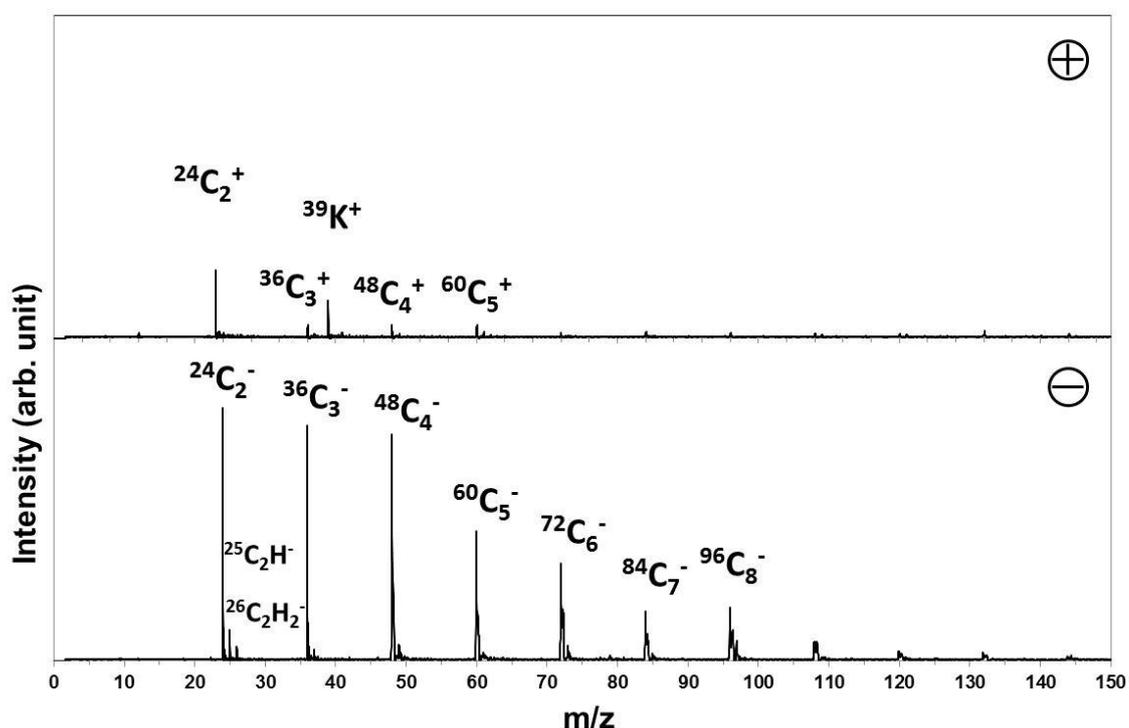
Figure 1.10   Example of a positive (above) and a negative (below) mass spectrum from an aircraft engine exhaust particle recorded by the ATOFMS.

1.3.3.2 Data analysis

The ATOFMS data needs to be calibrated for mass and for size. The mass calibration is the conversion from the measured time-of-flight into an *m/z* value. The time-of-flight is calibrated with known ions. This is achieved by sampling aerosol from a metal solution containing specified metal ions of known and easily distinguishable masses. The obtained spectra can then be used to identify the peaks of the metals and assign the corresponding *m/z* value to them. The size calibration is needed to convert the measured particle transit time between the two sizing lasers into the particle aerodynamic size. It

is performed by recording data from particles of known sizes and density. Mostly, commercially available polystyrene latex (PSL) particles are used. PSL particles are of unit density, spherical and they are available in many different sizes. The obtained information on size from at least four different sizes of PSL particles is then used to generate a function describing the relationship between size and transit time. These calibrations need to be repeated if any adjustments (e.g. new alignment of the AFL, sizing lasers or ionization laser) were performed or if the ATOFMS operates at changing ambient conditions. Both size and mass calibration can be performed using MS-Analyze, a software used to analyze and process ATOFMS data (TSI, 2004a).

MS-Analyze is the standard program to analyze ATOFMS data. The data set contains the individual mass spectra and the aerodynamic size of the particles that were hit by the ionization laser. The data can be displayed as tables, graphs and lists, and it can be exported to other applications such as a Microsoft Access database or ENCHILADA (see below). In MS-Analyze, queries can be performed allowing the classification of particles with specific compounds by searching for the corresponding *m/z* value. It is also possible to define a query with multiple *m/z* values that have to match the mass spectra in order classify the particles. The queries can be adjusted by defining peak height and absolute or relative peak area. The relative peak area is the area of a peak divided by the sum of all peaks present in the spectrum. A query can further be performed inclusively or exclusively. An inclusive query allows a particle to be classified in multiple classes whereas an in exclusive query a particle is only assigned to the first class for which the defined values accord. Besides the compound classification, MS-Analyze can also display time lines and size distribution graphs of the sampled particles. MS-Analyze also creates average spectra of data sets or subsets thereof defined according to composition, size or time recorded.

TRD (TimeResolvedData) is a Microsoft Access form designed to analyze ATOFMS data according to user-defined time bins. Prior to analyses, the data has to be transferred from MS-Analyze to an SQL-database. TRD allows generating timelines, size histograms, average spectra, *m/z* correlations and threshold histograms. The latter are histograms for which threshold values such as peak height, peak area and relative peak area can be defined.

Besides MS-Analyze and TRD, also ENCHILADA (Environmental Chemistry through Intelligent Atmospheric Data Analysis) was used to analyze the ATOFMS data presented in this thesis. ENCHILADA was used for a cluster analysis of the analyzed particles.

Different clustering algorithms, e.g. k-means and ART-2a (Rebotier & Prather, 2007; Gross et al., 2010; Giorio et al., 2012), can be applied to the ATOFMS data to group similar spectra into clusters. Each resulting cluster is representative for a particle type that shows specific *m/z* values. Herein, k-means was used that allows to define and identify an adequate number of clusters using a value (average distance from centroids) indicating by how much the spectra differ from each other. This method was shown to give similar results as ART-2a and other hierarchical methods (Rebotier & Prather, 2007). Finally, similar clusters were manually merged together.

The advantage of the ATOFMS compared to mass spectrometer where the bulk of samples are analyze is its capability to record the chemical composition of individual aerosol particles. This allows gaining insight into the mixing of the particles that would not be possible if only the composition of the bulk was known. On the other hand, the ATOFMS data does not directly provide quantitative results like many other mass spectrometric methods. The ATOFMS is not quantitative mainly because of matrix effects (Liu et al., 2000). Matrix effects arise from the fact that different chemical species can influence each other's ionization efficiencies. Moreover, the ionization efficiency was shown to decrease for the same particle if secondary species were used to coat the particle (Hatch et al., 2014). Both, matrix effects and coatings result in changes in the measured ion peak areas of a specific compound even if the amount thereof remains constant. Nevertheless, analysis of relative peak areas from particles of the same type can reduce matrix effects to a certain extent because of lower spectrum to spectrum variability (Gross et al., 2000). Thus, such spectra can be used to reveal some information on relative differences in the amount of constituents under different conditions by comparing the corresponding averaged relative peak areas.

1.3.4 Centrifugal particle mass analyzer

The Centrifugal Particle Mass Analyzer (CPMA; Cambustion Ltd., Cambridge, UK) classifies aerosol particles according to their mass-to-charge ratio (Olfert & Collings, 2005; Olfert et al., 2007). It was used to investigate the physical properties of particles from aircraft engine exhaust. Within the CPMA, the particles pass between two rotating concentric cylinders on which a voltage is applied, and only particles in a narrow mass-to-charge ratio range are transferred through the instrument. Thus, the CPMA produces a monodisperse aerosol consisting of particles with a certain mass-to-charge ratio.

The CPMA is a further development of the Aerosol Particle Mass analyzer (APM, Figure 1.11) introduced by Ehara et al. (1996). Their general working principle however, is identical. In the APM, the aerosol is introduced between the two cylinders, denoted as inner and outer electrode in Figure 1.11. The cylinders rotate at the same angular speed (ω) creating a centrifugal force (F_c). Once introduced, the aerosol rotates with the same ω as the cylinders, and F_c acts on the aerosol particles. A high voltage (V) is applied between the two cylinders using brushes in order to make contact between the rotating and the stationary parts. The voltage is applied such that positively charged particles experience an electrostatic force (F_e) acting in the opposite direction than F_c. Particles on which F_c and F_e act with the same magnitude eventually exit the APM whereas particles that experience different magnitudes of F_c and F_e precipitate on either of the cylinders walls. F_c depends on the cylinder radii (r_1 and r_2), ω and particle mass, and F_e depends on V and on the charge of the particle. Thus, all parameters are known and assuming the particles to carry one elementary charge, the mass of the classified particles can be determined. By adjusting ω and F_e, the desired particle mass can be set.
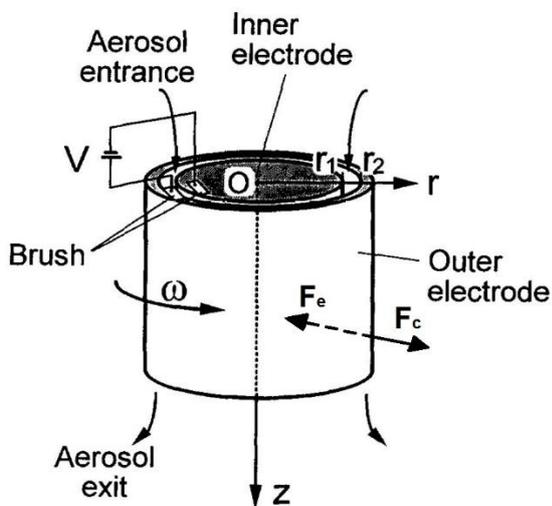
Figure 1.11   Schematic of the APM (Ehara et al., 1996).

This concept however, does not take into account the gradient of F_c and F_e within the narrow gap of the cylinders. Since the cylinders rotate at the same angular speed, F_c increases towards the outer one. In contrary, F_e decreases with increasing r because, analogously to an electrical point source, the strength of the electric field decreases with increasing radial distance from the inner cylinder (the center). If a particle enters the gap

of the cylinders not exactly in the middle, where F_c equals F_e, it will experience either a larger F_c or F_e if it is closer to the outer or inner cylinder, respectively. Consequently, the beam of desired particles with exactly the same mass is diverging from the center of the gap. This leads to the loss of particles with the desired mass. This problem is overcome in the CPMA. In the CPMA, the speed of the cylinders are controlled individually and do not have the same ω. This allows adjusting the gradient of F_c. For a desired particle mass, the gradient is set such that F_c is slightly larger towards the inner and slightly smaller towards the outer cylinder than F_e, while both forces are still in equilibrium in the center of the gap. Consequently, the stream of particles having the desired mass is converging between the cylinders and consequently the particle transmission efficiency is enhanced compared to the APM. The ability of the CPMA to control ω individually for each cylinder constitutes the main and difference to the APM.

The CPMA can be used either to generate an aerosol sample consisting of particles with the same mass or to record the mass distribution (similar to a particle size distribution) of aerosol particles from a constant source. The latter requires performing a so-called step scan. In the step scan mode, the CPMA consecutively classifies particles of different masses. The particle concentration of the classified particles is recorded at each step (corresponding to a certain particle mass) downstream of the CPMA using a Condensation Particle Counter (CPC). Within the CPC, the aerosol particles grow by condensation in a saturated region to a size large enough to be detected by a laser and counted. Both mass and concentration need to be processed for the same instant of time. The CPMA is capable to do so if the CPC data is transferred to the CPMA and information on sample flow rate and transit time between the instruments are provided as input parameters. The CPC transfers the information on the particle concentration to the CPMA. If measuring from a source with largely varying particle concentration, a second CPC must be used upstream of the CPMA to account for the fluctuations. The measured concentrations combined with the corresponding masses finally yield a particle mass distribution of the aerosol sample recorded by the CPMA.

Further information on the effective density and morphology of fractal particles can be derived if the CPMA is used to measure the mass of aerosol particles previously selected according to their size. In order to measure simultaneously the mass and size of aerosol particles, the CPMA can be used in combination with a Differential Mobility Analyzer (DMA). The DMA is a device that classifies particles according to their mobility size. Within a DMA, the particles travel through a metal tube with the aerosol

flow and are forced to move towards the center due to an electric field. A narrow gap at the inner end of the tube finally allows the particle to exit and be used for further measurements. The terminal particle velocity towards the center depends only on the particle electrical mobility size and instrument design. Thus, for a certain voltage applied only particles with the same known electrical mobility size exit the DMA whereas all other particles precipitate in the DMA and are consequently removed from the sample flow. Analogously to the CPMA, the DMA can be used either to generate a monodisperse aerosol consisting of particles with the same mobility size or to measure a size distribution if used in combination with a CPC downstream of the DMA.

The presented studies in chapters 3 and 4 used a DMA-CPMA-CPC system. This way, the mass of pre-selected particles with a certain electrical mobility size was measured. To account for multiply charged particles, a neutralizer was used to apply a known charge distribution to the particles prior to the system. To generate a monodisperse aerosol, the DMA was set to classify particles with a certain electrical mobility size. Downstream of the DMA, the CPMA was run in the step scan mode to record the mass distribution of the classified particles.

The mode (the mass that most of the particles have) of the obtained mass distribution was then determined by fitting a log-normal distribution to the data. The combined knowledge of particle electrical mobility size and mass yields the effective density of a particle (c.f. 3.2). Because soot particles are fractal objects, their effective density changes with particle size. This size-dependence can be measured using the DMA-CPMA-CPC system by performing measurements for different pre-selected particles sizes. The change of the effective density with particle mobility size reveals the fractal dimension. More precisely, it is termed mass-mobility exponent if it is derived from the particle mass and mobility size. However, the mass-mobility exponent and the fractal dimension are closely related to each other and are equally used to describe aggregate particles (DeCarlo et al., 2004) as explained in 3.2. Since one CPMA (step-) scan takes ~4 to 7 minutes, this requires quite some time during which the particle source needs to be constant. Note that in principle, it is also possible to pre-select particles with a certain mass using the CPMA and then perform a DMS scan in order to determine their size.

1.4 Thesis objectives

The main goal of this thesis is to provide new insights on the physical and chemical properties of fresh soot particles emitted by aircraft engines. The results are meant to contribute to a better understanding of the characteristics and behavior of aircraft soot particles in the atmosphere and in the applied sampling system. The initial properties of these particles such as size distribution, concentration, morphology and chemical composition are key components because they determine their transport behaviour and impacts on climate and interactions clouds. Although not investigated within the framework of this thesis, these properties are also important for the ability of aerosol particles to act as CCN and/or INP and to describe and understand plume processes (IPCC, 1999). Moreover, information on the initial conditions of aerosol particles in general are important to understand their further transformation due to the aging process they experience later in the atmosphere. Soot particles in particular may turn from hydrophobic to hydrophilic due to condensation of or coagulation with hydrophilic aerosol particles which further results into changes in their ability to act as CCN (Lambe et al., 2015). Such changes and corresponding timescales however, can only be properly understood and predicted (e.g. for the use in climate models) with the knowledge on the physic-chemical properties of the nascent particles. Besides the need for a thorough characterization of soot particles emitted from aircraft engines because of their atmospheric relevance, the presented results are also used with respect to aspects that are more technical. The experimental set-up at the Zurich Airport was unique because it was developed recently in the course of establishing a certification standard for aircraft engines. The measured initial chemical composition revealed metallic compounds to be present in the particles. This information was then used to assign these compounds to potential sources in the aircraft engine. This would have not been possible with measurements from aged particles. Furthermore, the presented results also provide information to characterize and evaluate this standardized sampling system used during the A-PRIDE campaigns.

Chapter 2 presents findings from measurements performed using the ATOFMS. It describes the chemical composition of the exhaust particle types from three different engine types. The elemental carbon to total carbon ratio of the particles was determined. This chapter focuses on the occurrence of metallic compounds in the soot particles. These metallic compounds are discussed with respect to potential sources inside the engine in order to assign them. The considered sources were fuel, oil and engine wear-

ing components. A quantitative analysis of samples collected from these sources was performed using inductively coupled plasma mass spectrometry.

Chapters 3 and 4 describe the physical properties of the emitted particles. The morphology of the soot particles is investigated for an engine type under different operating conditions, i.e. at different thrust settings. This includes determination of the particle size, fractal dimension and effective density. Additionally, the data is compared to literature values from another engine type, which was also investigated in the same test cell using a similar set-up. The effective density was further used to determine PM mass concentrations and to estimate PM mass emissions of the aircraft turbine. The mean effective density was derived to estimate particle losses in the sampling line. A summary of the presented results and suggestions for further research based on the findings can be found in Chapter 5.

2 CHEMICAL CHARACTERIZATION OF FRESHLY EMITTED PARTICULATE MATTER FROM AIRCRAFT EXHAUST USING SINGLE PARTICLE MASS SPECTROMETRY

Manuel Abegglen[a], B. Brem[b,c], M. Ellenrieder[d], L. Durdina[b,c], T. Rindlisbacher[e], J. Wang[b,c], U. Lohmann[a] and B. Sierau[a]

[a] *Institute for Atmospheric and Climate Science, ETH Zurich, Switzerland*
[b] *Laboratory for Advanced Analytical Technologies, Empa, Dübendorf, Switzerland*
[c] *Institute of Environmental Engineering, ETH Zurich, Zurich, Switzerland*
[d] *SR Technics, Zurich, Switzerland*
[e] *Swiss Federal Office of Civil Aviation, Bern, Switzerland*

This chapter is adapted from the submitted article.

Abstract

Non-volatile aircraft engine emissions are an important anthropogenic source of soot particles in the upper troposphere and in the vicinity of airports. They influence climate and contribute global warming. In addition, they impact air quality and thus human health and the environment. To investigate this, we provide fundamental information by presenting a chemical characterization of freshly emitted particulate matter from aircraft engine exhaust. The chemical composition of non-volatile particulate matter emission from aircraft engines was investigated using single particle time-of-flight mass spectrometry. The exhaust from several engines was sampled and analyzed. The soot particulate matter was sampled directly behind the turbine in a test cell at Zurich Airport. Single particle analyses focused on the identification of the particle types with focus of metallic compounds. The particles analyzed herein represent a subset of the emissions composed of the largest particles with a mobility size >100 nm due to instrumental restrictions. A vast majority of the analyzed particles was shown to contain elemental carbon, and depending on the engine and the applied thrust, the elemental carbon to total carbon ratio ranged from 83 % to 99 %. The detected metallic compounds were all internally mixed with the soot particles. The most abundant metals in the exhaust were Cr, Fe, Mo, Na, Ca and Al; V, Ba, Co, Cu, Ni, Pb, Mg, Mn, Si, Ti and Zr were also detected. We further investigated potential sources of the ATOFMS-detected metallic compounds using Inductively Coupled Plasma Mass Spectrometry. The potential sources considered were kerosene, engine lubrication oil and from engine wearing components. An unambiguous source apportionment was not possible because most metallic compounds were detected in several of the analyzed sources. Cobalt and zirconium were found to originate solely from engine wear.

2.1 Introduction

The continuous increase of commercial air traffic has led to rising public awareness and concerns about the associated Particulate Matter (PM) emissions. The annual future growth rate is estimated to be 3.4–6.1 % (ICAO, 2013) in terms of passenger revenue kilometers. The PM legislation regarding aircraft emission however, has been lagging behind general emission regulations from other combustion sources (e.g. road traffic). Up to now, the standard way to regulate PM emissions for aircraft engines manufactured after 1983 is to limit smoke number (ICAO, 2008). Smoke number is a unit derived from filter measurements using its change in reflectance after sampling a

prescribed volume of exhaust. The smoke number standard is an exhaust plume non-visibility criteria. It is insufficient to assess particulate matter related air quality and climate impacts from aircraft engines. In the course of the recent development of an ICAO particulate matter certification standard for aircraft engines, the Aviation Particulate Regulatory Instrumentation Demonstration Experiment (A-PRIDE) campaigns were initiated. The A-PRIDE campaigns were conducted in the SR Technics facility at Zurich Airport in Switzerland. Previous studies from the A-PRIDE campaigns focused primarily on the physical characterization of the exhaust particles (Durdina et al., 2014; Abegglen et al., 2015) and evaluation of the sampling system in order to demonstrate its suitability for aircraft emission certification (Lobo et al., 2015). Herein, we focus on the chemical characterization of PM in the aircraft engine exhaust. The presented measurements were mainly conducted during A-PRIDE 5 in the year 2013 investigating a very common in-production turbofan engine, using an Aerosol Time-of-Flight Mass Spectrometer (ATOFMS, TSI Model 3800-030). The ATOFMS allows to investigate the chemical composition of single particles, and the A-PRIDE campaigns offered a great and rare opportunity to sample and study unaltered combustion products from aircraft engines.

The emitted PM from aviation is of interest because it represents a unique anthropogenic source of soot particles in the upper troposphere and in the vicinity of airports. These particles alter the Earth's radiation budget in various ways depending on their physical and chemical properties. Based on findings presented in the special report on aviation and the global atmosphere (IPCC, 1999) and IPCC AR4 WG1 (IPCC, 2007), Lee et al. (2009) divided the climate effects from aircraft PM on climate into three radiative forcing components: soot aerosols, linear condensation trails (contrails), and induced cirrus cloudiness, which are all believed to result in a warming. In addition, the emitted particles could act as Ice Nucleating Particles (INP) and affect natural clouds.

Freshly emitted soot particles directly absorb and scatter solar radiation, primarily due to their opaque appearance. The magnitude however depends (besides size and morphology) on the chemical composition. A higher Elemental Carbon (EC) content for example enhances absorption of radiation whereas a lower EC content leads to an increase of the single scattering albedo (Qiu et al., 2014). Linear contrails form just behind aircraft due the emission of heat and water vapor and formation depends on the ambient temperature and ambient air humidity as well as on the exhaust temperature and mixing processes after emission. The cooling of the exhaust stream causes water

vapor to condense onto a fraction of the emitted particles and to freeze subsequently if the temperature is sufficiently low. Contrails result in a positive radiative forcing due to their occurrence in high altitudes. Similarly to thin cirrus clouds, they reflect little incoming solar radiation back to space but absorb terrestrial infrared radiation. Their global coverage for the year 2006 was detected via satellite to be 0.07 % (Duda et al., 2013). Research on occurrence and formation of contrails dates back almost 100 years and is well summarized in the review article from Schumann (1996). If the ambient air is supersaturated with respect to ice, the formed ice particles continue to grow and can form a persistent contrail. The largest radiative forcing arises from the induced cirrus caused by the possible evolution of linear contrails into persisting cirrus clouds (Burkhardt & Kärcher, 2011). These spreading cirrus clouds can become undistinguishable from naturally (e.g. synoptically or orographically) evolved cirrus clouds. With a confidence of 90 %, the aviation-induced radiative forcing in the year 2005 was estimated to be in the range from 23–87 mW/m^2 without aviation-induced cirrus and from 38–139 mW/m^2 including cirrus cloud formation, corresponding to a contribution to the anthropogenic forcing of 4.9 % (2–14 %) (Lee et al., 2009).

Moreover, it has been found that some fraction of carbon-containing particles are efficient INPs (Cozic et al., 2008). Thus, aircraft emissions can lead to regionally increased INP concentration affecting natural cirrus clouds even in the absence of contrail formation (Kärcher et al., 2007), including changes in optical properties and delays of freezing onsets (Burkhardt & Kärcher, 2011). This is explained by additional heterogeneous INP inhibiting the homogeneous freezing of the background aerosol particles, due to the decreased water content available. The magnitude of this effect remains uncertain because it depends heavily on the ice-nucleating efficiency of the emitted soot particles and of the background aerosol particles which are not yet completely understood (Zhou & Penner, 2014). A study performed by Cziczo et al. (2013) tackling the properties of INP in the upper troposphere showed that a dominant fraction of Ice Residuals (IR) collected in cirrus clouds contain metal compounds such as sodium, potassium, copper, lead and iron. These compounds have also been found in aircraft emissions by sampling the exhaust (Agrawal et al., 2008). Also, Cziczo et al. (2009) showed that lead-containing mineral dust particles are efficient INP, as a consequence, lead- or metal-containing particles might increase the INP number in the atmosphere. Thus, a thorough chemical characterization of single particles from fresh aircraft PM emissions provides

information to study the link between aircraft emissions and ice formation processes in the atmosphere.

The radiative and ice-nucleating properties change over time as the soot particles undergo aging by the uptake of water and/or secondary volatile species and oxidation. These processes are partly influenced by the particle's initial composition (Rudich et al., 2007). The Organic Carbon (OC) components on the particle surface were found to be important for the aging process of soot and may even alter the Cloud Condensation Nuclei (CCN) or INP activity when they are oxidized by O_2 under solar radiation and turn into soluble organics (Han et al., 2012).

Aviation PM emissions are also of importance as PM in general is known to cause adverse health issues. The emitted particles have been shown to be small with a geometric mean diameter well below 100 nm (Lobo et al., 2007a; Kinsey et al., 2010; Abegglen et al., 2015) and therefore fall mainly into the particle class described as ultrafine PM ($PM_{0.1}$). Ultrafine particles can penetrate deeper into the human respiratory system and are less likely to be removed than larger particles and may be able to enter the blood stream (Terzano et al., 2010). Health effects in general seem to be more associated with Black Carbon emission (BC) than with PM_{10} or $PM_{2.5}$ alone (Janssen et al., 2012), but it was not possible to show that BC directly is a toxic component. Janssen et al. (2012) therefore summarizes that BC probably acts as a carrier for toxic substances. This supports findings from an earlier study showing that particles containing metals such as vanadium, iron, copper and nickel can cause epithelial injuries (Pagan et al., 2003). It seems intuitive that the largest respiratory health effects caused by aircraft emissions are found in the vicinity of airports (Keuken et al., 2015), especially for workers at airports (Touri et al., 2013). However, emissions can cause health effects not only in the vicinity of airports but also on larger spatial scales (Yim et al., 2015).

Earlier studies on PM aircraft emissions focused primarily on the particle size and concentration in proportion to the thrust applied to the engine (Petzold & Schröder, 1998; Rogers et al., 2005; Corporan et al., 2008; Herndon et al., 2008; Onasch et al., 2009). Investigations on the composition in terms of organic content have also been performed (Onasch et al., 2009; Timko et al., 2010a; Lobo et al., 2015). Literature on the investigations of PM aircraft emissions with respect to the chemical composition is also available. Fordyce and Sheibley (1975) used trace element content analysis from jet fuel to estimate corresponding concentrations in typical exhaust gas. Kinsey et al. (2011) sampled exhaust plumes from commercial aircraft at a distance of ~30 m behind

the engine using optical instruments to provide data on BC concentrations and gravimetric analysis of filters to investigate the elemental composition quantitatively. Agrawal et al. (2008) conducted measurements on commercial aircrafts and presented emission indices of PM, elemental and organic carbon as well as of metallic compounds detected in the exhaust. Vander Wal and Bryg (2014) performed X-ray photoelectron spectroscopy to investigate jet exhaust particles from different aircraft and found varying amounts of N, S, Na, Ca, Zn, Ba, Sn, Cr and Al. However, the investigation of aircraft PM emission in terms of chemical characterization from single particles is still in an early stage and only few studies exist. Demirdjian et al. (2007) sampled soot particles emitted by an aircraft gas turbine engine directly behind the engine duct in order to investigate the composition of soot agglomerates. The sample was then deposited on copper microgrids and analyzed. They have found impurities of Fe, O, S, K and Mn. Mazaheri et al. (2013) collected PM_1 samples on filters and membrane grids 200 m from an airfield runway in order to perform elemental analysis on discrete particles using energy dispersive X-ray spectroscopy. They found C, O, S, Cl, Na, Al, Si, Ca, Ti, Cr, Fe, Co, Ni, Cu, Zn and Pb but attributed them not only to engine exhaust but also to a diverse range of sources such as tire wear, dust and automotive traffic. Especially studies on fresh aircraft exhaust sampled directly behind the engine remain scarce and no study exists to our knowledge that investigates the chemical composition of freshly emitted aircraft exhaust particles using in-situ single particle mass spectrometry. Our study focuses on a general chemical characterization of single particles sampled directly behind the engine with emphasis on metallic compounds in the particles.

2.2 Methods

2.2.1 Measurement campaigns and location

The majority of the measurements presented herein were conducted during the dedicated Aviation - Particle Regulatory Instrument Demonstration Experiment 5 (A-PRIDE 5) campaign in July and August 2013. Additional data was collected during piggyback measurements in Mai 2015. The campaigns took place at the Zurich Airport where the measurements were conducted in a test cell of SR Technics. The facility is located in the southeastern corner of the airport area. A tram route and a road are going by in the east of the test cell at a distance of <50 m and a freeway at ~100 m.

The particle emissions of three in-production, high-bypass turbofan engines were investigated. All of the engines are widely used in the current aircraft fleet. Engine 1 and 2 were core-flow single annular combustor types with rated outputs in the range of 120 kN, here referred to as "Turbofan 1 and 2", respectively. Engine 3, here referred to as "Mixed-Flow Turbofan" utilized also a single annular combustor with rated output of ~150 kN, but its exhaust is diluted with its bypass air at a ratio of approximately 6:1. All engines were fueled with standard Jet A-1 fuel.

2.2.2 Experimental set-up

The emitted particles were sampled by a probe oriented parallel to the exhaust flow (Figure 2.1). The sampling probe was positioned at a distance of ~0.7 m behind the engine duct, guiding the emissions through an 8 mm inner diameter stainless steel pipe heated to 160 °C to the sampling system. A tee was used to split the sample into two main measurement lines referred to as the PM line and the Annex 16 line. The PM line was mainly used for measurements of non-volatile PM number and mass whereas the Annex 16 line was mainly used to measure gaseous species. Both lines were conductive PTFE and ~25 m in length before leading to the measuring instruments. Both lines were heated in order to prevent condensation of volatile species onto the sampled particles. The PM line was diluted by a factor of ~8–12 with synthetic air (grade 5.0) using a Dekati ejector dilutor (Dekati, Model DI 1000, Dekati Ltd., Kangasala, Finland). At the dilution point, the PM line temperature was reduced from 160 °C to 60 °C. This 60 °C line was used for the PM instrumentation and the ATOFMS. The undiluted Annex 16 line was maintained at 160 °C leading to the Annex 16 gaseous analyzers. A tee at the end of this line was used to guide the sample through a 60 °C heated line to a Nafion (Perma Pure, Model PD-100T-24 (MSS), Perma Pure LLC, Toms River, USA) dryer to the ancillary Annex 16 instruments and a Scanning Mobility Particle Sizer (SMPS, TSI, Model 3936, TSI Inc., St. Paul, USA) system. See Lobo et al. (2015) for a more detailed overview of the additional instruments and results from this experimental set-up.
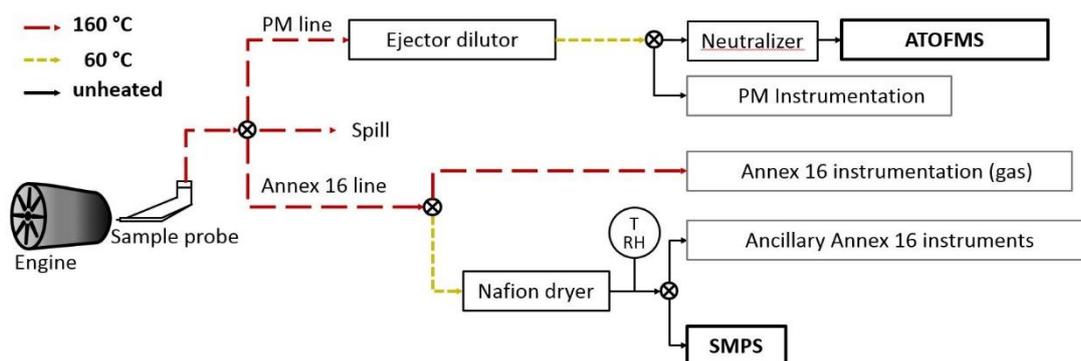
Figure 2.1   Simplified schematic of the experimental set-up.

2.2.3 Instruments

2.2.3.1 Aerosol time-of-flight mass spectrometer

An Aerosol Time-of-Flight Mass Spectrometer (ATOFMS, TSI Model 3800-030) was used to investigate the single particle chemical composition of non-volatile fresh emissions from aircraft engines. The ATOFMS is a mass spectrometer that measures the chemical composition of single particles and their vacuum aerodynamic diameter (d_{va}) (Gard et al., 1997) and has the capability to resolve refractory material such as EC as well as metallic compounds. Each mass spectra obtained allows the chemical analysis of this particle.

The ATOFMS works at low pressures which draws the sample flow into the instrument. It consists of three main regions with decreasing working pressures: 1) the particle sampling region ($\sim$270 Pa), 2) the particle sizing region ($\sim$$10^{-3}$ Pa), and 3) the mass spectrometry region ($\sim$$10^{-6}$ Pa). The sample flow rate into the instrument was 0.1 l/min, set by a critical orifice. A backup flow between 1 l/min and 3 l/min (depending on the flow needed by other instruments) was used to shorten the response time. Downstream of the critical orifice, the particles pass through an Aerodynamic Focusing Lens (AFL) that aligns the particles into a narrow beam and then into the sampling region. For this study, an AFL optimized for an aerodynamic particle size range from 30 nm to 300 nm was used (TSI, 2004b). Once the particles are in the sizing region, they accelerate due to the pressure drop depending on their size and are detected by two consecutive continuous, orthogonally oriented wave diode-pumped lasers ($\lambda = 532$ nm). The time they need to travel between the sizing lasers is used to determine their aerodynamic size and to trigger the ionization laser in the following. The particles then enter the mass spec-

trometry region where the particles are ionized by the ionization laser (Nd:YAG, $\lambda = 266$ nm), set to an energy of ~1 mJ/pulse. If the particle is hit by the ionization laser, it gets ablated and ionized, resulting in ions and molecules, both positive and negative. They are then separated according to their mass-to-charge ratio (*m/z*) by their mass-dependent acceleration in positive and negative electromagnetic fields in the flight tubes. The time (of flight) the individual constituents need to travel through the electromagnetic fields until they reach detector plates is recorded and converted into *m/z* values. The output is a positive and negative mass spectra for each ionized particle, revealing its aerodynamic size and chemical composition.

Before the particles entered the ATOFMS they were treated with a 210^{Po} neutralizer in order to minimize their electric charge increasing the hit rate (fraction of sized particles that are ionized). This is because electrostatic forces can cause deviation of the particle's trajectory within the instrument.

The ATOFMS data itself is not quantitative because of several reasons. For example, the coating of a particle with secondary species was shown to decrease the ionization efficiency resulting in changes in the measured ion peak areas (Hatch et al., 2014). Moreover, different chemical species in the same particle can influence each other's ionization efficiencies due to the so-called matrix effects (Liu et al., 2000). Nevertheless, analysis of spectra from the same particle type using relative peak areas can reduce matrix effects to a certain extent because of lower spectrum to spectrum variability (Gross et al., 2000). Thus, average relative intensities from a large number of similar particles can be used to gain some information on relative differences in the mass of compounds in the particle when comparing different conditions.

2.2.3.2 Inductively coupled plasma mass spectrometry

Inductively Coupled Plasma Mass Spectrometry (ICP-MS) was used to analyze samples from fuel, lubrication oil and wearing from engine. Fuel and oil were analyzed using an ELAN 6100 (Perkin Elmer, Canada) whereas the sample from engine wear was analyzed using an ELAN 6100DRC^{+} (Perkin Elmer, Canada). ICP-MS is an offline method often used to measure metals from a bulk sample. It is very sensitive to the concentration of the analyzed compounds, which can be as low as one part in 10^{-15}. It uses argon treated with a high frequency current in order to heat it up to ~10 000 K, turning the argon into a plasma. The sample is introduced with argon as carrier gas into the argon plasma where it is vaporized, atomized and ionized (Gross, 2011). The result-

ing ions are accelerated by an electromagnetic field and subsequently registered by detectors, and quantification is achieved by comparison with certified reference materials.

2.2.4 Data analysis

2.2.4.1 Identification of particle types and components

The mass spectra were analyzed using MS-Analyze and ENCHILADA (Environmental Chemistry through Intelligent Atmospheric Data Analysis) (Gross et al., 2010), two software programs designed to analyze ATOFMS data. This allowed further size resolved analysis of the particles or subclasses of particles using queries. Queries allow the identification of the compounds of particles by searching for the corresponding m/z values.

ENCHILADA was used for a cluster analysis of the analyzed particles. It groups similar spectra into clusters using different clustering algorithms (Giorio et al., 2012). Each resulting cluster is representative for a particle type that show specific m/z values and ratios of intensities. This study used k-means, a clustering algorithm that allows to identify and define an adequate number of clusters. This method was used because only a small number of clusters were expected due to the high resemblance of the spectra. Similar clusters were manually merged together. The data presented in this study were analyzed with respect to engine thrust if enough data was obtained, i.e. the A-PRIDE 5 measurements. The particles were characterized with emphasis on the occurrence of metallic compounds. If interference with other peaks from other ions was observed, peaks from isotopes of the metallic compounds were used to discriminate.

Ratios of Elemental to Total Carbon (EC/TC) ratio were derived from ATOFMS data adopting a method using the sum of relative peak areas associated with EC and TC presented by Ferge et al. (2006). TC is defined as the sum of Organic Carbon and EC. After subtracting peaks from known inorganic compounds from the average spectrum, TC was calculated by adding up all remaining peak areas. The list of inorganic compounds from Ferge et al. (2006) was modified by adding the metallic compounds found during our analysis. EC was calculated from the average spectrum by adding up all peak areas at m/z $12i$, $12i + 1$, $12i + 2$ and $12i + 3$ (with $I = 1$, 2, etc.). The ratio of the obtained peak areas for EC and TC then yielded the presented EC/TC values. In this study from Ferge et al. (2006), the described method above was found to agree with a

standardized thermo-optical approach using the NIOSH 5040 (Birch, 2002) method and a thermo-coulometric method, especially for samples with low inorganic content. Additionally, the particles were classified into 'EC' and 'ECOC' using criteria such that the 'EC' class composed particles with no OC whereas the 'ECOC' class composed particles showing both EC and OC signals. This was done by applying an "exclusive" classification query on the obtained positive spectra in MS-Analyze. This means, if particles are sorted into the first class for which they meet the prescribed requirements, they are then excluded from further classification. The first class comprised the 'EC' particles. In order to define the 'ECOC' class, two additional classes, 'EC + K' and 'K noEC noOC', had to be defined and classified in advance because of the ambiguous association of the *m/z* +39 peak with organic compounds and potassium. This excludes the possibility of having particles in the 'ECOC' class that contain EC and potassium and no OC. The first additional class labelled as 'EC + K' was defined to show a peak at *m/z* +39 and the EC peaks. The second one labelled as 'K noEC noOC' was defined to show solely *m/z* +39 while not showing the other peaks associated with OC. Note that the presence of EC in the 'K noEC noOC' class is excluded due to the previous classification. Eventually, the 'ECOC' class was defined to consist of the remaining particles showing any combination of the OC and EC markers.

2.2.4.2 Particle size analysis

The vacuum aerodynamic diameter (d_{va}) of the analyzed aircraft exhaust particles was measured by the ATOFMS. Note that the ATOFMS was not used to determine the size distribution that is representative for the aircraft PM emission. d_{va} was converted into electrical mobility diameter (d_m) in order to compare d_{va} to continuous size measurements performed by a Scanning Mobility Particle Sizer (SMPS, TSI, Model 3936, TSI Inc., St. Paul, USA) system, which measures d_m. The calculation was done using equation [50] in DeCarlo et al. (2004):

$$d_{va} = \frac{\rho_p}{\rho_0} \frac{d_m}{\chi_v^{3/2}}$$

(2.1)

ρ_p and ρ_0 are the particle density and unit density respectively and χ_v is the dynamic shape factor in the vacuum or free molecular regime. ρ_p was assumed to be equal to the particle material density of soot. This holds for aggregates with no internal voids such as freshly evolved unaltered soot particles, and is supported by TEM pictures from aircraft soot (Liati et al., 2014; Boies et al., 2015). A value for ρ_p of 1.87 g/cm^3 as estimated from our previous effective density measurement on aircraft exhaust (Abegglen

et al., 2015) was assumed. For comparison, other reported values of ρ_p range from 1.7 ±0.7 g/cm^3 for non-volatile components of diesel soot (Park et al., 2004) up to 2.03 g/cm^3 (Braun et al., 2004) also for diesel soot. χ_v was calculated using equations [2.1] and [2.2] as described in Shapiro et al. (2012) with the information on particle mass and d_m also measured during A-PRIDE 5. Because the mass of a particle with a certain size additionally depends on engine thrust the mass was averaged over the measured thrusts. The value of χ_v is size-dependent and was calculated using a power law fit taking into account values obtained at different d_m.

2.3 Results and discussion

This chapter first gives an overview on the size of the investigated particles from aircraft engine exhaust. Information on the chemical composition of the identified particle types is provided, followed by Elemental Carbon (EC) to Total Carbon (TC) ratios determined from ATOFMS data. Lastly, the occurrence of metal compounds detected in the particles is presented and potential sources thereof are discussed. The latter is supported by ICP-MS analyses of the most likely sources that are engine jet fuel, lubrication oil and engine wear.

During the A-PRIDE 5 campaign, the ATOFMS was not able to record both the positive and the negative ion spectra because of instrumental restrictions. Thus, the vast majority of the data consists of positive spectra. It was possible to measure negative spectra during the last two days of the campaign, by switching the polarities of the high voltages applied to the flight tubes of the ATOFMS.

2.3.1 Size of investigated particles

The upper panel of Figure 2.2 depicts the averaged thrust dependent SMPS measured size distributions shown as the particle mobility diameter emitted by Turbofan 1, collected via both, the PM line and the Annex 16 line. The lower panel shows the particle mobility diameter, calculated from the measured aerodynamic size as explained in section 2.2.4.2, of the hit (i.e. chemically analyzed) particles by the ATOFMS during A-PRIDE 5. It can be seen that the ATOFMS measures the right hand tail of the mobility size distribution as shown in the upper panel. This is because the ATOFMS cannot size and analyze particles down to the mobility size of the majority of the emitted particles.
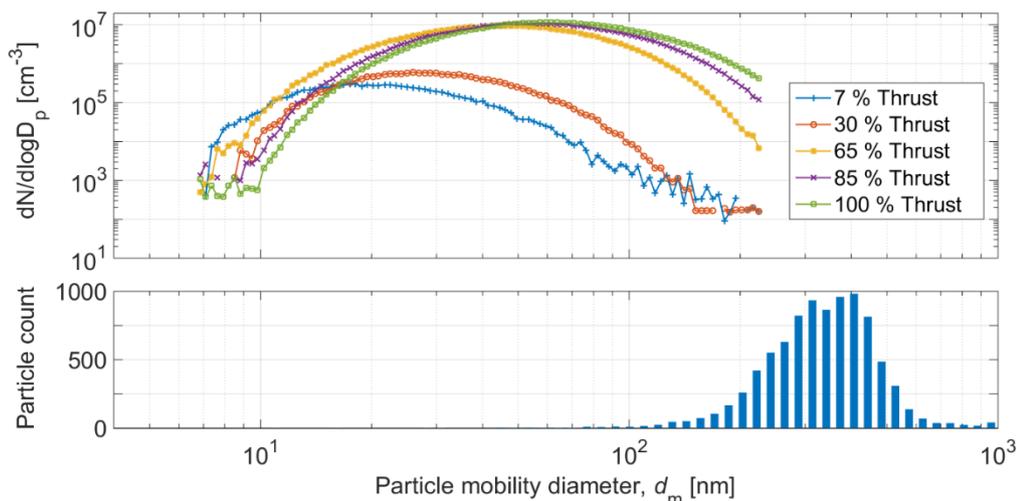
Figure 2.2   Size distributions measured by SMPS on the sampling line (top) and the calculated size of the chemically analyzed particles by the ATOFMS (bottom).

The mode of the SMPS size distribution lies between 20 nm and 50 nm. By extrapolating the data assuming a log-normal distribution, the measured mobility size ranges from <10 nm to ~600 nm. The mobility size distribution of particles that were hit by the ATOFMS, however, shows a mode at ~400 nm and ranges from ~100 nm to ~700 nm. The exact mobility size distribution of the hit particles remains unknown because the material density was assumed, and if it was higher, then the values calculated for d_m would be lower. Nevertheless, the size distributions would still differ in their modes. Although no differences in the chemical composition of the investigated particles were observed within the investigated size-range, our results cannot be reliably extrapolated towards smaller particles. Thus, the results presented in the following are only representative for the largest particles in the exhaust.

Experimental studies on the ice nucleating ability of soot showed that larger particles generally are more efficient INP than smaller ones (DeMott, 1990; Diehl & Mitra, 1998). Thus, assuming that particles emitted by aircraft engines are INP active, their efficiency to act as INP probably also increases with increasing particle size. Because we sampled the largest particles with the ATOFMS, they can be considered the fraction that is likely to be the most important regarding the contribution of aircraft emissions to INP.

2.3.2 Chemical characterization

2.3.2.1 Turbofan 1

For the spectra recorded during A-PRIDE 5 the clustering and the subsequent interpretation of the particle types were affected by the lack of negative mass spectra. In total 9875 positive spectra were obtained. The analysis of the mass spectra obtained from particles emitted yielded six clusters.

The mass spectra of the three major clusters (Figure 2.3) represent >99 % of the particles, the most prominent of which comprised ~93 % of all chemically analyzed particles. They were classified as: (1) **EC-Na-metal** particles with a strong EC signature (m/z +12, +24, +36, +48, +60, +72, +84) and small peaks of inorganic compounds from sodium (m/z +23) and metals such as chromium (m/z +52) and iron (m/z +56). A small hydrocarbon peak (m/z +37 (C_3H)) indicates the presence of organic carbon (Spencer & Prather, 2006). The **K-Na-Ca-EC** particle type (2) has a dominant potassium signal (m/z +39, +41) and a sodium peak while including the EC pattern. This cluster comprises ~5 % of the particles. The **Ca-Al-K-metal** particle type (3) comprises ~2 % of the particles. It is dominated by a calcium peak at m/z +40 followed by an aluminium peak at m/z +27, a potassium and an iron peak. The peak at m/z +27 could also be attributed to organic carbon e.g. C_2H_3 (Silva & Prather, 2000; Pastor et al., 2003). However, from our EC/TC determination (see 2.3.3) and the fact that other possible markers OC such as m/z +29, 37, 43, 51 and 63 (Spencer & Prather, 2006) are very weak, we assume the influence of OC to be smaller than from aluminium. The peak at m/z +56 is probably a mixture of Fe and CaO because of the small peak at m/z +57 that indicates the presence of CaOH. The three remaining clusters comprised 16 or less particles each and showed mainly one single peak at m/z +41 or +42 or +43. As a consequence, these clusters were assigned as unclassified.
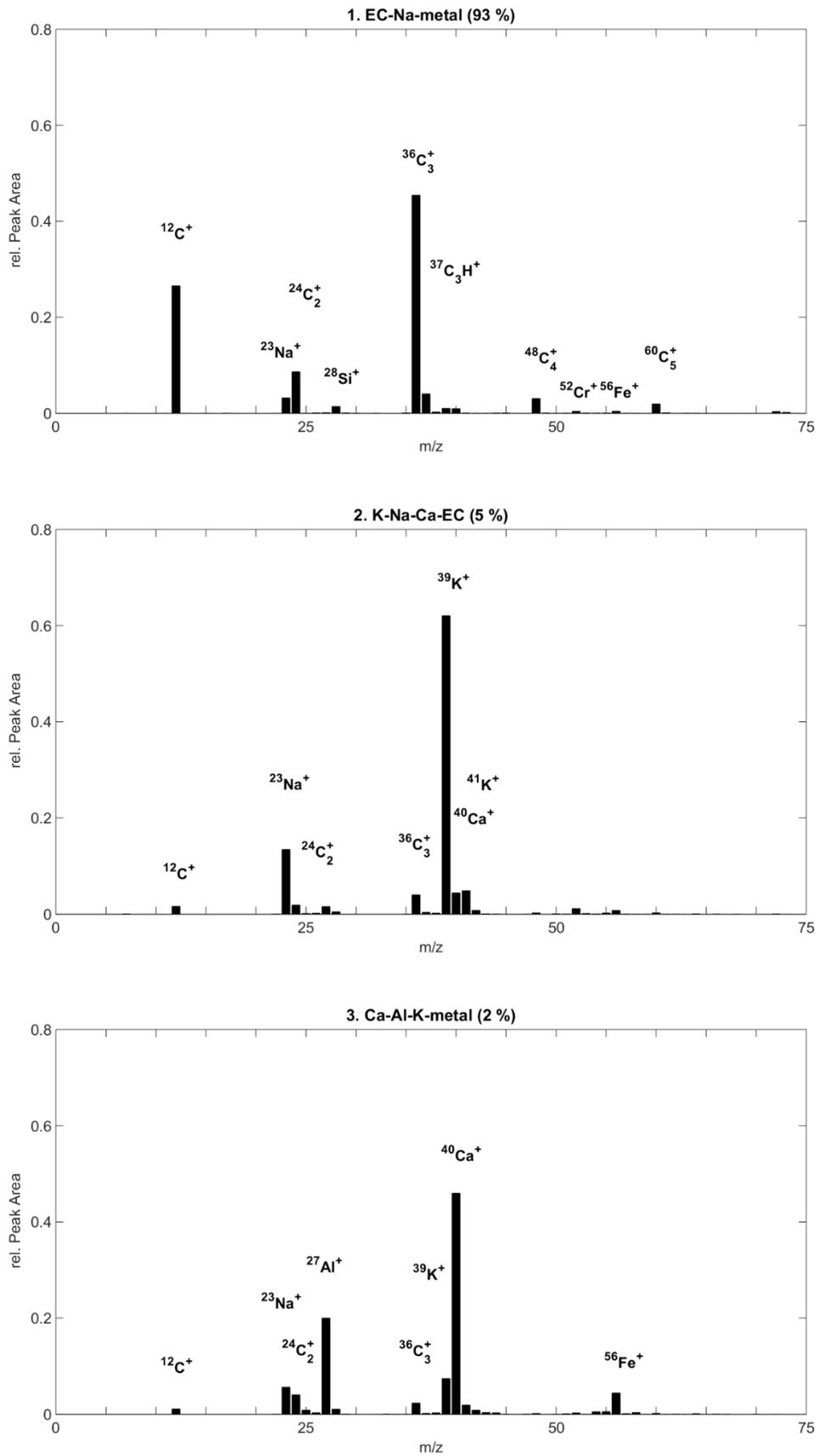
Figure 2.3   The three major clusters (i.e. particle types) identified for particles emitted by Turbofan 1 during A-PRIDE 5.

By switching the polarities of the ATOFMS' flight tubes, we were able to analyze negatively charged ions and constituents, though the small number of spectra meant a cluster analysis was not meaningful. Instead, the average spectrum of the negative ions is presented in Figure 2.4. Although it cannot be used to identify the individual particle types, it provides insight into most abundant chemical compounds of the analyzed particles. The average spectrum in terms of relative peak area mainly shows the presence of EC (peaks at m/z +12, +24, +36, etc.) and a prominent sulfate signal (m/z +97) which is a typical marker for sulfuric acid. The average negative spectrum agrees with the positive ions that also indicate a prevailing presence of EC.

Because all three major positive ion clusters indicated the presence of EC, we conclude that the detected inorganic and metallic compounds were all internally mixed with soot particles. This is also supported by the average negative spectrum and the fact that only 2.5 % of the spectra did not show at least one peak associated with EC. Considering that some fraction of soot can effectively act as INP (Cozic et al., 2008) and that a dominant fraction of ice residuals in cirrus clouds contain metal compounds (Agrawal et al., 2008) the presented findings support the assumption that aircraft engine emissions can act as INP.
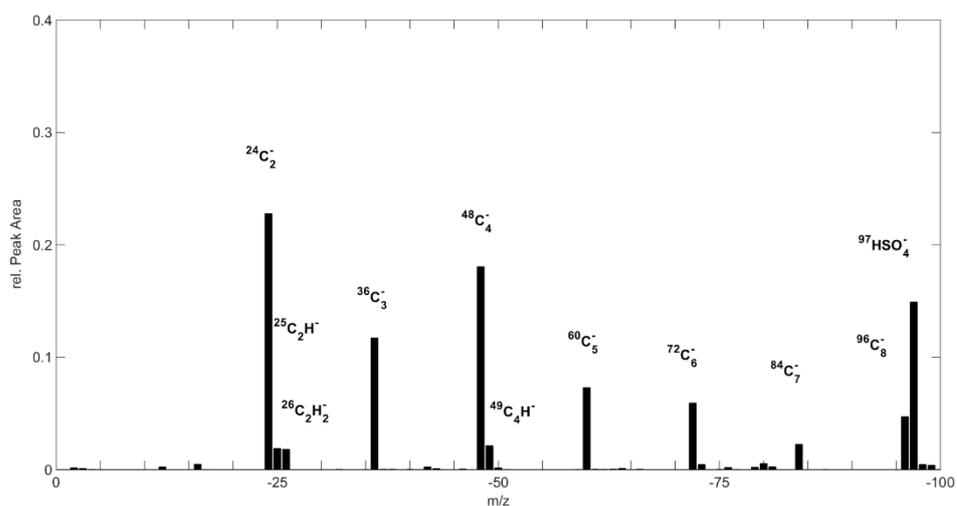
Figure 2.4   Average negative spectrum from the spectra collected from Turbofan 1.

2.3.2.2 Turbofan 2

The cluster analysis resulted in nine clusters, of which five were considered to represent the main particle types (Figure 2.5). Although the total number of spectra recorded was only 317, we still discuss the similarities to the particles sampled from Turbofan 1.

The **EC-S-metal** (1) was the most abundant particle type ($\sim$44 %). Besides the very prominent sulfate ion peak at m/z -97 and the EC pattern, this cluster also shows the presence of metal compounds such as aluminium (m/z $+27$), chromium (m/z $+52$), iron (m/z $+56$) and molybdenum (m/z $+92 - +100$). The **metal-N** particle type (2) is made up from $\sim$16 % of the particles, and shows mainly metal compounds with the most pronounced peaks arising from magnesium (m/z $+24 - +26$), iron, barium (m/z $+138$) and calcium (m/z $+40$). Magnesium was identified due to the absence of other EC peaks and the matching isotopic ratio. Nitrate was identified by the peak at m/z -46. Here, the EC pattern is only present in the negative spectrum. The **EC-Na-metal** (3) particle type comprises $\sim$25 % of the particles, and is similar to cluster (1). However, this cluster includes a more intense sodium ion peak at m/z $+23$ and a lower intensity of the sulfate peak thus the negative EC pattern is relatively more pronounced. The **Ca-metal-Na-EC** particle type (4) shows combined features of EC, metal compounds and sodium. This cluster comprises $\sim$8 % of all particles, and contrary to the other clusters it shows strong signals of both barium and barium oxide. The peak at m/z -95 assigned to CH_3SO_3 is ambiguous due to the absence of other peaks from sulfates. Also, this peak has not been observed in other clusters. The peak at m/z -95 could potentially be associated with PO_4 or $NaCl_2$, however both are unlikely. The presence of phosphate is implausible because no peaks from PO_2 and PO_3 at m/z -63 and -79 were detected. For $NaCl_2$, an additional peak from its isotopes at m/z -93 would be expected. The **EC-S-K-metal** particle type (5) comprises $\sim$6 % of the particles. This cluster has very similar features to cluster (1) and (3), despite its dominant sulfate peak at m/z -96 instead at m/z -97. The spectra of the remaining four clusters make up $\sim$1 % of the total. These clusters all showed peaks associated with EC except for one. This cluster only contained one spectra with a major peak at m/z $+90$ potentially from zirconium and a peak at m/z -17 (OH).
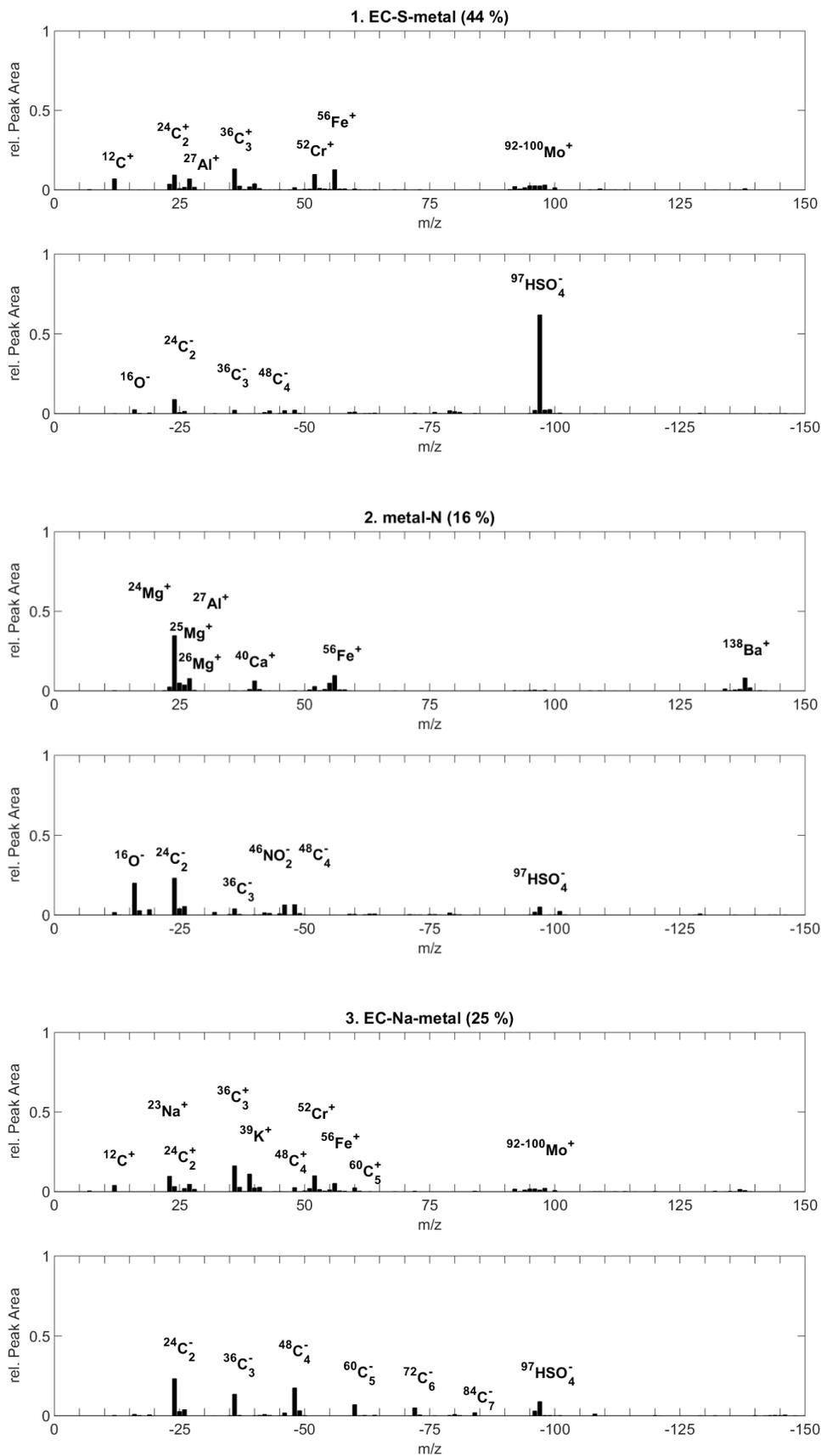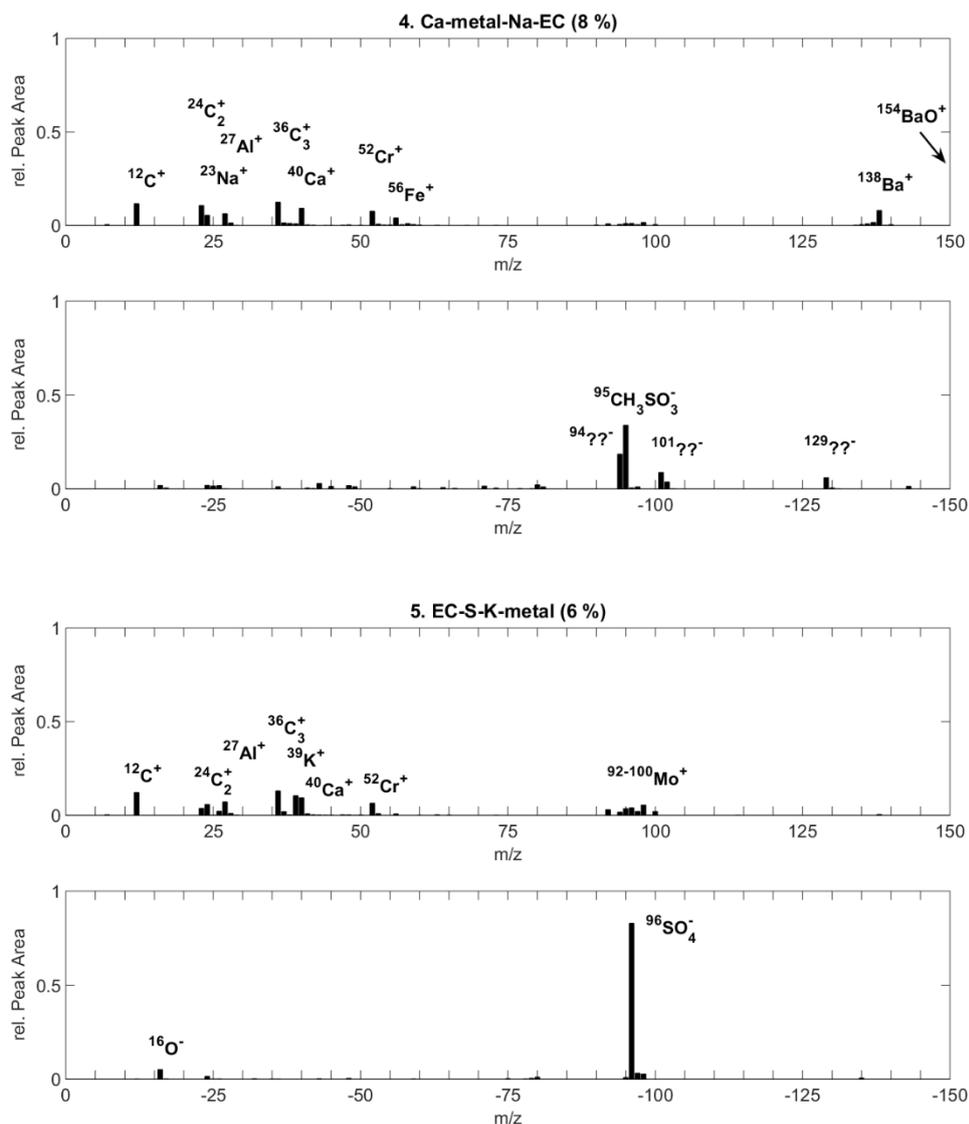
Figure 2.5   Cluster analysis from the particle spectra measured from Turbofan 2, including both positive and negative spectra.

2.3.2.3 Mixed-flow Turbofan

The cluster analysis of the spectra obtained from the particles emitted by the Mixed-Flow Turbofan yielded six clusters, of which three were already identified for Turbofan 2. One cluster comprised only one particle. The two new clusters, metal-S-EC cluster (2) and metal cluster (5), are depicted in Figure 2.6. The total number of particles chemically analyzed from this engine was 466.

The **EC-Na-metal** (1) particle type was very similar to cluster (3) from Turbofan 2. Also, contribution by this cluster, 23 %, is comparable. The **metal-S-EC** (2) particle type comprises 18 % of the particles. This cluster shows similar peaks to cluster (1),

with less pronounced EC and more intense sulfate peaks. Moreover, it has more pronounced peaks from vanadium (*m/z* +51) and molybdenum (*m/z* +92 – +100). The **EC-S-metal** particle type (3) looked like cluster (1) from Turbofan 2. Both the clusters comprised the same number fraction of particles (44 %). The **metal-N** particle type (4) made up of 12 % of the total particles and was similar to cluster (2) for the Turbofan 2 with a distinct presence of barium. The **metal** particle type (5) comprised ~3 % of the particles. As shown, a combination of metal compounds was detected in the positive spectrum, though the negative spectrum has major peaks that cannot be unambiguously assigned. The peak at *m/z* −43 is assigned to C_2H_3O thus organic carbon (Spencer & Prather, 2006). The peak at *m/z* −42 was assigned to CNO, which could emerge due to the simultaneous occurrence of nitrogen and carbon in the particle (Mauney et al., 1984; Kolaitis et al., 1989). The peak at *m/z* −184 could not be assigned. This cluster does not have peaks associated with EC in either of the spectra. The sixth cluster (one spectra) had a dominant sulfate peak at *m/z* +97 and a peak at *m/z* −25 that could not be assigned.
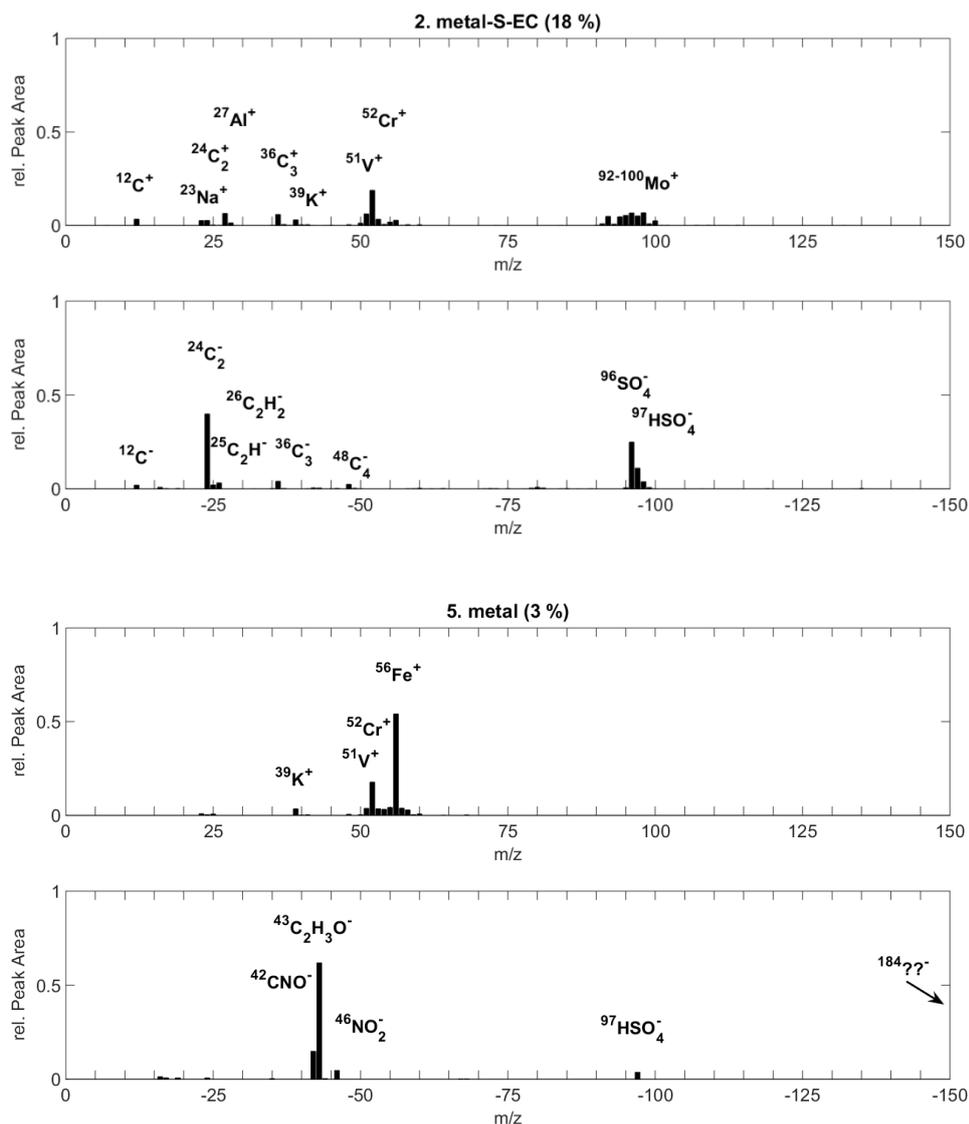
Figure 2.6   Cluster analysis from the particle spectra measured from the Mixed-Flow Turbofan.

2.3.2.4 Ambient background particles

ATOFMS measurements of ambient background particles were conducted in order to investigate if ambient aerosol particles could influence the engines measurements. The 325 background particles were sampled overnight from 6:00 p.m. to 9:00 a.m. without an engine running following the test run of the Mixed-Flow Turbofan which ended at 2:30 p.m. The sampled particles represent the aerosol particles that enter the test cell with the air that is consumed by the engine as it is running. During the overnight sampling, the airlocks of the test cell were left open to allow a passive exchange of the outside air with the test cell air. The sampling conditions did not fully reflect the situa-

tion during engine runs due to the flow of air through the test cell during engine runs caused by the operation of the engine.

In total, the analysis yielded seven clusters. The two main particle types are displayed in Figure 2.7. The **K-N-Na** particle type (1) made up ~54 % of the analyzed particles and has dominant potassium peaks at *m/z* +39 and +41 and a smaller sodium peak. Calcium (*m/z* +40) is also present though this peak can be the result of the potassium signal at *m/z* +39 (especially if it is very intense) to which the ATOFMS is very sensitive (Healy et al., 2013) that sometimes causes a peak to be registered at *m/z* +40. The negative spectra are dominated by ion peaks from nitrate at *m/z* −46 and −62. A likely association with K, Na and N is dust (Jeong et al., 2011) probably from the road and the freeway nearby. The **S-Fe-K** particle type (2) comprises ~18 % of the spectra. This cluster is dominated by a strong sulfate (*m/z* −97) signal and the presence of iron (*m/z* +56) and potassium ions (*m/z* +39). This cluster also has a weak EC signature in the positive mass spectra. Consequently, these particles could be aged remainders from aircraft exhaust emitted during previous engine tests or soot particles from sources nearby. The **K-N-EC** particle type (3) was made up of ~7 % of the total spectra, and differed from the other clusters by its EC pattern up to C_9^- (*m/z* −108) mixed with potassium and nitrate. Additionally, it showed the metal compounds manganese (*m/z* +55) and iron (*m/z* +56). The **Fe-N** particle type (4) comprised ~7 %. In contrast to the other clusters it displayed a prominent iron peak in the positive spectrum. The negative spectrum was dominated by a strong nitrate signal and a smaller sulfate peak. The **Ca-N-Na** particle type (5) comprised ~6 % of the particles. Except for the presence of calcium instead of potassium, it had similar features than the K-N-Na particle type (1). The **EC-Ca-K-S** particle type (6) made up ~5 % of the total particles. It depicted low intensities of carbonaceous peaks from EC mixed with potassium, calcium and sulfate, and in contrast to the other clusters, phosphate was detected, mainly at *m/z* −79 (PO_3) and to a smaller extent at *m/z* −63 (PO_2). These peaks are commonly associated with soil dust (Silva et al., 2000). The **K-CN-N** particle type (7) only comprised ~2 % of the total particles. This cluster had a strong potassium peak in the positive mass spectrum and peaks from organic nitrogen (*m/z* −26 (CN), −42 (CNO)) and nitrate (*m/z* −46, −62) in the negative spectra.
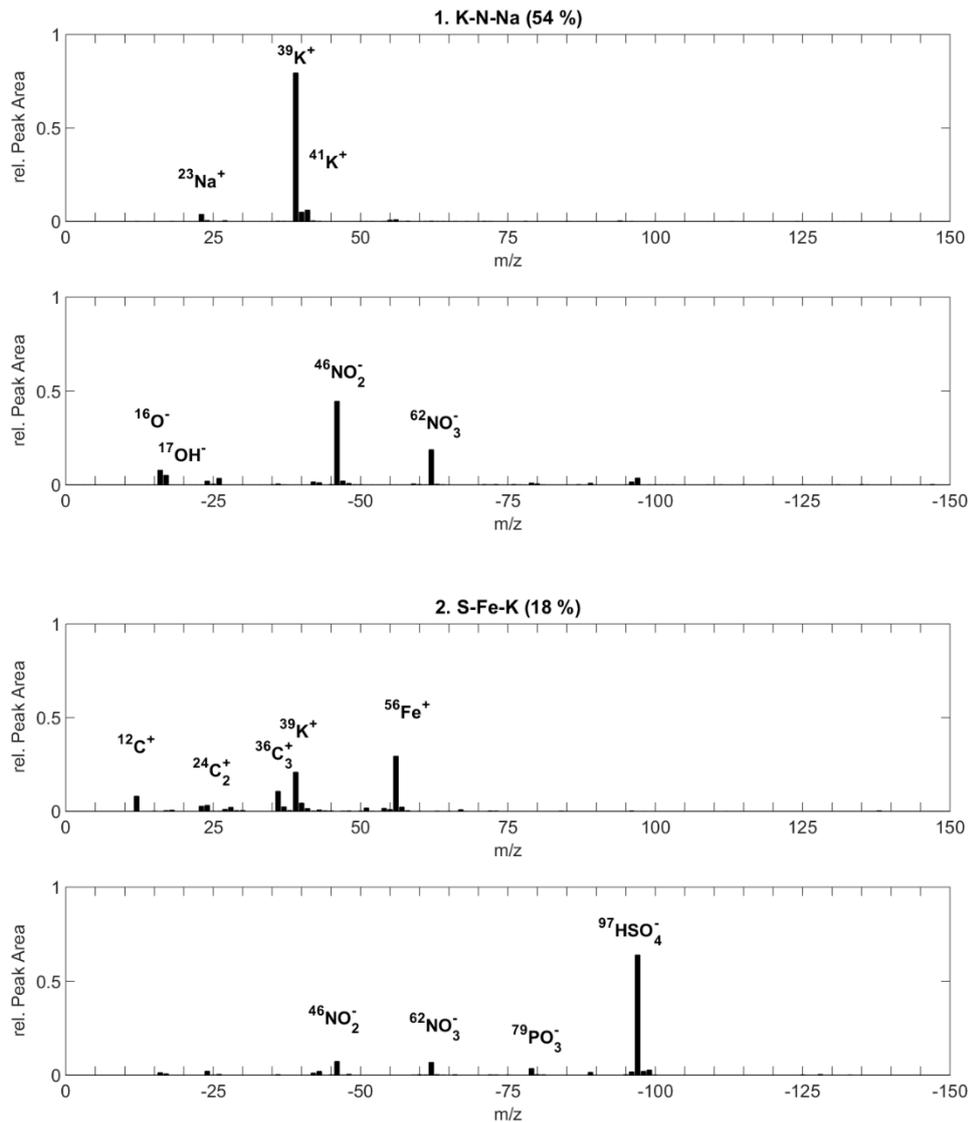
Figure 2.7   Main clusters from the spectra collected during the ambient background measurements performed in the test cell without an engine running.

2.3.2.5 Comparison of the identified particle types

The particle types identified as described in the previous sections are summarized in Figure 2.8. As mentioned, only small differences were recognized between clusters (1), (3) and (5) from Turbofan 2 and clusters (1) and (3) from the Mixed-Flow Turbofan. They are similar to the EC-Na-metal particle type (cluster 1) presented for Turbofan 1 with respect to the positive ion spectra. Also, the common particles types from Turbofan 1 and the Mixed-Flow Turbofan were similar in terms of number fractions. Together, these particle types made up more than 75 % of the measured particles for both engines. These engines mainly differed from Turbofan 1 because the metal-N particle type was not observed. However, this is probably due to missing the negative spectra.

The analysis of the ambient particles revealed that they do not resemble the exhaust particles sampled during engine runs. None of the particle types identified for ambient background aerosol were found in the aircraft exhaust, and only ~12 % of the background particles depicted a clear EC pattern in both the positive and the negative spectrum. These particles were assumed to be remainders from previous engine tests or from sources in the vicinity such as landing and starting aircraft or cars. Most similarities exist between the K-N-EC (cluster 3) from the ambient background particles and the EC-Na-metal particle type from the engines, though the K-N-EC particle type clearly differs by the presence of nitrate and markers for organics. Nitrate however, is found in the metal-N particle type from the aircraft engines. As all ambient particle types contained nitrate, it is possible that nitrate from ambient aerosol is partly responsible for the nitrate detected in the particles emitted by the engines. The opposite is the case for the metallic compounds, especially aluminium, magnesium, vanadium, chromium, iron, manganese, molybdenum and barium. These are detected in most particle types of the engine emissions but only in clusters 2 and 4 from the ambient background particles.

Because of the different particle types detected in the exhaust and in the background, we assume that the background particles did not influence our exhaust measurements. In a similar way, we assume that the engine emissions from the engines have influenced the ambient background particles in terms of metallic compounds to some extent. Moreover, most metal compounds do not vaporize in the engine combustor according to their boiling points that exceed the maximum combustor temperature. Thus, the redistribution of the metal compounds from ambient particles onto the soot particles in the aircraft engine could only happen by coagulation. However, this would require the metallic compounds to be externally mixed in the ambient aerosol and the cluster analysis showed that this was not case. Possible exceptions are calcium, sodium and magnesium that have boiling points below the temperature in the engine potentially allowing their vaporization within the combustor. Calcium and sodium can both be abundant in ambient atmospheric aerosol and were also detected in our background measurements. So they can possibly be vaporized and redistributed via condensation onto the soot particles within the engine. However, considering the large difference in particle concentration between ambient air and exhaust their influence is thought to be minor.
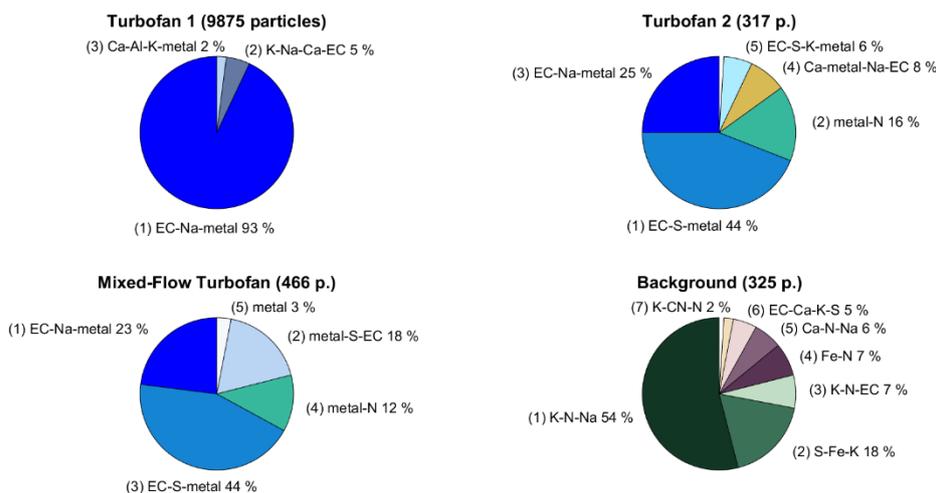
Figure 2.8   Major particle types of the investigated aircraft engines and from the ambient background aerosol. The number in parentheses is the cluster number as described in the corresponding chapter.

2.3.3 Elemental carbon to total carbon ratio

Elemental Carbon to Total Carbon (TC) ratios were obtained from positive ATOFMS spectra by adapting the method presented in Ferge et al. (2006). The thrust-dependent EC/TC ratios for Turbofan 1 are displayed in Figure 2.9. The thrust percentage refers to the predicted thrust at sea level. Depending on the applied thrust, the EC/TC ranged from 0.96 to almost 1 for the ATOFMS measured particles. The EC/TC ratios for the emissions from Turbofan 2 and from the Mixed-Flow Turbofan were averaged over all measured thrust levels because the majority of the spectra were obtained at thrusts <30 %. These were 0.89 and 0.83 respectively, considerably lower than for Turbofan 1. Thus, for this engine the relative contribution of OC to TC is lower than for the other two engines. We attribute these differences to different engine deteriorations. For comparison, Ferge et al. (2006) reported EC/TC values for soot samples of two different sizes of 0.90 (±0.05) and 0.89 (±0.03) from a diffusion flame generator using the setting for high organic loadings and 0.94 (±0.01) and 0.93 (±0.02) using the setting for low organic loadings.

For comparison, we calculated the number of particles associated with EC, classed as particles with peaks at m/z −36, −24, −12, +12, +24 and +36. The number fractions of EC-containing particles emitted by Turbofan 1, Turbofan 2 and the Mixed-Flow Turbofan were 97.5 %, 94.5 % and 96.7 %, respectively. The bypass air (ambient air), which

is mixed with the exhaust before sampling, did not influence the fraction of EC-containing particles in the exhaust of the Mixed-Flow Turbofan. This may be explained by the relative low particle concentration in the bypass air compared to the emitted soot particles in the core-flow.
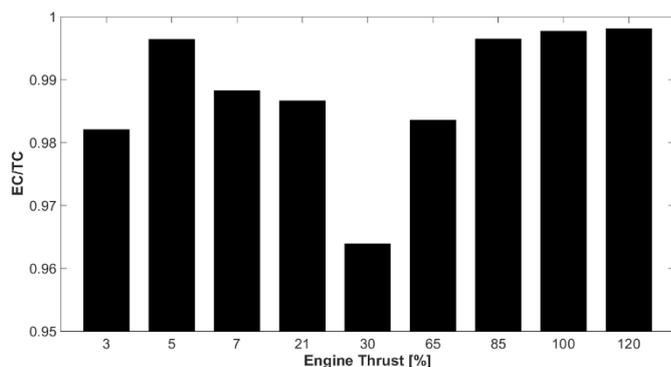
Figure 2.9   Thrust dependent elemental carbon to total carbon values measured by the ATOFMS for Turbofan 1.

For more detailed information on the carbon-containing particles, MS-Analyze was further used to classify the particles into 'EC' and 'ECOC' classes for Turbofan 1, depicted in Figure 2.10 according to the applied thrust. The 'K noEC noOC' class consisted mainly of spectra from particles that showed a dominant potassium peak. The number fraction of the 'ECOC' class defined in this way has to be considered as the lower limit because of the possibility that some of the particles from the 'EC + K' class are actually 'ECOC'. The number fraction of the 'EC' class ranges from ~50 % to ~90 % where the highest values are found to occur in the high thrust range (85 % to 120 %). The 'K noEC noOC' class and 'unclassified' particles are the only ones not associated with EC, and were generally higher at thrust ≤30 %. For the same engine type at thrust >30 %, Brem et al. (2015) found that the influence of aromatic species from the Jet A-1 fuel on soot emissions decreases with increasing thrust. They attributed the observed maximum influence at 30 % thrust to the less efficient combustion of aromatics, due to lower combustor temperatures and pressures. If this applies to organics in general, more organic material would remain unburnt at low thrust than at high thrust, which would explain the generally higher fraction of particles in the 'EC' class at higher thrusts.
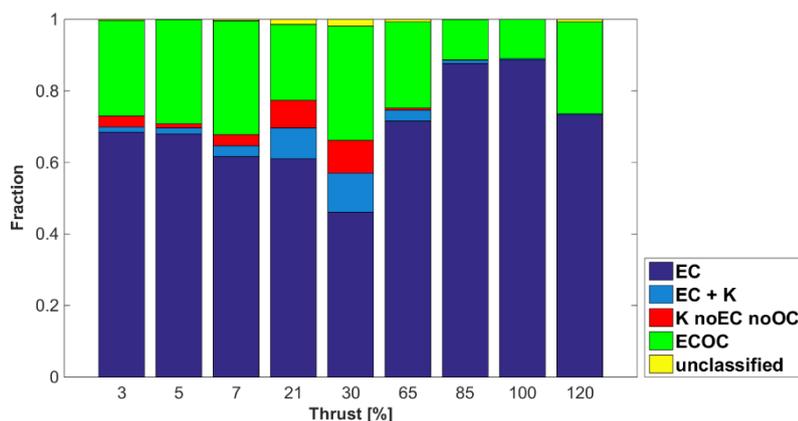
Figure 2.10   Thrust dependent fraction of the particles from Turbofan 1 classified into 'EC' and 'ECOC'. The 'EC + K' and the 'K noEC noOC' classes were needed to define the 'ECOC' class.

2.3.4 Metals

2.3.4.1 Occurrence of metallic compounds

The following metallic compounds were detected to be internally mixed with the exhaust soot particles: molybdenum, calcium, sodium, iron, copper, barium, chromium, aluminium, silicon, magnesium, cobalt, manganese, vanadium, nickel, lead, titanium and zirconium. These metallic compounds were detected for all three engines investigated except for zirconium that was not found in particles from Turbofan 1. Also, indium, boron, selenium, arsenic, tin, wolfram, antimony and gadolinium were analyzed, but they were not detected except for antimony, boron and wolfram that were identified on only four or less particles each. In general, one or more metallic compounds were detected in a single particle, and the fraction of particles emitted by Turbofan 1 containing at least one, two, three and four metals was 36.3 %, 19.9 %, 10.5 % and 3.2 %, respectively.

The metals, number fractions and relative peak areas for the three engines and the ambient background measurements are listed in Table 2.1. The fractions for the Turbofan 1 engine are sorted according to the applied thrust to reveal variations between the different phases of an aircraft taxiing (low thrust), cruise (medium thrust) and take-off (high thrust). However, the actual cruise conditions are only partly represented by the medium thrust range as measured in the test cell because the inlet pressure and the fuel flow do not correspond to typical cruise values due to different ambient pressures and temperatures as well the missing forward speed. Moreover, the turbine case can shrink due to

the low temperatures in high altitudes. Consequently, the results presented in the following for the medium thrust range should only be considered as indicative and not be used directly to describe the aircraft PM emissions during cruising conditions of an actual flight. The relative peak area value given in parenthesis is normalized for each metallic compound so that the largest peak area measured corresponds to 1 for that metal. The data for Turbofan 2 and the Mixed-Flow Turbofan were averaged over all measured thrusts because not enough particles were sampled for a thrust-dependent analysis. However, ~80 % of these particles were sampled at thrusts <30 % corresponding largely to the low thrust range.

For Turbofan 1 the fraction of particles containing molybdenum is largest at the high thrust range. Also within this range, the fraction was found to increase with increasing thrust. For calcium, sodium, iron, copper and barium the corresponding fractions of particles containing the metal are largest at low thrust and decrease with increasing thrust. A reason for this behavior could be the increasing total particle concentration with increasing thrust. If the total amount of these metallic compounds did not increase with increasing thrust, then relatively fewer particles are affected by them. For chromium, aluminium, silicon, magnesium, cobalt, vanadium, nickel, lead and titanium the corresponding fractions of particles containing the metal are largest at medium thrust. In contrary to the other compounds the peak area values from calcium and barium are not largest at that thrust range where the fraction of calcium- and barium-containing particles are largest. This indicates that the amount of calcium and barium present on each particle is largest at medium thrust despite the smaller number fractions.

The fractions of metal-containing particles were generally higher for Turbofan 2 and the Mixed-Flow Turbofan than for the Turbofan 1 with the largest differences found for molybdenum, barium, chromium, aluminium, manganese, magnesium, vanadium, nickel and lead. As discussed in the next section, kerosene, lubrication oil, grease and engine wear are potential sources of these metals. One reason for the larger fractions is the possible difference in oil and grease consumption. Turbofan 2 and the Mixed-Flow Turbofan generally have a higher oil consumption than Turbofan 1. Another reason for the differences in the measured metal-containing fractions are variations thereof over time for the same engine. Alloys sometimes consist of heterogeneously distributed compounds. Thus, if wear takes place and an engine alloy frets, its individual compounds are unevenly released. Also, it is known that an engine can exhibit an increased abrasion of wearing components during the beginning of the first operation

after it was overhauled. From the work scope of the investigated engines, we do not expect this to be the case; however, increased abrasion can still not be entirely excluded.

Table 2.1   *Number fraction in percent of spectra from particles emitted by the Turbofan 1, Mixed-Flow Turbofan and Turbofan 2 engines and from ambient background showing peaks indicating the presence of the corresponding metal compound. For Turbofan 1 the values are pooled into low (3 % – 7 %, idle/taxi), medium (20 % – 65 %, cruise) and high (85 % – 120 %, take-off) thrust range, and the value in parenthesis is the average peak area normalized to the largest value for each metal.*

| | Turbofan 1 | | | | | |
Element	Low thrust	Medium thrust	High thrust	Mixed-Flow Turbofan	Turbofan 2	Background
Molybdenum	5.3 (0.52)	5.9 (0.73)	9.6 (1.00)	55.9	36.7	1.9
Calcium	32.4 (0.61)	16.2 (1.00)	1.8 (0.04)	22.3	39.1	23.1
Sodium	29.1 (1.00)	22.6 (0.41)	4.3 (0.06)	50.2	51.1	34.5
Iron	22.5 (1.00)	8.4 (0.49)	0.7 (0.06)	33.0	35.5	11.1
Copper	2.9 (1.00)	0.4 (0.50)	0.0 (—)	2.6	6.7	2.5
Barium	0.5 (0.16)	0.3 (1.00)	0.1 (0.08)	3.7	16.5	2.2
Chromium	2.7 (0.10)	17.2 (1.00)	3.6 (0.18)	72.3	52.0	5.2
Aluminium	3.1 (0.21)	8.4 (1.00)	1.0 (0.03)	8.3	13.5	15.1
Silicon	0.4 (0.36)	2.1 (1.00)	0.1 (0.15)	0.2	0.9	4.3
Magnesium	0.6 (0.46)	1.7 (1.00)	0.3 (0.04)	16.6	20.8	3.1
Cobalt	0.5 (0.83)	1.4 (1.00)	0.4 (0.93)	1.7	2.8	1.5
Manganese	0.3 (0.84)	0.9 (1.00)	0.1 (0.02)	17.5	17.4	8.9
Vanadium	0.4 (0.89)	0.7 (1.00)	0.1 (0.04)	9.4	9.2	3.4
Nickel	0.4 (0.12)	0.6 (1.00)	0.1 (0.04)	10.7	19.3	8.3
Lead	0.1 (0.36)	0.4 (1.00)	0.0 (—)	1.3	0.9	2.5
Titanium	0.0 (—)	0.2 (1.00)	0.0 (—)	0.0	0.9	0.0
Zirconium	0.0 (—)	0.0 (—)	0.0 (—)	0.9	0.6	0.3

The presented fractions of particles that contain metallic compounds are lowest for the ambient background particles except for silicon, lead and aluminium of which the latter shows similar values as Turbofan 1. It is likely that the ambient background measurements were influenced to some extent by the engine test run conducted beforehand on the Mixed-Flow Turbofan.

2.3.4.2 Potential sources of metals

ICP-MS was conducted to investigate potential sources of the metallic compounds identified in the exhaust particles of aircraft engines. It was applied as quantitative element screening on a) kerosene (Jet A-1 Fuel), b) engine lubrication oil (Mobile Jet II) and c) debris from engine wearing components.

Kerosene and oil samples were taken from the batch actually consumed by the aircraft engine during the A-PRIDE 5 campaign. As a reference for material from engine wearing components, a sample of debris collected on the blades of the High Pressure Turbine (HPT) of another Turbofan 1 engine type was used. The HPT is located downstream of the combustor where the collected debris was carried and accumulated by combustor air. The influence of oil on the emissions is thought to be less important compared to kerosene because of the much smaller amounts consumed. The ratio of kerosene to oil consumption is estimated to be $\sim$5000 ($\pm$1500):1 for the tested engines at medium thrust. Another potential source of the identified metal compounds in the exhaust not analyzed herein is grease mainly applied to rotating engine parts.

The detection of silicon in kerosene and oil samples using ICP-MS was not possible because of the analytical procedure applied. The concentrations in milligram per kilogram [mg/kg] of the most abundant metallic elements in Jet A-1 Fuel and Mobile Jet II Oil are shown in Table 2.2. 'Others' comprise compounds with >0.1 mg/kg each, including barium, manganese, arsenic, tin, nickel and molybdenum detected in both fuel and oil, whereas indium and boron were solely detected in fuel, and selenium solely in oil. Besides the metallic elements, sulphur and phosphorus were also detected in both samples.

Table 2.2   Concentrations in milligram per kilogram [mg/kg] of the most abundant metallic elements in the sampled Jet A-1 Fuel and Mobile Jet II Oil detected using ICP-MS.

Element	Jet A-1 Fuel	Mobile Jet II Oil
Calcium	113.15	30.82
Vanadium	3.59	1.82
Aluminium	3.08	4.35
Lead	1.98	>0.1
Iron	1.69	1.77
Magnesium	1.46	2.25
Titanium	1.45	6.01
Sodium	1.05	1.28
Copper	0.96	(—)
Antimony	>0.1	1.15
Chromium	(—)	1.09
Others	4.91	5.3

The elements that were detected in the solid HPT debris using ISP-MS are shown in Table 2.3 in percentage of mass [wt%]. It only lists the elements detected in the exhaust particles as well, covering 98.2 % of the mass of the HPT debris sample. The debris was stored in 95 % ethanol and 5 % isopropyl alcohol after sampling and a potential contamination from the solvent cannot be excluded. The suspension was homogenized and dried directly before the analysis.

Table 2.3   Mass fractions in percentage of mass [wt%] and 95 % Confidence Intervals (CI) of elements in solid residue from the HPT debris obtained using ICP-MS.

Element	Mass fraction, CI (95 %)
Silicon	60.1, [59.6, 60.6]
Calcium	12.2, [11.4, 13.0]
Sodium	5.03, [4.88, 5.18]
Iron	5.00, [4.65, 5.35]
Aluminium	4.90, [4.60, 5.20]
Magnesium	4.00, [3.90, 4.10]
Nickel	3.43, [3.39, 3.47]
Chromium	0.90 [0.86, 0.94]
Titanium	0.63 [0.61, 0.65]
Manganese	0.39 [0.39, 0.40]
Lead	0.39 [0.37, 0.41]
Copper	0.48 [0.45, 0.51]
Cobalt	0.32 [0.32, 0.33]
Barium	0.20 [0.17, 0.23]
Molybdenum	0.18 [0.17, 0.19]
Vanadium	0.051 [0.049, 0.053]
Zirconium	0.017 [0.012, 0.022]

The ICP-MS of the HPT debris was used to reveal compounds that are probably from engine wear. Although the identified compounds were part of the combustion air, the actual composition of the HPT debris as it was collected has not contributed to the combustion process like kerosene and oil. From empirical values the HPT debris was accumulated in the engine over an estimated engine operation time of about 20 000 hours to 30 000 hours. During this time, huge amounts of air passed through the HPT, allowing the accumulation of compounds not only from engine processes such as wear or kerosene and oil residues but probably also from ambient aerosol collected during flight. We assume silicon, calcium and sodium from ambient air to cause the large weight fractions in the HPT debris.

A potential source of aircraft engine wear are the so-called honeycomb structures that are built into in the compressor region of the engine downstream the combustor. The honeycomb structures are a wearing part made out of 'Hastelloy X'. The chemical composition and the corresponding weight fractions in percentages (in parenthesis) according to the specification sheet (Haynes, 1997) is: Ni (47), Cr (22), Fe (18), Mo (9), Co (1.5), W (0.6), Mn (≤1), Si (≤1), B (≤0.008). It was suggested that wear from 'Hastelloy X' contribute to debris collected in the HPT. However, the relative large amounts of molybdenum in 'Hastelloy X' and the large fractions of exhaust particles containing molybdenum are not reflected in the small mass fraction of molybdenum found in HPT debris. Thus, the amount of 'Hastelloy X' in HPT debris is probably rather small. Nevertheless, this does not exclude the possibility of wear from 'Hastelloy X' to contribute to the metals identified in the exhaust particles. Below, we discuss potential sources for each individual metal compound identified in the emitted engine particles based on the ICP-MS analyses.

Exclusively engine wear:

Zirconium was detected in small amounts in HPT debris but not in kerosene or oil. It is known to be used as thermal barrier coating in aircraft engine parts (Miller, 1997). **Cobalt** was detected in small amounts in HPT debris and it is used in 'Hastelloy X' but not in kerosene or oil.

Mainly engine wear:

Iron was detected in substantial amounts in HPT debris and in 'Hastelloy X'. It was also found in kerosene and in oil. Compared to other metallic compounds such as vanadium, lead, magnesium and titanium the number fraction of iron-containing particles was relatively high whereas the amounts detected in kerosene and oil were similar. Thus, we assume this difference in the fraction to be caused by the higher iron content in HPT debris and in 'Hastelloy X'. **Copper** was detected in kerosene and it is used in 'Hastelloy X'. Copper was not detected in oil. It was detected in the exhaust particles mainly in combination with iron indicating engine wear as a major source. **Chromium** was detected in HPT debris and 'Hastelloy X' contains a weight fraction of 22 %. Chromium is widely used in engine parts e.g. aircraft turbine blades and alloys. It was detected in oil but not in kerosene. **Nickel** is the most abundant constituent of 'Hastelloy X' and it shows a substantial weight fraction of 3.4 % in HPT debris. Only very low concentrations of nickel were detected in kerosene and in oil. **Molybdenum** is a main

constituent of 'Hastelloy X'. However, in aerospace, molybdenum disulfide is widely used in grease for lubrication applications where metal to metal contact exists. It can be converted directly to molybdenum metal when heated (Epshteyn & Risdon, 2010). The highest number fraction of molybdenum-containing particles was measured at maximum thrust when grease consumption and engine wear are likely to be highest. Only small quantities were detected in kerosene and oil. We therefore assume molybdenum to originate mainly from engine wear and grease.

Mainly kerosene:

Barium was detected in kerosene and in oil. It is not supposed to be present in any engine parts. As a side note, because of its capability to reduce soot emissions in combustion processes (Howard & Kausch Jr, 1980) by acting as a nucleation core for soot it was earlier used as an antismoke additive in kerosene to reduce the smoke number. **Vanadium** was detected in kerosene and in oil. Engine wear as a source of vanadium is not significant due to the very small amount detected in HPT debris. **Lead** was mainly detected in kerosene and only small amounts were detected in oil and in HPT debris. Lead is not used in any engine parts. **Titanium** was detected in kerosene and in oil. Small amount were also detected in HPT debris may be from alloys used in the compressor of aircraft engine upstream of the combustor. **Calcium** and **sodium** were both detected in kerosene and in oil. Especially calcium was detected in relatively large concentrations. Both kerosene and oil probably contribute to their existence in the exhaust particles. Calcium and sodium originating from engine wear can be excluded because they are not used in any engine part. However, ambient aerosol as an additional source is also possible because of the large fraction of ambient background particles containing calcium and/or sodium and the possibility that these compounds are redistributed onto the exhaust particles via gas phase processes.

No main source identified:

Aluminium was detected in kerosene, in oil and in HPT debris. Also, it is used in many engine parts. **Silicon** could not be identified with the ICP-MS method applied to the kerosene and oil samples. Small amounts of silicon are used in many materials used in aircraft engines. **Magnesium** was detected in oil, kerosene and HPT debris which are all potential sources. **Manganese** was detected in small amounts in oil, kerosene and HPT debris. Similar to silicone, it is commonly present in engine parts.

2.4 Summary and conclusions

We investigated the chemical composition of single particles emitted from three different in-production aircraft turbofan engines using an ATOFMS. Particle types were identified using a data mining software enabling the analysis of atmospheric mass spectra. The bulk EC/TC ratios were determined. Furthermore, we determined the fractions of particles that contained metallic compounds. In order to identify sources of the metallic compounds ICP-MS was performed on samples from Jet A-1 fuel, Mobile Jet II Oil and debris from engine wearing components. The particles that were analyzed by the ATOFMS represented a subset of the non-volatile emissions composing only the largest particles due to instrumental restrictions.

Depending on engine type, 94.5 % to 97.5 % of the particles contained EC. All three engine types showed common similar particle types regarding their chemical composition and corresponding number fractions. These were the EC-Na-metal, EC-S-metal and Metal-N particle types. The thrust-dependent EC/TC ratio of the emissions from Turbofan 1 ranged from 0.96 up to more than 0.99 depending on the applied thrust. The EC/TC ratio of the emissions from Turbofan 2 and the Mixed-Flow Turbofan were 0.89 and 0.83, respectively. These results were not influenced by whether the engine was a core flow engine or a mixed flow engine.

Particles containing metallic compounds were all internally mixed with the soot. The following compounds were detected in particles from all engines: Cr, Fe, Mo, Na, Ca, Al, V, Ba, Co, Cu, Ni, Pb, Mg, Mn, Si and Ti. Zr was only detected in the Turbofan 2 and Mixed-Flow Turbofan exhaust. The fraction of metal-containing particles was lower for the Turbofan 1 than for the Turbofan 2 and the Mixed-Flow Turbofan. To identify sources of the metallic compounds ICP-MS analyses were carried out. Traces of all compounds were detected in kerosene and/or in oil except for Co and Zr. We conclude that cobalt and zirconium can possibly be used as tracers for aircraft exhaust because they solely originate from engine wear. This accounts especially for cobalt because it was detected in the emission from all of three engines investigated. However, this would require further research because other combustion sources of cobalt- and zirconium-containing soot particles cannot be completely excluded. Nevertheless, the combined usage of cobalt and zirconium is rather limited. To use the other detected compounds as tracers is not possible because diesel and petroleum are produced from crude oil just like kerosene. Thus, the metallic compounds detected in kerosene can be expected to be found in other fuels and emissions, too.

In general, an unambiguous source apportionment of the metal compounds detected in the engine exhaust particles is difficult because of multiple reasons. Most importantly, many metals are detected at least in small amounts in multiple potential sources. Also, there is the possibility that the element composition of fuel and lubrication oil varies due to contamination in storage and distribution facilities (Fordyce & Sheibley, 1975). Further, it is difficult to quantitatively relate the sources to the compounds detected in the particles. On the one hand, the relative extents of the contribution from the individual sources are not exactly known. This is partly because aircraft engines are a complex system where exploration of chemo physical processes of trace elements within the engine is difficult because no direct observations are possible. On the other hand, the ATOFMS data is non-quantitative and represent only the largest exhaust particles. Moreover, engine wear and oil and grease consumption are not constant over the lifetime of an aircraft engine.

The implications of our results are of importance due to the potential of metal-containing particles to act as INP and consequently impact cirrus cloud properties and thus global climate (Cziczo et al., 2013). As a minimum value among the three engines, 36 % of the particles emitted by Turbofan 1 contained at least one metallic compound. These finding suggest that aircraft engine emissions are a considerable source of potential INP in the atmosphere. The fractions of metal-containing particles did not show a size-dependence in our investigated size-range in agreement with Demirdjian et al. (2007) who also did not observe appreciable differences in the chemical composition between small and large soot particles sampled directly behind an aircraft gas turbine engine. The majority of the actual aircraft emissions take place in the upper troposphere where the aircraft operate mainly at cruise conditions that can be mimicked to a certain degree with the medium thrust range measured in the engine test cell. Our thrust-dependent analysis revealed that for most of the metallic compounds, the measured averaged relative peak areas were found to be largest at medium thrust. This indicates that also their contents in the soot particles are largest at medium thrust. If the presence of a metallic compound is responsible for the INP activity of a soot particle, a larger content probably enhances its effectiveness to act as INP. At medium thrust range, measurements of the emissions showed high particle concentrations of $>10^6$ cm^{-3} (Abegglen et al., 2015) for Turbofan 1. In the upper troposphere the concentration of INP is typically on the order of <0.01 cm^{-3} (DeMott et al., 2003) where additional INP would contribute substantially to the total number, potentially resulting in

significant cirrus modifications (Hendricks et al., 2005; Hendricks et al., 2011). Therefore, to understand the connection between metal-containing particles from aircraft exhaust and ice nucleation, we recommend investigation of the ice-nucleating properties of non-volatile aircraft emissions. In addition, our findings provide information with regard to human health effects from aircraft PM emissions potentially caused by trace metals contained in the particles.

Acknowledgements

3 Effective density and mass–mobility exponents of PM in aircraft turbine exhaust: Dependence on engine thrust and particle size

M. Abegglen[a], L. Durdina[b,c], B. T. Brem[b,c], J. Wang[b,c], T. Rindlisbacher[d], J. C. Corbin[a], U. Lohmann[a] and B. Sierau[a]

[a] *Institute for Atmospheric and Climate Science (IAC), ETH Zurich, Zurich, CH-8092, Switzerland*
[b] *Laboratory for Advanced Analytical Technologies, EMPA, Dübendorf, CH-8600, Switzerland*
[c] *Institute of Environmental Engineering (IfU), ETH Zurich, Zurich, Switzerland*
[d] *Swiss Federal Office of Civil Aviation (FOCA), Bern, CH-5003, Switzerland*

This chapter is adapted from the original article.

Abstract

The mass and electrical mobility size of nascent soot generated by aircraft turbine engines were measured using a Differential Mobility Analyzer, a Centrifugal Particle Mass Analyzer and a Condensation Particle Counter in series. The measurements were conducted with a commonly used engine at a maintenance facility at Zurich Airport, Switzerland. The aircraft engine under investigation was a CFM56-7B26/3. The used standardized sampling system conforms to the emission certification regulations captured by the "Society of Automotive Engineers, Aerospace Information Report 6241". Effective densities of the aircraft soot were derived using measured power-law relationships between mass and electrical mobility size. The values ranged from 530 kg/m^3 to 1865 kg/m^3 depending on the particle mobility size and applied engine thrust. Trends in these effective densities suggest that the size of primary particles in the soot aggregates increase with increasing thrust. The mass-mobility exponents associated with these engine thrusts ranged from 2.54 to 2.79 and 1.86 to 2.32 for thrust levels above 30 % and below 30 %, respectively. Comparison with a second engine, a CFM56-5B4/2P, revealed higher effective densities for particles smaller than 40 nm.

3.1 Introduction

Knowledge of soot particle morphology is of major research interest because it influences several factors, such as the particles transport behavior, radiative properties (Zhang et al., 2008; Bond et al., 2013) and health effects (Lighty et al., 2000; Maricq & Xu, 2004). The most important aerosol-radiation interaction of soot is its ability to absorb solar radiation over a broad range of wavelengths and thereby directly cause a warming in the atmosphere and a dimming at the surface (Bond et al., 2013). This light absorption stands in contrast to most other atmospheric aerosol particles, which scatter solar radiation. Furthermore, aerosol-cloud interactions lead to indirect radiative effects by altering cloud properties, such as changing the albedo and lifetime of clouds (Boucher et al., 2013). The overall effects of soot on the global radiation budget are likely to be positive but they still remain very uncertain (Bond et al., 2013; Myhre et al., 2013) due to the variety in morphology amongst soot particles (Burtscher, 2005). Thus, morphology is one of the key quantities influencing soot aerosol optical and cloud forming properties (Boucher, 2013). Also, the morphology of soot particles does not remain constant over their atmospheric lifetime (Miljevic et al., 2012) which is typically one to two weeks (Cape et al., 2012). Regarding health effects arising from soot, several

epidemiological studies had concluded that diesel engine soot is likely to be carcinogenic to humans (Ris, 2008). Recently, the importance of a better characterization of diesel exhaust from cars for investigating effects on humans was mentioned and targeted (Wierzbicka et al., 2014).

Carbonaceous aerosol particles formed during various combustion processes largely differ in their physical properties such as size, mass, and morphology. The term soot will be used hereafter to describe the carbon containing particle agglomerates from fossil fuel combustion, excluding any organic species chemically combined with carbon such as hydrogen, nitrogen, oxygen, phosphorus, sulfur, chlorine, etc. (Petzold et al., 2013). Soot particles grow from nearly spherical primary particles into fractal like aggregates. The primary particles emerge by nucleation and combine by coagulation to form chain like structures. Hence, their morphology depends on the number and size of the primary particles as well as on the degree of compaction. A value often used to describe the morphology of fractal particles is the fractal dimension (Maricq, 2007; Shapiro et al., 2012). It relates the number of primary particles to the radius of gyration of the aggregate (Friedlander, 2000).

The combustion process itself determines the initial morphology of soot particles. Once emitted, changes in the morphology of soot particles take place as the particles age due to atmospheric processing (Zhang et al., 2008). This involves condensation of secondary organic substance and/or water onto the particles as well as the collapsing of the chain-like primary structure, which results in a more spherical and compact aggregate (Zhang et al., 2008; Ghazi & Olfert, 2013; Ma et al., 2013). Therefore, information on the initial fundamental properties of these particles is needed to understand these changes in the atmosphere and their effects on the Earth's radiation budget.

Aircraft soot emissions have been increasingly studied because of the above mentioned issues, combined with the fact that air traffic is steadily growing. In terms of revenue passenger kilometers, commercial air traffic is predicted to increase from 5 billion in the year 2010 to 13 billion in the year 2030 (ICAO, 2013). During taxiing and takeoff, the emissions are released in the vicinity of the airport in large quantities, directly affecting the local air quality and thereby the airport personnel and local population. During flight, emissions take place in the upper troposphere where they are a unique source of fresh soot. These emissions can lead to contrail formation and cirrus-cloud initiation, influencing the radiative budget of the Earth. These processes are still little studied due to the difficulties in collecting such particles (Popovicheva & Starik, 2007). To properly

capture, quantify, and explore the implications of such aircraft emissions, it is important to know how physical properties such as effective density and morphology of the soot particles change at various thrust levels.

The physical properties of fresh combustion generated Particulate Matter (PM) have been investigated for diesel engines, emissions from which are thought to be similar to aircraft emissions regarding their physical properties: Onasch et al. (2009) conducted measurements on fresh exhaust from a CFM56-2-C1 aircraft engine. The soot particles showed a similar morphology and fractal nature as diesel and premixed flame soot of the same mobility diameters. The measured size range however, was significantly lower for the aircraft engine than for diesel cars.

Limited data is available on the effective density of the PM emitted by aircraft engines. Onasch et al. (2009) calculated an effective density of $\sim 1000\,\mathrm{kg/m^3}$ for particles from a CFM56-2-C1, using combined measurements of the aerodynamic diameter in the free molecular regime and mobility diameter at rated thrusts >56 %. The same method was applied by Timko et al. (2010b) investigating a PW308 turbine. Values for the effective density found ranged from $710\,\mathrm{kg/m^3}$ to $840\,\mathrm{kg/m^3}$ for rated thrusts <50 %. However, as both of these measurements were based on aerodynamic diameters in the free molecular regime, the calculated effective density is differently defined than the hereinafter presented effective density resulting in an error when estimating particulate mass (Eq. (45) (DeCarlo et al., 2004)). A need for mobility based effective density measurements therefore remains.

To derive morphological information of aerosol particles such as radius of gyration, number of primary particles, density and fractal dimension, the most common techniques use light scattering measurements (Sorensen, 2001; Khalizov et al., 2009; Kiselev et al., 2010) and/or Transmission Electron Microscopy (TEM) (Mathis et al., 2005; Mazaheri et al., 2013). Effective density measurements may also provide information on morphology if the particle material density is known. Moreover, mobility based effective densities allow commonly available mobility size measurements to be translated into mass based PM emission indices. Various other studies have characterized aircraft PM (Rogers et al., 2005; Cheng et al., 2008; Williams et al., 2012). Still, it remains challenging to sample exhaust from an aircraft engine at a distance close enough to avoid mixing with ambient aerosol and associated condensation of organic substances onto the soot particles. For instance, Petzold et al. (2005) simulated an

aircraft engine using a modified combustor which had the same thermodynamic data and emissions.

We present comprehensive size selected mass measurements on freshly emitted soot particles, sampled directly (<1 m) behind a CFM56-7B26/3 engine, which is widely used on commercial aircraft. The engine has a single annular combustor for improved emissions and is applied in Boeing 737 aircraft. In order to measure fresh, non-aged aircraft exhaust, a distance of 1 m behind the engine exit plane has been previously shown to sample only refractory carbon soot particles (Onasch et al., 2009). Two different sampling probes, a single-point and a multi-point probe, were used which span the entire thrust and measured size distribution range. The measurements were conducted at an engine maintenance facility at Zurich airport, Switzerland. The test facility is run by SR Technics, a company that provides technical solutions to airlines. The presented measurements were performed during the so called "dedicated" tests. This means that a rented aircraft engine was run according to the needs of the scientific staff. The measurements provide information on the effective density and the mass-mobility exponent, which is associated to the fractal dimension. Note that (Durdina et al., 2014) also used effective density values of the CFM56-7B26/3 engine exhaust particles to derive thrust dependent PM line losses for the presented experimental set-up and discussed them accordingly. We also compare with literature data (Johnson et al., 2015) for the same engine type and effective density measurements from a CFM56-5B4/2P engine, a dual annular combustor turbofan for low NO_x emissions.

3.2 Fractal aggregates

Objects with infinite dilation (self-similarity) symmetry are called fractal. Real objects are also termed fractal if they show self-similarity over the scale of their size. Soot particles often display self-similarity on different length scales, and are therefore often described by a fractal scaling law relating aggregate size and number of primary particles to describe their morphology (Schmidt-Ott, 1988).

Equation (1) defines a relationship for fractal aggregates (Sorensen, 2011) consisting of spherical primary particles. It relates the number of primary particles (N_{pp}) to the radius of gyration (d_g) normalized to the diameter of the primary particles (d_{pp}). This implies self-similarity of the agglomerates over a certain range for N_{pp}.

$$N_{pp} = k \, (d_g/d_{pp})^{D_f} \qquad (3.1)$$

where D_{f} is the fractal dimension and k is a scaling prefactor.

Assuming the electrical mobility size scales with N_{pp}, it can analogously be written:

$$N_{pp} \sim d_m^{D_m} \tag{3.2}$$

In which d_{m} is the electrical mobility diameter and D_{m} is the mass-mobility scaling exponent.

As the primary particles are formed in the same environment, their size and density can be assumed constant (Schmidt-Ott et al., 1990), the particle mass (m_{p}) is then directly proportional to N_{pp}:

$$m_{\mathrm{p}} = C * d_{\mathrm{m}}^{\varepsilon} \tag{3.3}$$

C is a constant with units [kg/m$^{\varepsilon}$], and is called the mass-mobility prefactor. ε is the mass-mobility exponent, which is related to the arrangement of the primary particles within the agglomerate such that $\varepsilon = 1$ and $\varepsilon = 3$ correspond to an infinite long straight chain-like structure and a compact sphere-like structure, respectively (Friedlander, 2000).

When reporting densities of fractal aggregates, the effective density is a convenient quantity because it can be determined experimentally. Knowledge of d_{m} and the corresponding mass yields the effective density ρ_{eff} (DeCarlo et al., 2004):

$$\rho_{\mathrm{eff}} = \frac{m_{\mathrm{p}}}{d_{\mathrm{m}}^3} \frac{6}{\pi} = \frac{C * d_{\mathrm{m}}^{\varepsilon} * 6}{d_{\mathrm{m}}^3 * \pi} = C' * d_{\mathrm{m}}^{(\varepsilon - 3)} \tag{3.4}$$

C and C' are related such that:

$$C' = C * \frac{6}{\pi} \tag{3.5}$$

Where C' is a constant with the same units as C [kg/m$^{\varepsilon}$]. It is called the density-mobility prefactor. Hereafter, we always refer to the mass-mobility prefactor C.

3.3 Experimental methods

The Aviation Particle Regulatory Instrumentation Demonstration Experiment 5 (A-PRIDE 5) was conducted in the aircraft engine test cell at SR Technics, Zurich airport. We present data collected from 3$^{\mathrm{rd}}$ to 24$^{\mathrm{th}}$ of August 2013 during the dedicated measurement tests.

3.3.1 Measurement procedure

A dedicated measurement run consisted of a warm-up (WU) procedure typically comprising four thrust levels including ground idle (GI) followed by a sequence of up to twelve thrust levels on a decreasing power curve (Table 3.1). Prior to each measurement run, the engine must perform a warm up procedure consisting of a sequence of ascending thrust levels. The purpose was to heat up the probe by stabilizing the engine at these values for about five minutes. The engine test points were set using the combustor inlet temperature T3. T3 was used to predict the thrust at sea level (static thrust the engine would produce at 1 atm ambient pressure and 15 °C) and can therefore exceed 100 %. Here, we report this predicted thrust. Because the ambient temperature and pressure varied between engine runs, the actual thrust produced by the engine varied at constant T3. Note that different definitions of thrust exist which are reported in other publications referenced later herein. Durdina et al. (2014) and Lobo et al. (2015) used a definition of thrust that corresponds to a thrust corrected to International Standard Atmosphere (ISA) conditions at sea level (p = 101 325 Pa, T = 288.15 K) whereas Johnson et al. (2015) used the uncorrected measured thrust in the test cell.

The observed ranges for each engine thrust level are given in Table 3.1. At each thrust level a number of mass scans were performed at different particle mobility sizes (see Section 3.3.3). The number of test points measured varied from day to day because the engine test cycles varied in duration and thrust settings. In addition to the dedicated measurement runs, it was possible to measure during post-maintenance engine runs of customer engines.

Table 3.1   Overview of test points, corresponding measured thrusts and number of measurements per selected mobility size conducted. Ground idle (GI) and warm ups (WU) are conducted in addition to the desired test points.

Test point	Thrust [%]	Number of measurements per thrust level at the selected mobility size [nm] (columns) and engine thrust (rows)									
		20	30	40	50	60	75	90	100	125	150
GI	2.5 ±0.5	1	4	1	3	1	3	1	–	–	–
WU7	7 ±1	1	1	–	2	–	2	–	1	–	–
WU65	66 ±2	1	4	1	6	1	3	1	3	–	–
WU85	84 ±2	1	3	–	4	1	3	–	2	1	–
0	118 ±6	–	3	2	–	1	2	–	2	–	2
1	104.5 ±6	3	9	4	12	6	6	2	10	2	10
2	99.5 ±4	1	2	4	4	–	–	–	2	1	6
3	94 ±6	4	13	8	10	4	5	2	8	8	7
4	85 ±1	1	3	1	3	1	2	2	3	1	5
5	67 ±1	3	10	13	9	4	6	2	8	3	5
6	33 ±2	3	6	4	9	2	7	1	7	–	–
7	26 ±1	–	2	3	8	1	2	–	–	–	–
8	22 ±1	–	1	2	8	1	1	–	–	–	–
9	7 ±1	–	1	3	8	2	1	–	–	–	–
10	6 ±1	–	3	3	18	–	1	–	–	–	–
11	3 ±1	–	4	3	17	2	2	–	–	–	–

3.3.2 Sampling system

Figure 3.1 shows a schematic of the experimental set-up during the campaign. The used standardized sampling system conforms to the emission certification regulations captured by the "Society of Automotive Engineers, Aerospace Information Report 6241" (SAE, 2013). Exhaust was sampled by either of two 8 mm ID sample probe at a distance of ~0.7 m behind the engine and then distributed to the different instruments. The probe inlet was oriented to sample parallel to the exhaust stream. The probe was vertically movable to adapt to different types of engines. In addition to the earlier used single point probe, a multipoint probe was introduced on the 17th of August. It consisted of 24 selectable sampling nozzle positions in a cruciform pattern. Twelve of them were used to provide a representative sample directly at the engine exit plane according to the

emissions certification requirements (ICAO, 2008). The sampled engine exhaust was drawn through tubing heated to 160 °C in order to prevent condensation and/or evolution of secondary organic aerosol in the sampling system.

The sampling system consisted of two main measurement lines: the PM line and the Annex 16 line. The PM line was diluted with synthetic air (grade 5.0) by a factor of ten using a Dekati ejector dilutor (Dekati, Model DI 1000, Dekati Ltd., Kangasala, Finland) and was kept at 60 °C. This line was primarily used to measure non-volatile PM number and mass. "Annex 16" refers to the standard: "International Civil Aviation Organization Annex 16: Environmental Protection, Vol. 2 – Aircraft Engine Emissions" (ICAO, 2008), which prescribes standards and procedures for the certification of aircraft emissions. The undiluted Annex 16 line was heated to 160 °C and was primarily used for measurements of gaseous emissions.

For our measurements, a split was installed in the Annex 16 line leading into a 60 °C heated line. The advantage of measuring on the Annex 16 line was a stronger signal due to a higher particle concentration as well as being unaffected by changes in the dilution ratio in the PM line during some experiments. Downstream of the Nafion dryer (Perma Pure, Model PD-100T-24MSS, Perma Pure LLC, Toms River, USA) the flow was no longer heated. The conditions for nucleation were monitored by measuring temperature (T) and relative humidity (RH) downstream of the dryer.

The flow was then distributed into ancillary Annex 16 instruments, into a Scanning Mobility Particle Sizer (SMPS, TSI, Model 3936, TSI Inc., St. Paul, USA) system, and into the two identical Differential Mobility Analyzer (DMA; TSI, Model 3081, TSI Inc., St. Paul, USA)-Centrifugal Particle Mass Analyzer (CPMA; Cambustion Ltd., Cambridge, UK)-Condensation Particle Counter (CPC; TSI, Model 3776; TSI Inc., St. Paul, USA) systems. The two DMA-CPMA-CPC systems described below sampled from the Annex 16 line except for the two first dedicated measurement days.
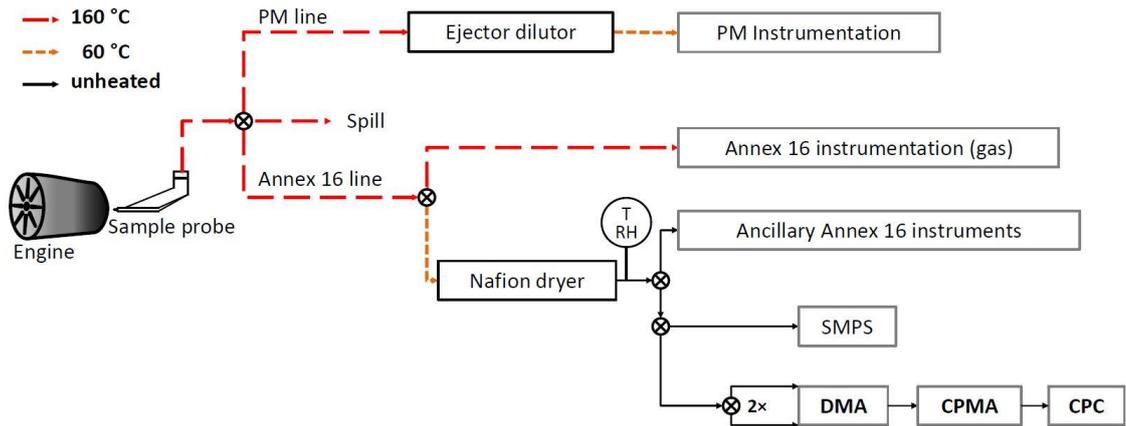
Figure 3.1   Schematic of the experimental set-up during A-PRIDE 5. The effective density measurements were performed using the two identical DMA-CPMA-CPC systems.

3.3.3 DMA-CPMA-CPC systems

Performing one DMA-CPMA-CPC scan at a fixed particle size and aircraft engine thrust eventuating in one mass distribution takes between 4 and 7 minutes. The exact duration depends on the resolution of the scan and the average mass of the single particles under investigation. Due to time restrictions on the engine runtime and scarcity of repetitions, it was only possible to scan a limited number of sizes (see Table 3.1). In order to record a more comprehensive data set, two DMA-CPMA-CPC systems were set up in parallel. During the entire campaign, the monitored T and RH downstream of the dryer ranged from 22 °C to 28 °C and 20 % to 38 %, respectively. This results in a maximum dew point temperature below 12 °C when taking the extreme values, so that condensation of liquid water is unlikely to have taken place.

The DMA was used to select particles of a desired electrical mobility size. The sheath and the aerosol flow rates were set to 12.0 l/min and 1.5 l/min, respectively. The DMA was part of an electrostatic classifier model 3080 (TSI Inc., Shoreview, USA). Before the particles entered the systems they were treated with an aerosol neutralizer (model 3077, TSI Inc., Shoreview, USA) to apply a known charge distribution to the particles (Wiedensohler, 1988). This ensures an accurate measurement when using instruments operating with an electrostatic principle, as it is the case for the DMA and the CPMA.

The CPMA (Cambustion, Cambridge, UK) classifies particles according to their mass to-charge-ratio (Olfert & Collings, 2005; Olfert et al., 2007). Within the CPMA, the particles pass between two rotating concentric cylinders with an applied voltage. Only particles in a narrow mass-to-charge ratio range are transferred through the instrument. The particle concentration downstream of the CPMA was recorded by a CPC at a flow rate of 1.5 l/min using an external pump.

3.3.4 Measurement uncertainty

From our measurements we obtained standard deviations for the size- and thrust-selected measured mass of maximum 16.6 % for particles ≤40 nm and 11.0 % for particles >40 nm. An exception was the data point of lowest thrust level (3 %) and $d_m = 40$ nm that showed an exceptionally high standard deviation of 23.6 % and was therefore excluded from further analysis. Reasons could be the variations of thrust (3 ±1 %) when setting this test point and the possible changes in the size distribution (see Figure 3.2). The number of measurements performed for the same particle size and at the same thrust level varied from one to nine. If less than three mass scans were performed for a given size and thrust, the above mentioned maximum standard deviation was applied to these data points as well. The data between individual test days vary mainly due to different ambient conditions that affect the engine operation.

3.3.5 Effective density and mass-mobility exponent calculation

The effective density was calculated from the selected mobility size and the respective measured particle mass using the mass mobility relationship shown in Eq. (3.4). The mass was determined as the mode of a lognormal function fitted to the mass distributions recorded by the CPMA. The particle mass was averaged for the same particle size and engine test conditions. The averaged mass was then fitted for each test point using Eq. (3.3). This was done using units such that the values (mass and mobility size) were close to one in order to avoid reaching limitations of the fitting program. The fitting procedure was then repeated in SI units holding the beforehand derived ε constant. It was not possible to derive ε for thrust levels consisting of three or less different sizes measured because of the few number of data points available for fitting. The precision in terms of effective density of the DMA-CPMA-CPC system itself was determined to be ±9.4 % (Johnson et al., 2013).

3.4 Results and discussion

3.4.1 Mass-mobility relationship

Figure 3.2 shows exemplary size distributions measured on the 28th of August representative for the effective density measurements conducted after the Nafion dryer during A-PRIDE 5. The particle size distributions were lognormal for all test points. The geometric mean diameter (GMD) had a local maximum of ~20 nm at engine idle and then monotonically increased with thrust reaching 60 nm at maximum thrust. The particle number concentration followed the same trend showing a local maximum at idle, a minimum at 7 % thrust and then an increase with increasing thrust. The broadening of the size distribution and the increase in particle concentration therefore allowed to select a wider range of particle size at higher thrust levels. At thrust levels below 30 % the investigated size range spanned mobility sizes from approximately 30 nm to 75 nm in diameter whereas for higher thrusts the range spanned from 20 nm to 150 nm in diameter.
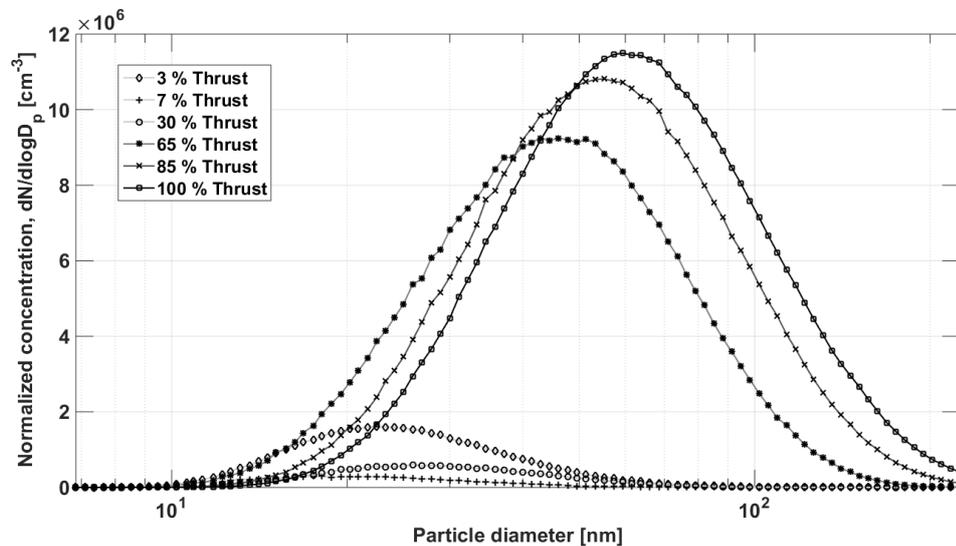
Figure 3.2   Typical PM distributions measured on the 28th of August using an SMPS system on the Annex 16 line after the Nafion dryer.

The mass-mobility relationship for the CFM56-7B26/3 engine at 3 %, 7 %, 22 %, 33 %, 67 %, 95 % and 105 % thrust is shown in Figure 3.3. The x- and y-axis show the selected mobility size and measured mass, respectively. The error bars represent the standard deviation derived from the modal mass measurements at constant DMA and thrust

conditions (see Section 3.3.4). The data points are grouped into boxes each showing the measured masses for a certain d_m at different thrust. They are depicted with a slight offset in x-direction such that the thrust in one box increases from left to right. The mass at a certain size is generally increasing with increasing thrust. This implies a more compact arrangement of the primary particles that is also supported by values of the mass mobility exponents discussed below or a larger primary particle size.

The measured particle mass ranged from 5.5×10^{-3} fg to 1.4 fg for particles with $d_m = 20$ nm and $d_m = 150$ nm, respectively. With increasing width of the size distribution the applied power law fit generally improves with respect to the 95 % confidence interval of the coefficients C and ε.
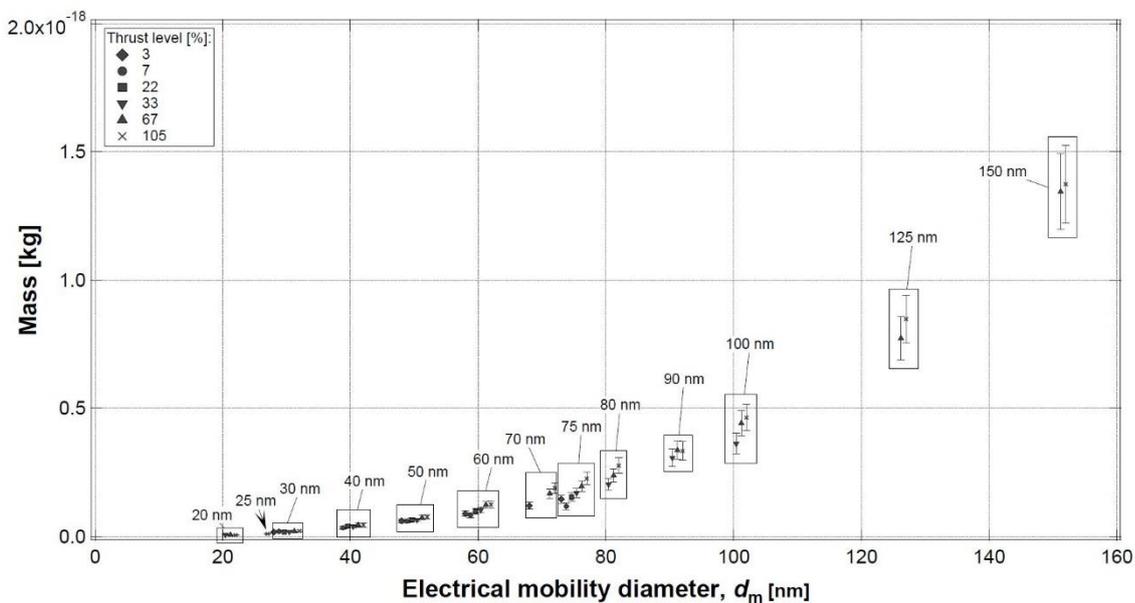
Figure 3.3   Electrical mobility diameter (d_m) vs. mass (m) from PM exhaust from a CFM56-7B26/3 engine. The data points are grouped into boxes each showing the measured masses for a certain d_m at different thrust. They are depicted with a slight offset in x-direction such that the thrust in one box increases from left to right.

Figure 3.4 summarizes the mass mobility exponents obtained for the dedicated runs (full circles) and for warm up (empty circles). The mass mobility exponent was found to be significantly lower at low thrust than at high thrust. At thrust levels below 30 % it ranged between 1.85 and 2.32 and at thrust levels between 67 % and 120 % it ranged from 2.57 to 2.79. At 105 % thrust, the measurements performed on particles smaller than 30 nm exceptionally showed a decrease in effective density (see Section 3.4.2) compared to the value measured at 30 nm and were therefore not taken into account for

the calculation of ε. This behavior was also observed by Johnson et al. (2015) and needs further investigation.

The general increase of the uncertainty in ε with decreasing thrust is assigned to the decrease in number of selected sizes and decreasing size range. The relative high value of ε (>2.50) for thrust higher than 60 % indicates that the particles have a more spherical shape and are less fractal than observed in other combustion sources. Olfert et al. (2007) determined mass mobility exponents from a diesel oxidation catalyst using a similar DMA-CPMA-CPC system. The values ranged from 2.22 to 2.48 at engine loads where the sulfate level was low enough to neglect condensation onto the particles. Park et al. (2003a) found values ranging from 2.33 to 2.41 at different loads for a diesel engine (John Deere 4045, 4 cylinders, 4.5 L, 75 kW). Table 3.2 summarizes this study's mass mobility exponents and mass mobility prefactors derived at the different engine loads and corresponding size ranges.
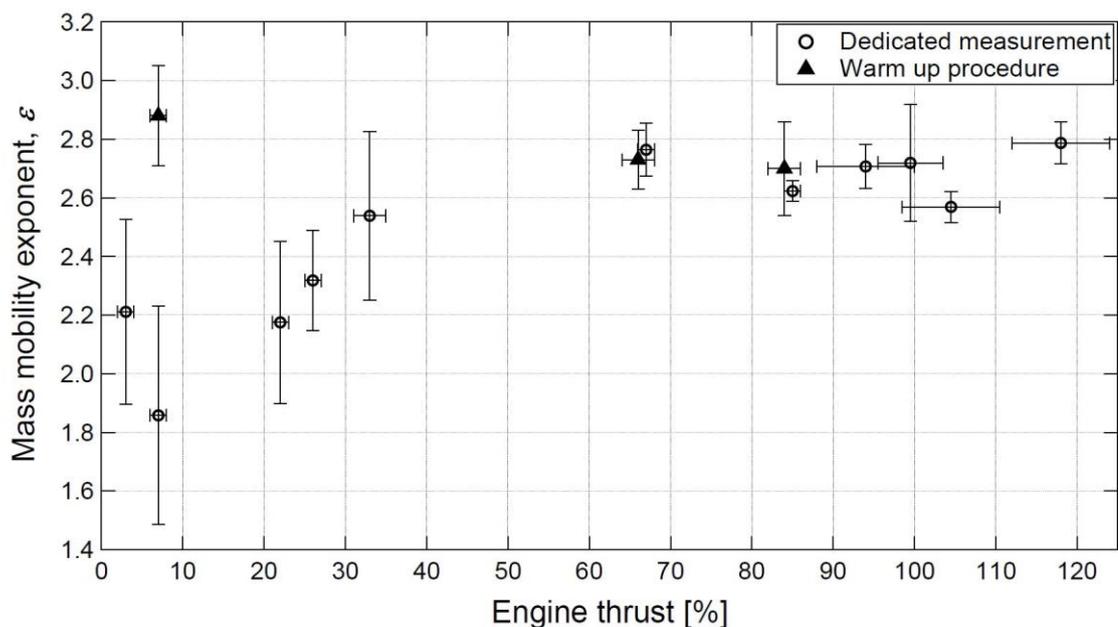
Figure 3.4   Mass mobility exponents (ε) at the different thrust levels derived during dedicated measurements (full circles) and warm up procedures (empty circles).

Due to the set-up of two parallel DMA-CPMA-CPC systems, it was possible to perform enough mass scans to derive the mass-mobility relationship at 7 %, 66 % and 85 % thrust during warm up. Except for 7 % thrust during warm up, the particles show very similar ε during the warm up as compared to the dedicated runs. This indicates similar particle morphology and comparable combustion process. The difference in ε at 7 %

thrust during warm up and ε at 7 % during the dedicated runs can be explained by the fact that the temperature inside of the engine influences the combustion process. This temperature was still near ambient conditions just after the cold start when the warm up procedure was initiated.

Table 3.2   Coefficients ε and C (see Eq. (3.3)), and the corresponding valid size range at different thrust levels.

Thrust level [%]	ε	C [kg/m$^\varepsilon$]	size range [nm]
3	2.21 ±0.32	810×10^{-6} ±41×10^{-6}	30–75
7	1.86 ±0.37	20.7×10^{-6} ±0.2×10^{-6}	30–75
22	2.18 ±0.28	400×10^{-6} ±30×10^{-6}	30–75
26	2.32 ±0.17	5.48×10^{-3} ±0.20×10^{-3}	30–75
33	2.54 ±0.29	220×10^{-3} ±10×10^{-3}	20–100
67	2.76 ±0.09	7.28 ±0.13	20–150
85	2.62 ±0.04	1.06 ±0.007	20–150
94	2.71 ±0.08	4.06 ±0.059	20–150
99.5	2.72 ±0.20	4.86 ±0.13	20–150
104.5	2.57 ±0.08	0.46 ±0.008	30–150
118	2.79 ±0.07	15.17 ±0.18	30–150
Warm up			
7	2.88 ±0.17	57.12 ±1.52	20–100
66	2.73 ±0.10	5.16 ±0.10	20–140
84	2.70 ±0.16	3.32 ±0.083	20–140

3.4.2 Effective densities

Figure 3.5 shows that the effective density decreases with increasing particle size. The decrease of effective density with mobility size was observed for all measured thrust levels. Hence, these particles can be considered to follow the concepts of fractal aggregates. For particles with $d_m = 30$ nm, the effective density ranged from 1075 kg/m^3 to 1490 kg/m^3, with the exception of the high value of 1865 ±291 kg/m^3 at 118 % thrust.

At $d_m = 75$ nm, measurements spanning the whole thrust range were conducted and ρ_{eff} ranged from 530 kg/m^3 to 1020 kg/m^3. With increasing thrust the effective densities generally increase for all selected sizes due to changes in the combustion process. Excluding 118 % thrust, this increase in effective density is smaller for smaller d_m. For particles larger than 100 nm only measurements at thrusts levels $\geq$67 % were possible and ρ_{eff} approaches ~800 kg/m^3 for $d_m = 150$ nm.

The mass distributions used to determine the mass of the size selected particles show a single mode for particles with a $d_m \geq 30$ nm. For particles <30 nm, the distributions are not always unimodal. In this case, it is assumed that the selected mobility size was close to the size of the primary particles and the number of primary particles was close to the limit of one single primary particle. For a diesel engine, the measured d_{pp} ranged from 24 nm to 28 nm with a standard deviation of ~25 % (Rissler et al., 2013), i.e. were observed with a similar value within the uncertainty range. Furthermore, the possible increase in aircraft engine primary particle size with increasing engine thrust is consistent with similar studies on combustion engine exhaust particles. Mathis et al. (2005) found values for d_{pp} of a heavy-duty diesel engine to vary between 17.5 nm and 32.5 nm depending on engine power and injection pressure with larger d_{pp} at high engine load.
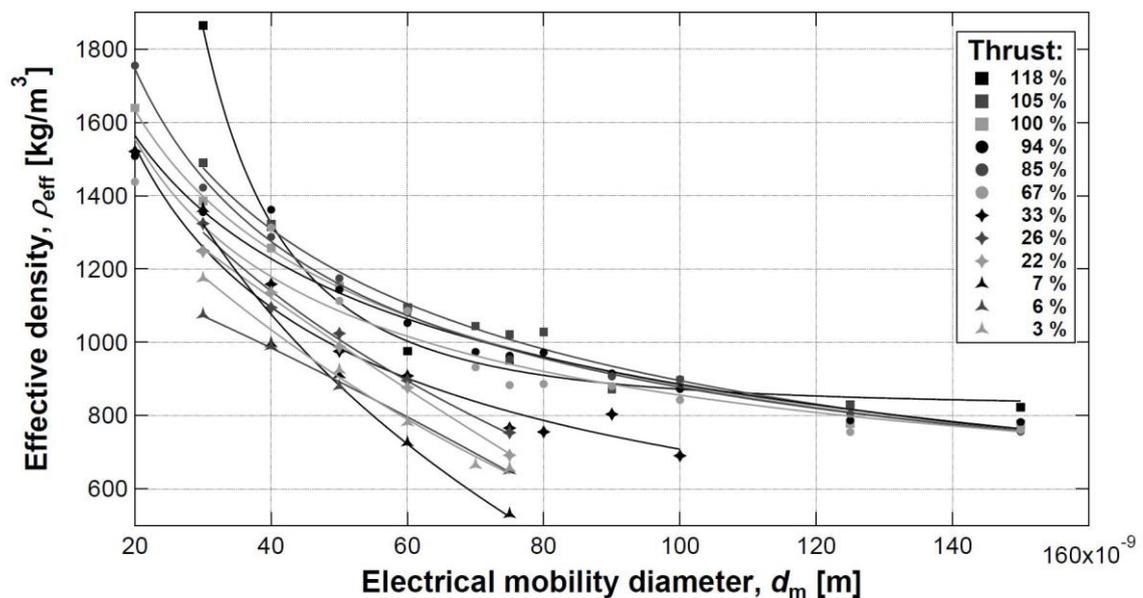

Figure 3.5   Effective densities of PM exhaust from a CFM56-7B26/3 engine for the measured sizes and applied thrust.

The effective density is equal to the material density if the number of primary particles reaches the limit of one. If at 118 % thrust the primary particle size was reached at $d_m = 30$ nm, the material density of the particles investigated in this study would correspond to 1865 ±291 kg/m^3. Within its uncertainty, this value is consistent with the density of 1700 ±70 kg/m^3 found by Park et al. (2004) for preheated (in order to avoid condensation of organics) diesel soot particles. In addition, a primary particle size of 30 nm is consistent with the measurements of Vander Wal et al. (2014), where primary particles larger than 25 nm were observed at 85 % thrust for a different aircraft engine, namely a CFM-56-3 aircraft engine. Despite the effort taken to avoid condensation of volatile and semi-volatile species by heating and drying the sample during A-PRIDE 5, an influence thereof on the measured effective density cannot completely be excluded because no corresponding measurements were performed.

Since the effective densities obtained at different thrust levels do not converge to one single mobility size, it is possible that the primary particle size changes with changing thrust. By extrapolating the fits towards smaller sizes, the above assumed material density would be reached at smaller sizes for lower thrusts. Thus, our data imply that the primary particle size decreases with decreasing thrust. Consistent with this hypothesis, Vander Wal et al. (2014) have also observed smaller primary particle sizes at lower thrust conditions for aircraft-turbine soot. Moreover, this hypothesis is confirmed by findings of Liati et al. (2014) who analyzed TEM pictures of aircraft engine exhaust particles sampled during the same A-PRIDE 5 campaign. The primary particle size was found to increase from 13 ±3 nm at low thrust (7 %) to 24 ±9 nm at high thrust (100 %) conditions using the same definition of thrust as presented in this study. The authors attributed the increase in size with increasing thrust to a decrease in air-to-fuel ratio and a shorter residence time of the combustion products within the combustor; both processes probably lead to a reduction of the soot oxidation rate and thus to larger primary particle sizes. Changes in the combustion temperature within the engine may also have played a role. It is worth noting that Dastanpour and Rogak (2014) have observed that soot aerosols tend to be external mixtures of soot aggregates, with smaller aggregates containing smaller primary particles and vice versa. In the present sample, such an effect would have to be secondary to thrust effects for the trends observed herein and by Liati et al. (2014) to be true.

We also calculated effective densities for particles <30 nm at thrust levels above 100 % but these effective densities did not follow the fractal nature observed for the larger

particles and the uncertainty range was exceptionally high and were therefore excluded from analysis.

3.4.3 Comparison of the single vs. multi-point probe

Figure 3.6 shows a comparison of the two probes. Depicted are the residuals of the measured masses predicted from the overall best fit to Eq. (3.3) and using all valid mass measurements. Residuals represent the error of a measured data point to the mathematically derived value using a fit function. The thrust range is colored in blue and red for the single point and the multi-point probe, respectively. To visually separate the measurements from the two probes, the data points from the single and multi-point probe have been arranged with a negative and positive offset from the actual value on the x-axis. Due to the lack of measurements of particles having the same size and thrust conditions when comparing both probes, only few overlapping data points exist. The residuals are within ±40 % for the majority of measurements. The residuals generally increase with decreasing thrust for a given d_m. Hence, residuals would be smaller if only data from one thrust level was fitted. That is, the thrust-dependent mass-mobility relationships discussed in Section 3.4.1 provide a more accurate mass prediction than this overall fit.

No systematic difference in terms of particle size and corresponding mass can be found between the single- and the multi-point probe. Consequently, data from both the probes were combined for the effective density analysis as presented above.
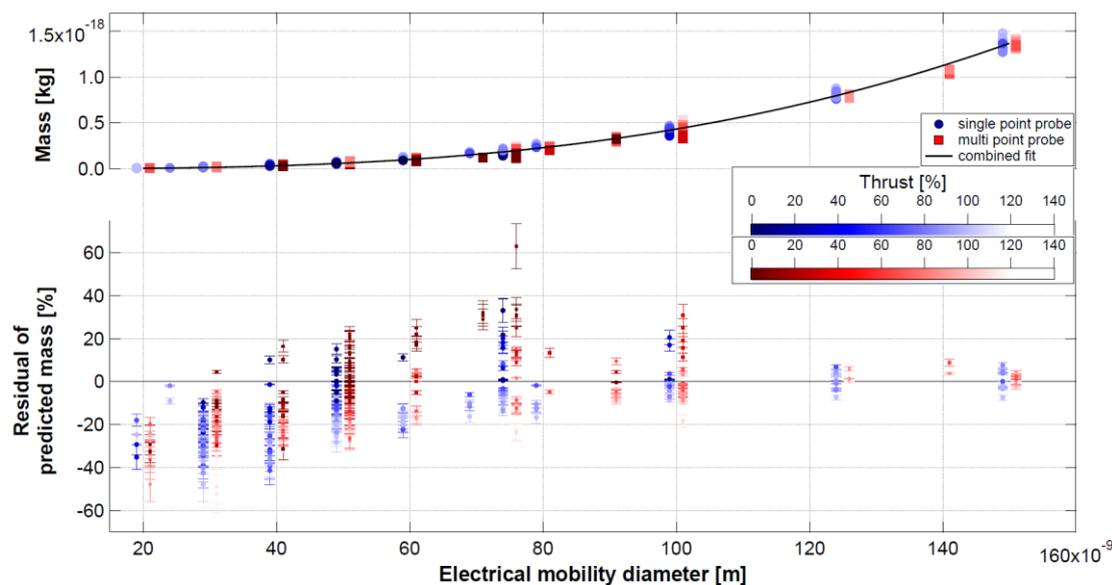
Figure 3.6   Comparison of the two sample probes. The x-axis shows the particle mobility diameter [m] with a positive and negative offset for the multi- (red) and single-point (blue) probe, respectively. The upper panel shows the measured masses [kg]. The lower panel shows the residuals from the measured masses to an overall best fit. The thrust [%] is depicted by the intensity of the color.

In a similar way, size selected particle masses measured from the Annex 16 line were compared with those measured from the PM line (cf. Figure 3.1). No significant or systematic differences were revealed. This indicates that the particles experienced negligible restructuring and/or condensation of secondary material in either of the sampling systems after emission. If this had been the case, significant differences would have been expected to arise due to the different temperatures in the two sampling lines. As a consequence of these results, the comparison of two engines as discussed in the next section includes all measurements, regardless of sampling probe or sampling line.

3.4.4 Comparison to the CFM56-5B4/2P engine

In addition to the measurements conducted on the CFM56-7B26/3 engine during A-PRIDE 5, we performed 22 DMA-CPMA-CPC scans for a CFM56-5B4/2P engine at three different thrust levels in the range of 21–40 % during A-PRIDE 4 in November 2012. Corresponding size distributions for the same CFM56-5B4/2P engine can be found in Lobo et al. (2015) that shows that the emitted particles are generally smaller. This engine has a unique dual annular combustor with two rings of fuel injection points designed for low NO_x emissions. The CFM56-7B26/3 has a commonly used single annular combustor. Both engines are turbofan engines and do not mix the air from the

engine core with bypass air before the exhaust duct. Johnson et al. (2015) performed effective density measurements on the same CFM56-5B4/2P engine at the same SR Technics facility during SAMPLE III.2 in April/May 2012 (EASA, 2012). The measurements were also conducted using a CPMA, sampling from both, the PM line and the undiluted Annex 16 line. In this section, we compare these two data sets for overlapping thrust levels. However, Johnson et al. used actual measured test cell thrust for which the corresponding combustor inlet temperature linked sea level thrust for Zurich can be up to 15 % higher depending on the different ambient conditions.

Figure 3.7 shows this study's measurements (triangles) for both engines in addition to the UoA (University of Alberta) data from Johnson et al. (2015) (circles). The data are grouped into three thrust categories: 21 ±1 %, 25 ±1 % and 35 ±5 % thrust (a, b and c). Figure 3.7a includes an additional UoA measurement performed at 17.4 % thrust (empty circles). UoA used a CPMA and a modified Differential Mobility Spectrometer (mDMS) system to derive effective densities (Johnson et al., 2015). The CPMA prese-lected particles with a certain mass-to-charge ratio. The mobility size distributions of the preselected particles were then obtained from the mDMS. Data was recorded from both lines with and without a Catalytic Stripper (CS). The CS was used to remove the gas-phase and semi-volatile fraction of the soot particles. In contrast to our findings, Johnson et al. observed a significant difference in the effective density measured from the diluted and the Annex 16 line. Therefore, we compare our data only to data recorded at the Annex 16 line without a CS.

Comparison of the two CFM56-5B4/2P engines (circles and dark blue triangles) reveals that the UoA data is generally higher but within the uncertainty range. The most striking difference is that except for the lowest thrust shown in Figure 3.7a, the measured UaA-effective densities show maxima for particle sizes between 30 nm and 40 nm whereas our data depict a steady increase towards smaller sizes. Possible reasons for these differences could be different experimental set-ups as outlined above, the different ambient measurement conditions, or differences in the engine/combustion process. The UoA data were recorded in April/May, whereas our measurements took place in the month of August (A-PRIDE 5) and November (A-PRIDE 4). The ambient temperature and pressure can influence the combustion process and thereby particle formation. As a consequence, the season when the experiment took place might have to be considered as well for the interpretation of the results. However, due to the lack of data from different seasons no conclusions are drawn regarding the effect of ambient T and RH on particle

effective densities. Additional reasons for the observed differences could be due to different measurement techniques and engine wear.

The comparison of the CFM56-7B26/3 to the CFM56-5B4/2P engine in Figure 3.7a and b indicates that the CFM56-5B4/2P engine yielded lower effective densities than the CFM56-7B26/3 engine for particles <40 nm. We assume that these differences are attributed to the different combustor systems described above that likely produce different primary particle sizes as well that could affect the measured effective density.

To infer similar information from the data presented in Figure 3.7c is less appropriate since herein, non-overlapping thrust levels of 40 % and 33 % are compared. The effective density however, was shown to increase with increasing thrust. Consequently, the effective density of particles from the CFM56-7B26/3 engine is likely to be higher if it would have been measured at the same 40 % thrust level rather than at 33 %. For particles with a mobility diameter ≥40 nm, the effective density of particles from both engines lies within the uncertainty range. The change in effective density with mobility size is smaller for the CFM56-5B4/2P engine for all thrust levels.

Johnson et al. (2015) calculated a mass-mobility exponent for the measurements at 17.4 % of 2.72 and 2.75 as shown in Figure 3.7a. At the closest thrust level of our measurements of 22 %, the mass-mobility exponent for particles from the CFM56-7B26/3 engine was only 2.18 ±0.28. This indicates that the particles from the CFM56-5B4/2P engine were more spherical in the range of these low thrust levels. In our measurements, similar values of ε (~2.74) were only observed at thrust >60 % (see Figure 3.4) for the CFM56-7B26/3 engine.

a)
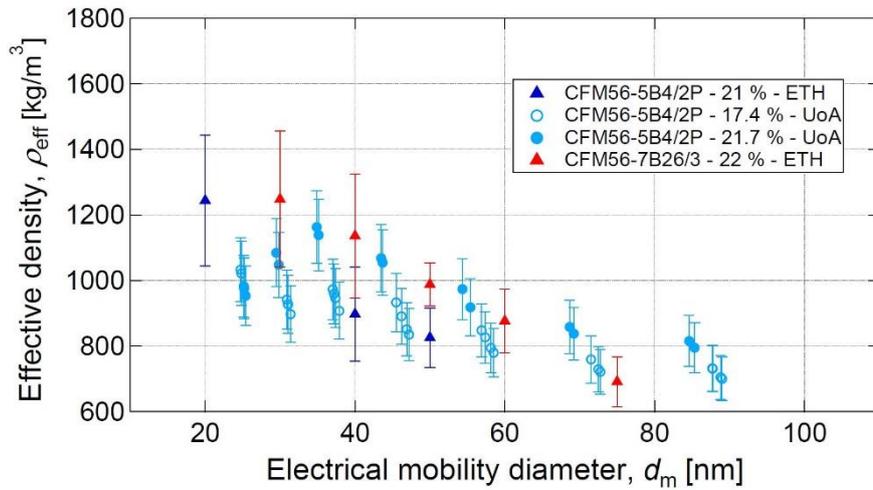
b)
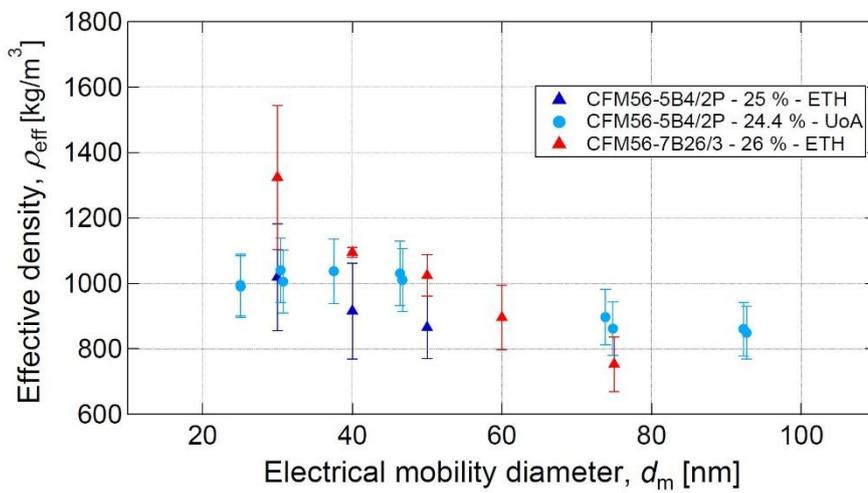
c)
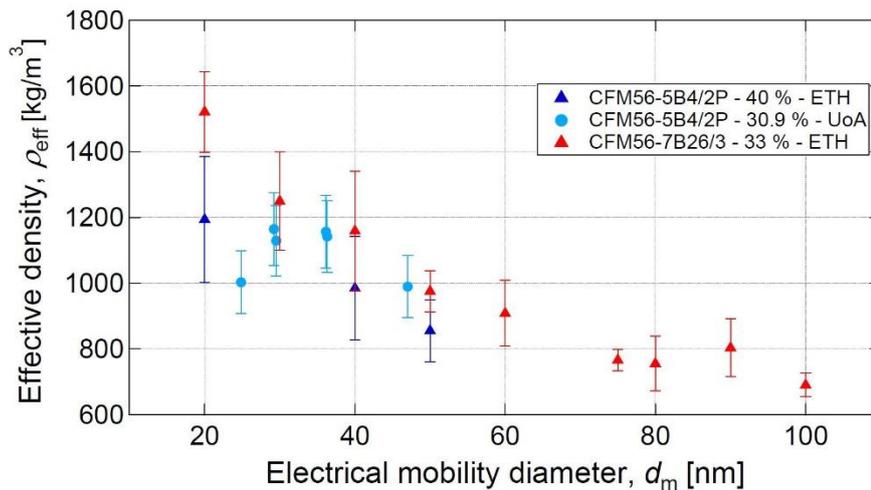
Figure 3.7   Comparison of effective densities derived by our measurements (triangles) from a CFM56-7B26/3 (red) and a CFM56-5B4/2P (dark blue) engine to literature values measured by Johnson et al. (2015) (circles) from a CFM56-5B4/2P engine at similar thrust levels.

3.5 Summary

To measure the effective density of non-volatile particles emitted by a CFM56-7B26/3 aircraft engine, a DMA-CPMA-CPC system was used in the framework of the A-PRIDE 5 campaign. The measurements were performed for 12 different thrust levels and spanned the mobility size range from 20 nm to 150 nm depending on the corresponding size distribution and instrument restrictions. Mobility-based effective densities decreased with increasing mobility size. The effective density increased with increasing engine thrust due to changes within the combustion process. It ranged from 1075 kg/m^3 to 1865 kg/m^3 for $d_m = 30$ nm including all thrust levels. The mass-mobility exponents ranged from 1.85 to 2.32 for thrust levels <30 % and from 2.54 to 2.79 for thrust levels >30 %. For particles larger than 100 nm, only measurements at thrusts levels ≥67 % were possible because of size distribution and instrument limitations. ρ_{eff} approached ∼800 kg/m^3 for $d_m = 150$ nm.

A comparison of two engines revealed that for particles with $d_m > 40$ nm the effective densities from the CFM56-7B26/3 and the CFM56-5B4/2P are within the uncertainty range. For smaller particles the CFM56-5B4/2P engine showed lower effective densities than the CFM56-7B26/3 engine. The values for the mass-mobility exponents at thrust levels higher than 60 % (2.54 to 2.79) from a CFM56-7B26/3 were similar to literature values of ∼2.74 measured from a CFM56-5B4/2P at 10 % thrust. A new sampling probe introduced during A-PRIDE 5 did not show a systematic difference between the two sampling probes with regard to our density measurement.

Information on the physical properties of engine emission particles in general can be used in emission protocols. For instance, if only information about the particle size distribution is available the effective densities shown can be used to estimate the total emitted mass. Since the particle's initial size, mass and information on morphology is provided, these properties can also be compared to those of aged particles. Aged particles can be collected from ambient in the vicinity of airports or artificially be aged in the laboratory by coating the particle and/or treat them with UV-light. The results can also be of interest for investigations addressing the combustion process with respect to the engine PM emissions.

From an atmospheric science perspective the presented values as well as a possibly improved knowledge of the aging in terms of conversion speed and rate could be applied in climate models. The values found in this study could be used as a starting

point to investigate atmospheric aging of turbine emission particles from the source. The aging then influences the particle scattering and absorption properties which are important for the Earth's radiation budget.

Acknowledgments

4 DETERMINATION OF PM MASS EMISSIONS FROM AN AIRCRAFT TURBINE ENGINE USING PARTICLE EFFECTIVE DENSITY

L. Durdina[a,b], B.T. Brem[a,b], M. Abegglen[c], P. Lobo[d], T. Rindlisbacher[e], K.A. Thomson[f], G.J. Smallwood[f], D.E. Hagen[d], B. Sierau[c], J. Wang[a,b]

[a] Laboratory for Analytical Chemistry, Empa, Dübendorf CH-8600, Switzerland
[b] Institute of Environmental Engineering (IfU), ETH Zürich, Zürich CH-8093, Switzerland
[c] Institute for Atmospheric and Climate Science (IAC), ETH Zürich, Zürich CH-8092, Switzerland
[d] Center of Excellence for Aerospace Particulate Emissions Reduction Research, Missouri S&T, Rolla, MO 65409, USA
[e] Swiss Federal Office of Civil Aviation (FOCA), Bern CH-5003, Switzerland
[f] Measurement Science and Standards, National Research Council (NRC), Ottawa K1A 0R6, Canada

This chapter is adapted from the original article.

Abstract

Inventories of particulate matter (PM) emissions from civil aviation and air quality models need to be validated using up-to-date measurement data corrected for sampling artifacts. We compared the measured black carbon (BC) mass and the total PM mass determined from particle size distributions (PSD) and effective density for a commercial turbofan engine CFM56-7B26/3. The effective density was then used to calculate the PM mass losses in the sampling system. The effective density was determined using a differential mobility analyzer and a centrifugal particle mass analyzer, and increased from engine idle to take-off by up to 60 %. The determined mass-mobility exponents ranged from 2.37 to 2.64. The mean effective density determined by weighting the effective density distributions by PM volume was within 10 % of the unit density (1000 kg/m^3) that is widely assumed in aircraft PM studies. We found ratios close to unity between the PM mass determined by the integrated PSD method and the real-time BC mass measurements. The integrated PSD method achieved higher precision at ultra-low PM concentrations at which current mass instruments reach their detection limit. The line loss model predicted ∼60 % PM mass loss at engine idle, decreasing to ∼27 % at high thrust. Replacing the effective density distributions with unit density lead to comparable estimates that were within 20 % and 5 % at engine idle and high thrust, respectively. These results could be used for the development of a robust method for sampling loss correction of the future PM emissions database from commercial aircraft engines.

4.1 Introduction

The lack of data on emissions of particulate matter (PM) from aircraft turbine engines has led to simplifying assumptions in development of PM emissions inventories (Masiol & Harrison, 2014). This gap has been addressed in several recent field campaigns (Herndon et al., 2008; Kinsey et al., 2010; Timko et al., 2010a; Mazaheri et al., 2011; Lobo et al., 2012; Mazaheri et al., 2013). However, these campaigns produced only partial inventories of PM characteristics (mass, number, size, composition) for some operating conditions and engines of the in-use aircraft at the particular airport. The ground level emissions from aircraft increase the background PM concentrations near airports (Westerdahl et al., 2008; Hsu et al., 2012) and pose a serious health risk (Barrett et al., 2013; Yim et al., 2013). Aircraft PM emissions also globally impact the climate. The global black carbon (BC) mass emissions from commercial aviation have been

estimated to warm the atmosphere as much as 1/3 of the CO_2 emissions from aviation (Stettler et al., 2013). However, the global emissions inventories are based on limited data sets and estimates. The data sets used are often not corrected for sampling artifacts that are common with extractive sampling, and misrepresent the actual emissions. More measurement data of the direct aircraft PM emissions with resolved sampling artifacts are needed to validate current models.

Directly behind the engine in the high temperature exhaust, aerosol consists almost entirely of non-volatile (solid) soot particles. The primary spherical soot particles coagulate and form larger fractal-like aggregates. The largest fraction of the soot mass is made up of BC that closely corresponds to non-volatile elemental carbon (EC) (Petzold et al., 2011). Despite the fractal nature of aircraft soot particles, researchers often assume that the particles are spheres with a constant density to convert the measured particle size distributions (PSD) to PM mass. Most widely assumed is unit density $1000 \, kg/m^3$ (Onasch et al., 2009; Lobo et al., 2011; Mazaheri et al., 2011; Petzold et al., 2011; Kinsey et al., 2012; Peck et al., 2012), but also higher values have been reported: $1200 \, kg/m^3$ (Beyersdorf et al., 2013), $1500 \, kg/m^3$ (Schmid et al., 2004; Brundish et al., 2007), $1900 \, kg/m^3$ (Hagen et al., 1998), and $2000 \, kg/m^3$ (Howard et al., 1996). In some cases, the PSD-derived mass overestimated the BC mass measured by optical techniques by as much as 50 % (Onasch et al., 2009; Kinsey et al., 2012), others have reported an average underestimation of BC mass by 35 % (Petzold et al., 2011). These differences could be caused by a systematic departure from the uniform density and particle sphericity (Kinsey et al., 2012).

Particle density and shape of irregular particles are often lumped in one parameter, the particle effective density (Park et al., 2003a; DeCarlo et al., 2004; Schmid et al., 2004). The mass of individual particles classified by a differential mobility analyzer (DMA) can be measured directly using the aerosol particle mass analyzer (APM), centrifugal particle mass analyzer (CPMA) (Olfert et al., 2007), or indirectly from aerodynamic size measurements using an aerosol mass spectrometer (AMS) or an electrical low pressure impactor (ELPI). Results of these measurements are expressed as the ratio of particulate mass to volume from the mobility diameter, which is the effective density. The effective density of soot agglomerates decreases with increasing particle size to values substantially below the material density (bulk soot density $\sim 1800 \, kg/m^3$ (Park et al., 2003a)). Here, we use the mass-mobility-based effective density in the form of a power-law relationship:

$$\rho_{\text{eff}} = C_\rho d_{\text{m}}^{D_{\text{fm}}-3} \tag{4.1}$$

where d_{m} is the particle mobility diameter, D_{fm} is the mass-mobility exponent (fractal-like dimension) with a theoretical range from 1 for long chains to 3 for spheres, and C_ρ is a scaling constant. D_{fm} of soot particles from diesel engines and diffusion flame burners range from 1.9 to 2.6 (Park et al., 2003a; Olfert et al., 2007; Kim et al., 2009; Rissler et al., 2013), D_{fm} of 2.72 has been recently determined for an aircraft turbine engine (Johnson et al., 2015). The effective density and D_{fm} vary for different combustion sources and variability is also expected for different aircraft engine combustion technologies.

The size-resolved particle effective density has been previously applied to determine PM mass from PSD for diesel engines emitting ultra-low levels of PM (Liu et al., 2009; Li et al., 2014; Zheng et al., 2014). This integrated PSD method (IPSD) (Liu et al., 2009) is a promising addition to the regulatory gravimetric method as diesel PM emissions continue to decrease and reach the measurability limits. It can be adapted for gas turbine PM measurements where similar challenges emerge at ultra-low PM mass emissions from modern engines.

BC mass concentrations in aircraft gas turbine exhaust have been recently investigated by real-time optical measurement techniques (Petzold et al., 2011; Crayford et al., 2012). Real-time measurement of non-volatile PM mass will be also part of the developed standardized measurement methodology of PM emissions from aircraft turbine engines (SAE, 2013). Although the current mass-based techniques can reliably detect concentrations $\sim$10 μg/m^3, the advanced gas turbines emit BC mass $\sim$1 μg/m^3 at some conditions of the standard emissions test cycle (Crayford et al., 2012). Therefore, the sensitive IPSD technique could provide additional information along the regulatory measurements.

An unavoidable artifact of gas turbine sampling is the particle loss. Diffusional, inertial and thermophoretic effects are responsible for particle losses to the walls of the transfer lines that are more than 30 m long (SAE, 2013). Some studies report line loss corrected PM mass emissions using experimentally determined penetration functions and unit particle density (Lobo et al., 2011), whereas others report PM emissions using uncorrected instrument readings (Timko et al., 2010a). The PM mass and number emissions data measured with the standardized systems from in-production engines will be published in the ICAO emissions database (ICAO, 2014) and used by climate and air

quality modelers. Therefore, the particle losses in the standardized systems need to be well characterized since they could reach several tens of percent in terms of particle mass (and much higher in terms of number) — depending on the PSD and sampling system properties (Timko et al., 2010a). In this regard, size-resolved effective density distributions could improve the estimation of PM mass losses in the sampling system.

To study the variability and characteristics of non-volatile PM emissions from in-production aircraft turbine engines, standardized test systems compliant with the methodology developed by the SAE E-31 Aircraft Exhaust Emissions Measurement Committee (SAE, 2013) have been operated in the engine testing facility of SR Technics, Zürich airport, Switzerland in several campaigns. This paper analyses the measured data from the A-PRIDE 5 campaign (*Aircraft – Particulate Regulatory Instrumentation Demonstration Experiment*) that took place in July–August 2013. During this campaign, we determined effective density distributions from tandem mass-mobility measurements over the entire operating range of a CFM56-7B26/3 engine (Boeing 737 next generation). The effective density distributions were then utilized in the IPSD method to calculate total PM mass concentrations (TPM). TPM was then compared with the results from the real-time optical BC mass measurement techniques. Finally, we used effective density distributions to estimate the PM mass losses in the sampling system.

4.2 Methods

4.2.1 Engine tests

The engine was operated on a descending power curve over its entire operating range burning conventional Jet A-1 fuel. The engine test matrix was guided by the landing/takeoff cycle for emissions testing defined by the International Civil Aviation Organization (ICAO, 2008). This test cycle consists of four engine thrust levels at reference conditions (1 atm and 15 °C): 7 % (taxi), 30 % (approach), 85 % (climbout) and 100 % (takeoff). The test points were set using the combustor inlet temperature T_3. As the ambient temperature varied during the campaign, different thrust levels were reached at the same T_3. To capture the emissions at the highest power, a test point at the maximum continuous operation limit was introduced (T_3 corresponding to around 110 % rated thrust F_{00} at reference conditions). The relative corrected thrust $F_{c,rel}$ used here is the measured thrust corrected to reference conditions.

4.2.2 Exhaust sampling

The engine exhaust was sampled at the engine exit plane by two different probes: a single-orifice probe, and a fixed multi-orifice cruciform rake that is compliant with the current regulations for emissions certification (ICAO Annex 16 Vol. II; (ICAO, 2008)). Both the probes were made of Inconel alloy to withstand the high temperatures at the engine exit. Positions of the probes' orifices in the exhaust stream were adjusted such that air-to-fuel ratios (AFR) calculated from the gaseous emissions data agreed within 15 % of the AFR from the engine data, and thus they provided a representative exhaust sample.

Trace-heated lines transferred the sample from the probe to the distant instrumentation for gas and particle measurements. After a 6.3 m long stainless steel transfer section, the line was split to provide sample to the three reference systems — Swiss, North American, and European. The two guest systems (Figure 4.1) were the North American mobile reference system operated by Missouri University of Science & Technology and the European mobile reference system operated by Sample III Consortium (Crayford et al., 2012). The sample to each system was then again split in three paths: undiluted sample line (Annex 16 line), diluted sample line (PM line), and an excess sample path. Both the sample lines were made of carbon-loaded, electrically grounded PTFE to minimize electrostatic particle losses. The undiluted Annex 16 line for the Swiss reference system transferred the raw exhaust to a gas bench measuring CO_2, NO_x, CO (Horiba PG250), and unburned hydrocarbons (Horiba MEXA-1170HFID). The PM line sample was diluted by Dekati DI-1000 ejector diluter by a factor of $\sim$8–12 using high purity synthetic air. Transport times from the probe to the instruments were on the order of 3−5 s.
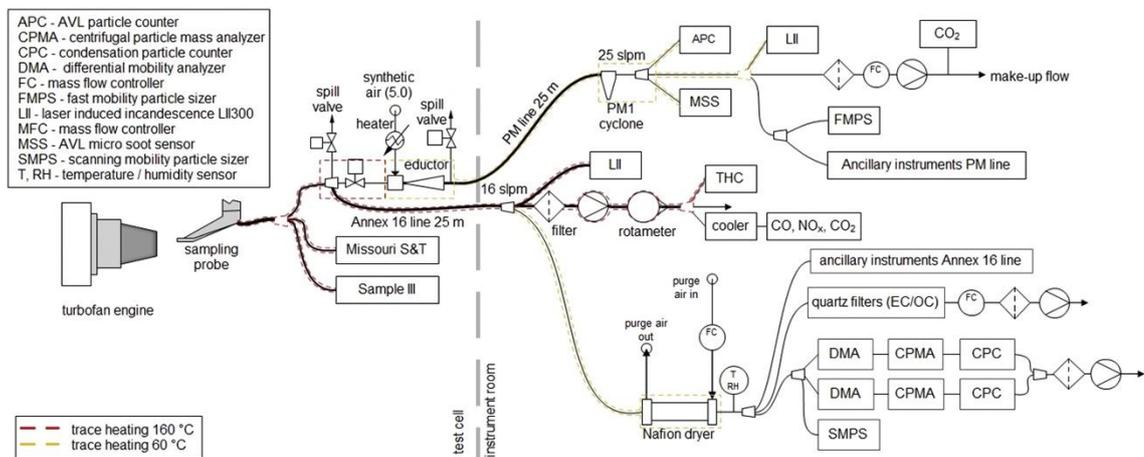

Figure 4.1   Schematic of the A-PRIDE 5 experimental setup.

4.2.3 PM instrumentation

To characterize non-volatile PM (nvPM), we measured PM number, mass, and size (Figure 4.1). The nvPM number concentration was measured using an AVL Particle Counter advanced with a catalytic stripper and a sulfur trap (APC; AVL model 489). The nvPM mass concentration was measured using two optical absorption instruments. The Micro Soot Sensor (MSS; AVL model 483 (Schindler et al., 2004)) measures the equivalent black carbon mass concentration (eBC, (Lack et al., 2014)) based on the photo-acoustic principle. The second instrument, the LII300 (LII; Artium Technologies) is based on the laser-induced incandescence (Snelling et al., 2005) and reports the refractory black carbon mass concentration (rBC (Lack et al., 2014)). Both the BC mass sensing instruments were calibrated in parallel to the thermo-optically determined EC mass concentrations (Method 5040 (NIOSH, 2003)) using an inverted flame burner. All three systems had the same models of nvPM mass and number instruments. PSD in the Swiss system was measured using a Scanning Mobility Particle Sizer (SMPS; TSI 3096) and a Fast Mobility Particle Sizer (FMPS; TSI 3091) in the Annex 16 line and the PM line, respectively (Figure 4.1). PSD in the PM lines of the guest systems was measured by Differential Mobility Spectrometer DMS500 (DMS500; Cambustion).

To determine the size-resolved particle effective density, we used two DMAs (DMA; TSI 3081), CPMAs (Cambustion, Ltd.), and condensation particle counters (CPC; TSI 3776) in series. With the two systems in parallel we collected more data in a wider particle size range. After the first two days, the DMA-CPMA-CPC systems were moved to the Annex 16 line due to the ultra-low particle concentration in the PM line at thrust levels below 50 % (1–5 µg/m^3).

For the undiluted line measurements, there is a potential for water and volatiles condensation that would restructure the particles and change the effective density compared to the diluted line (Johnson et al., 2015). To avoid this, measurements were done downstream of a multi-tube Nafion dryer (Permapure PD-100T-24-MSS) that maintained the relative humidity of the sample <25 %. The results for the two lines agreed within the uncertainty of the method and test-to-test variability, thus we assumed that the particle morphology remained the same in both the lines (see Supplementary information S2).

4.2.4 Effective density distributions

To determine effective density distributions, the monodisperse aerosol after the DMA was classified by mass/charge ratio in the CPMA while stepping the classifier speed and voltage. The mass spectral density from the CPMA scan was fitted with a log-normal distribution using Origin 9.1 where the mode was identified as the particle mass of the singly-charged DMA-classified particles. On average, the standard deviation of the fit was 0.7 %, and results with standard deviation higher than 5 % were excluded from the analysis. In the next step, effective densities were calculated from the paired mobility size - mass data as $6m_p/\pi d_m^3$, where m_p is the determined particle mass. They were then grouped to three thrust ranges with the average standard deviation of the mean <10 % for a given particle size: 3–5 % (90 valid data points), 15–30 % (40 valid data points), and 50–100 % $F_{c,rel}$ (320 valid data points). The average effective densities for each particle size and thrust range were fitted with Eq. (4.1) using a χ^2-minimization algorithm weighted by the standard deviation of the mean in Origin 9.1. The three effective density distributions were used in the next steps for calculation of the mean effective density and TPM.

4.2.5 Mean effective density

The mean effective density simplifies the IPSD technique by using a single factor or a function based on the experimentally determined effective density. It was determined from the DMS500 and SMPS data as follows:

$$\rho_m = \frac{\sum_{i=1}^{n} n_i \frac{\pi D_{p,i}^3}{6} \rho_{eff}(D_{p,i})}{\sum_{i=1}^{n} n_i \frac{\pi D_{p,i}^3}{6}} \tag{4.2}$$

where $D_{p,i}$ is the i-th channel diameter midpoint and n_i is the particle number concentration in the i-th channel in the discrete PSD data at standard temperature and pressure (273.15 K and 101.325 kPa). In this equation, the numerator represents the TPM and the denominator is the total PM volume. Two assumptions were made for this calculation. First, the effective density of particles smaller than 20 nm was forced to the effective density at 20 nm. This assumption decreased the TPM by ~0.1 % and ~5 % at high thrust (50–100 %) and low thrust (3–30 %), respectively. Second, only the dominant peaks in the DMS500 PSD data were used for the analysis. The secondary peaks at ~200–500 nm had measurable mass, but were low in number concentration that could not be resolved by the DMS500 and were likely measurement artifacts (Williams et al.,

2012). Due to the extremely low mass concentrations at low thrust levels, these secondary peaks would decrease the mean effective density by up to 50 %.

4.2.6 Emission index of PM mass

The averaged PM mass concentrations are reported here as mass-based emission indices (EI_m) expressed as mass of PM per unit mass of fuel burned (SAE, 2013; Masiol & Harrison, 2014). At a stable engine test point (standard deviation of the particle number concentration measured by the APC < 5 %), the real-time BC mass and PSD data were averaged for 30 s whereas the SMPS scans were averaged for the whole stable period.

4.2.7 Correction for sampling losses

The line loss correction model outlined in Figure 4.2 uses a modeled particle penetration function combined with thrust-dependent PSD parameters and effective density distributions. Size-dependent particle transport efficiency was estimated using a model developed for characterization of particle losses in aircraft exhaust sample lines by the United Technologies Research Center (UTRC (Liscinsky et al., 2010). The UTRC model agrees well with experimental studies (Liscinsky et al., 2010; Anderson, 2011; Crayford et al., 2012). We assume that the aerosol at the mass instrument is log-normally distributed with the geometric mean diameter (GMD) and the geometric standard deviation (GSD) being linear functions of engine thrust. Both the GMD and GSD were determined from log-normal fits of the DMS500 data and the coefficients of determination of the linear regressions R^2 were >0.93. Firstly, the program iterates the initial particle number concentration $N_{tot,0}$ such that the mass concentration of the modeled distribution equals the measured BC mass. Secondly, the modeled particle mass distribution is multiplied by the inverted penetration function from the UTRC model. Finally, the ratio between the two mass concentrations is the sought line loss correction factor. Details and equations used in the model can be found in the online Supplementary information, S1.
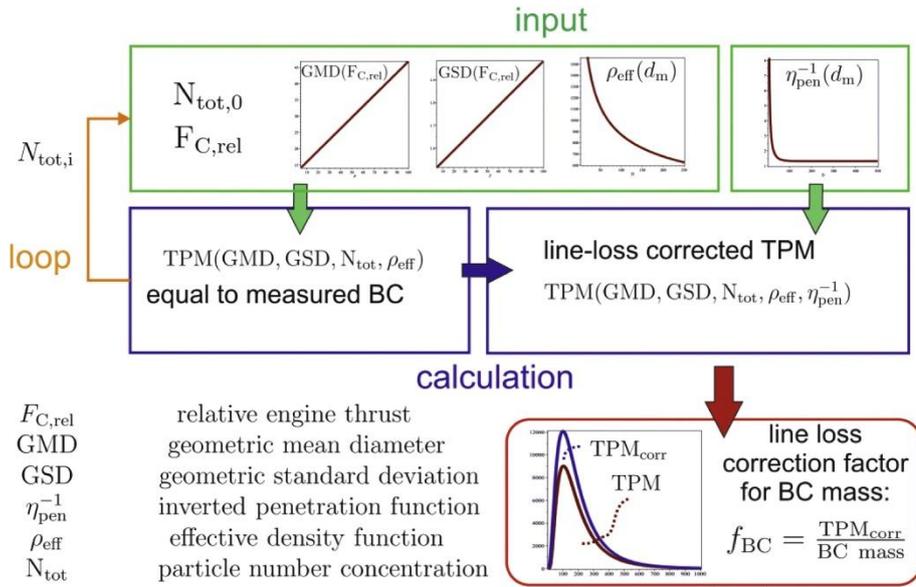
Figure 4.2 Flowchart of the line loss correction method.

4.3 Results and discussion

4.3.1 Effective density distributions

Both the effective density and mass-mobility exponents increased with engine thrust. In Figure 4.3, the curve for the lowest thrust range falls rapidly with particle size. The high thrust curve decreases more gradually and levels off at ~125 nm. The following equations were determined for the three thrust ranges (±standard error of fit at 95 % confidence):

$$\rho_{\text{eff},3-5\,\%} \left[\frac{\text{kg}}{\text{m}^3} \right] = 0.02 d_{\text{m}}^{2.37-3} \pm 77 \tag{4.3}$$

$$\rho_{\text{eff},15-30\,\%} \left[\frac{\text{kg}}{\text{m}^3} \right] = 0.2 d_{\text{m}}^{2.50-3} \pm 57 \tag{4.4}$$

$$\rho_{\text{eff},50-100\,\%} \left[\frac{\text{kg}}{\text{m}^3} \right] = 2.44 d_{\text{m}}^{2.635-3} \pm 14 \tag{4.5}$$

To justify the use of a single equation for the 50–100 % range, a surface function was fitted to the effective density data and can be found in the Supplementary information, S2.
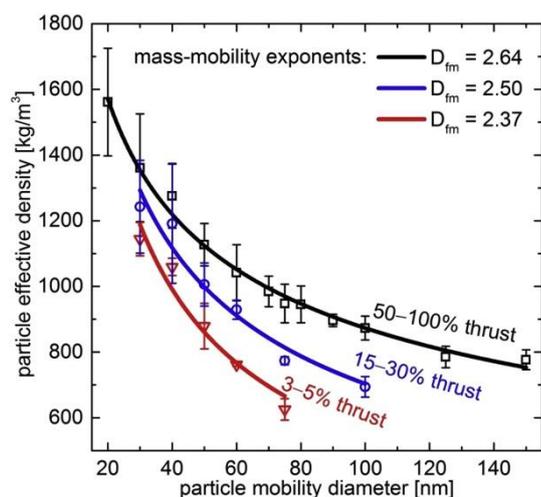
Figure 4.3   Effective density distributions determined for the various thrust ranges. Error bars represent standard deviation in the experimental data.

While the results are in the range of the previously determined size-resolved effective density for aircraft turbines (Williams et al., 2012; Johnson et al., 2015), there are no reports on changing effective density with engine thrust (here up to 60 % at 75 nm). Two hypotheses could account for this: increase of primary particle size and change of chemical composition. At low thrust, the AFR is the highest and also the residence time in the combustor is the longest, thus more time is available for soot oxidation and consumption. With increasing thrust, AFR decreases and residence time shortens, therefore the primary particle size as well as the total soot mass emissions increase. Electron microscopic analysis of soot particles collected during A-PRIDE 5 confirms the increase of primary particle size with thrust (Liati et al., 2014; Vander Wal et al., 2014) also observed increasing primary particle size and change of the internal structure with engine thrust using high resolution transmission electron microscopy for a CFM56-3 engine. They link the change of particle structure from amorphous to graphitic with the changing chemical composition from organic carbon (OC) at low thrust to EC at high thrust ((Vander Wal et al., 2014) and references herein).

4.3.2 Mean effective density

The mean effective densities determined from the DMS500 and SMPS data linearly decreased from ~1100 kg/m^3 at ground idle to ~900 kg/m^3 at takeoff (Figure 4.4b and c). With increasing thrust, GMD shifts to bigger particles that have lower effective density, hence the mean effective density decreases. We approximated the mean effec-

tive density as (±standard error of fit) 983 ±7.7 kg/m^3 and 932 ±17.4 kg/m^3 from the DMS500 and SMPS data, respectively.
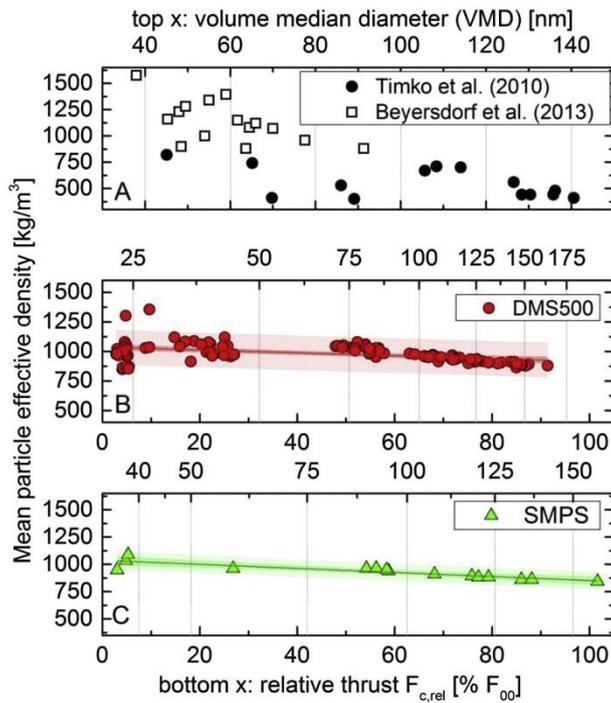
Figure 4.4   Mean effective density as a function of engine thrust and volume median diameter (VMD). a) PW308 engine (circles) and a CFM56-2C1 engine (open squares). b) DMS500 (this study) and c) SMPS (this study). Note that the lower two panels have the same thrust scale, but the VMD determined for the two techniques as a function of engine thrust shown in the upper x-axes is different.

The mean effective density was previously determined as a ratio of BC mass to total PM volume for engines burning various blends of conventional and alternative fuels (Timko et al., 2010b; Beyersdorf et al., 2013). Our results are more than 50 % higher than those for a PW308 business jet turbofan (circles in Figure 4.4a; (Timko et al., 2010a)), whereas the mean effective density for a CFM56-2C1, a high-bypass turbofan engine, is on average by 25 % higher (squares in Figure 4.4a; (Beyersdorf et al., 2013)). Certainly, the differences in the techniques used account for some of the differences observed; nevertheless it is evident that a single mean effective density misrepresents the whole fleet due to the different combustion technologies and fuels used. For the engine tested here, however, the widely assumed unit density is reasonable, being within 10 % of the experimentally determined values in the entire operating range. Its practical value is used later in the line loss correction.

4.3.3 Comparison of mass concentrations

Figure 4.5 shows the TPM and online BC mass data. The data are referenced to MSS, which was the primary mass instrument for the Swiss reference system (Table 4.1, inset of Figure 4.5). The rBC mass has a negative offset and a slope close to unity. The origin of this offset is yet unknown, but could be due to sensitivity to particle morphology and composition. Common to both instruments is the measurement noise when measuring emissions at very low thrust levels.
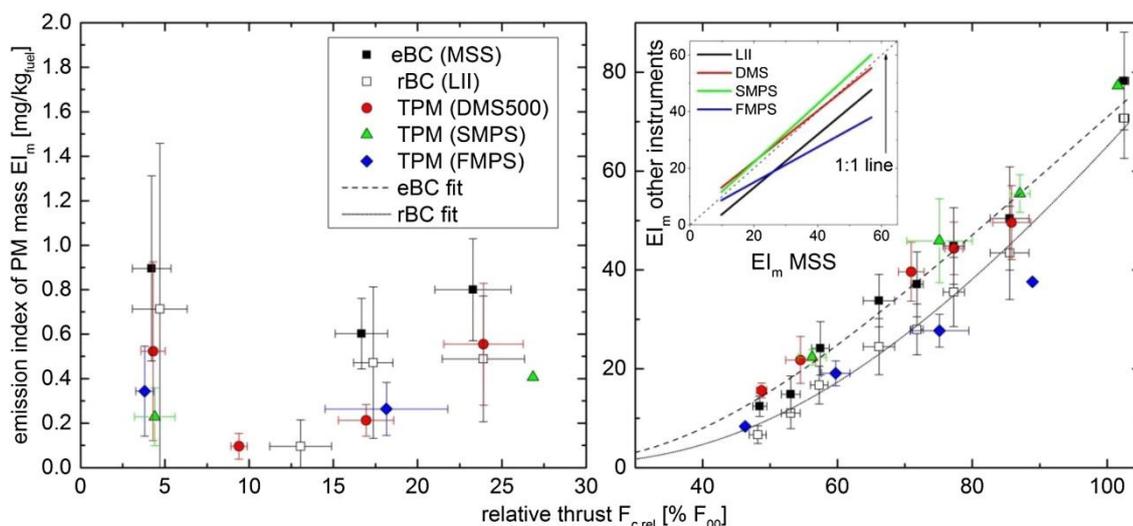
Figure 4.5   Comparison of TPM and BC mass. Error bars represent one standard deviation of the averaged data.

The TPM derived from DMS500 and SMPS agreed well with eBC mass (Table 4.1). At low thrust where both the rBC and eBC data were scattered and sometimes went negative, both the TPM techniques could still detect mass as low as 0.15 μg/m^3 and were more consistent. Our SMPS – eBC mass closure qualitatively agrees with the diesel PM studies, which report ratios between the SMPS IPSD method and the gravimetric method close to unity (Park et al., 2003b; Liu et al., 2012).

Table 4.1   *Comparison of the PM mass data to eBC mass in the 50–100 % thrust range.*

Instrument	Average ratio ±st. dev.	Slope	Offset [mg/kg]
LII	0.72 ±0.12	0.94	−5.7
DMS500	1.06 ±0.09	0.90	4.3
SMPS	1.08 ±0.03	1.03	1.45
FMPS	0.72 ±0.05	0.62	2.43

The FMPS underestimated the eBC by more than 30 % at high thrust (Table 4.1, Figure 4.6). Both the FMPS and its 10 Hz version, the engine exhaust particle sizer (EEPS), undersize agglomerate particles by up to 40 % compared to SMPS (Anderson, 2011; Lee et al., 2013) which underestimates the PM mass. The result is similar to (Li et al., 2014) that report a ratio of 0.63 between the EEPS IPSD mass and gravimetric mass determined for a light duty diesel vehicle. To improve its performance, FMPS should be calibrated for soot like the DMS500 (Symonds, 2010).
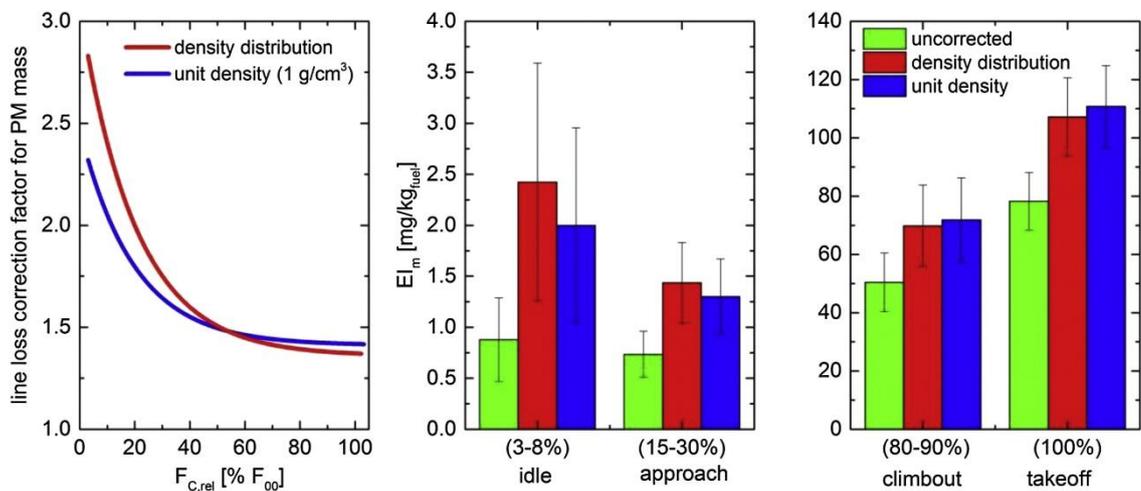
Figure 4.6   *Line-loss correction factors as a function of engine thrust and comparison of the line loss corrected eBC mass. Error bars represent one standard deviation of the averaged data.*

Overall, our results agree both qualitatively and quantitatively with previous BC mass data for CFM56-7B engines obtained both at the engine exit plane and tens of meters downstream (Lobo et al., 2007b; Timko et al., 2010a). All the BC mass data follow a similar curve with a local maximum at ground idle, a global minimum at ~10–15 %

rated thrust, and peak emissions at maximum thrust. In reality, the idle emissions are much higher than measured due to the high loss of these extremely small particles in the 30 + m long transfer lines, as discussed in the next section.

4.3.4 Line-loss corrected eBC mass

The line loss correction factor is highest at engine idle when the engine generates the smallest particles that are most affected by diffusional losses (Figure 4.6). The effective density correction (red bars) predicts 60 % PM mass loss at idle and it levels off at ~27 % for 80 % thrust and higher. This is due to the independence of diffusional losses on particle size for bigger particles that contribute most to the mass concentration at high thrust (VMD > 100 nm, Figure 4.4). The assumed unit density provided very reasonable estimates with respect to the effective density method (blue bars). The two methods agreed within 20 % at idle to less than 5 % at high thrust. It should be noted here that the results depend on the thermophoretic losses that were estimated from the temperature gradient between the exhaust gas and the sample line. This part needs further refinement by measuring the gas temperature at the probe tip. Nevertheless, a similar range and trend of line loss correction for PM mass is expected for all single annular combustor engines measured with the standardized sampling systems.

4.4 Conclusions

We have utilized the particle effective density determined over the entire operating range of a CFM56-7B26/3 engine to (1) determine PM mass concentrations using the IPSD technique and (2) to estimate the PM mass emissions at the engine exit. As the PM emissions from aircraft turbine engines decrease, the PM mass is becoming difficult to measure with the mass-based techniques. We have shown here that the IPSD technique agreed well with the real-time BC mass data, and may offer higher sensitivity for measurements of ultra-low PM emissions. It is not expected that this labor-intensive technique would be adapted for the industrial practice but its research application could lead to robust estimates useful for practical calculations. We have shown here that the unit particle density (1000 kg/m^3), widely assumed in aircraft PM studies to convert PSD to PM mass, is a reasonable estimate for the engine tested here. This engine is the upgraded version of the CFM56-7B that is the most popular engine in commercial aviation, representative of the modern single annular combustor engines. Therefore, this finding may be applicable to a large fraction of the current fleet. The

practical value of the unit density comes into play in the correction of PM mass losses in the sampling system. We have shown here that neglecting the PM mass losses would lead to a severe underestimation of the total emissions. Approximately 60 % of the PM mass is lost in the standardized sampling system at engine idle and around 27 % at high thrust using the size-resolved effective density. The unit density led to estimates that were within 20 % and 5 % at idle and high thrust, respectively.

Results of this study could be used to advance the development of a robust line loss correction methodology for PM mass data reported by the engine manufacturers in the future ICAO emissions database. In order to use these data for accurate environmental assessment, we suggest that the penetration functions of the exhaust sampling systems together with GMD and GSD values should be provided in the database.

Acknowledgments

Supplementary data

The supplementary data related to this article can be found at http://dx.doi.org /10.1016/ j.atmosenv.2014.10.018.

5 CONCLUSIONS

5.1 Summary of results

Aircraft emissions are an important anthropogenic source of soot particles in the upper troposphere and near airports, where they can impact air quality and influence climate. It is known that particles emitted by aircraft can initiate the formation of contrails (Schumann, 1996), which, depending on the conditions, can persist, spread and even emerge into cirrus clouds (Minnis et al., 1998). The latter process also depends on the ice nucleating properties of these particles and causes the largest aviation-induced radiative forcing (Burkhardt & Kärcher, 2011). Kärcher et al. (2007) stresses that soot particles potentially can act as cloud condensation nuclei and ice nucleating particles, and Cozic et al. (2008) showed that some fraction of carbon-containing particles act as ice nucleating particles. However, the microphysical processes are not yet completely understood (Kärcher et al., 2007; Zhou & Penner, 2014) and the question of which aerosol species are actually responsible for ice nucleation remains to be clarified. In order to assess these effects, knowledge of their chemical and physical properties is crucial. Thus, experimental measurements were performed on freshly emitted particulate matter from aircraft engine emissions to provide new information.

Soot particles formed by different combustion processes also differ in their physical properties such as size, mass, density and morphology, which are important for their transport and interactions with other aerosol species. Soot particles are fractal aggregates consisting of coagulated, nearly spherical primary particles. Hence, the morphology of soot particles depends on the number and size of the primary particles as well as on the degree of compaction of the agglomerate, and is often described using the effective density and fractal dimension (Maricq, 2007; Shapiro et al., 2012). The effective density of fractal particles depends on the particle size whereas the fractal dimension does not, because fractal objects are self-similar, i.e. they resemble a segment of itself. The fractal dimension is related to the arrangement of the primary particles within the agglomerate, ranging from an infinite long straight chain-like structure (fractal dimension of one) and a perfect sphere without voids (fractal dimension of three) (Schmidt-Ott et al., 1990; Xiong & Friedlander, 2001). The fractal dimension is important to

<mark>describe the transport behavior and the interaction with radiation of fractal particles (Zhang et al., 2008).</mark>

The measurements on aircraft soot were conducted in a test facility at the Zurich Airport, using a standardized experimental set-up where samples were taken directly behind the engine for the development of a new certification standard for aircraft emissions. This offered a unique and highly favorable opportunity to sample and investigate fresh aircraft emissions.

5.1.1 Chemical characterization of freshly emitted particulate matter from aircraft exhaust using single particle mass spectrometry

Using the ATOFMS ~~the~~ first ever extensive chemical characterization of single exhaust particles emitted from three different in-production aircraft turbofan engines over their entire operating range was performed. However, due to instrument limitations the particles analyzed by the ATOFMS represent the largest size fraction of particles emitted by the engine. Depending on engine type, 94.5 % to 97.5 % of the particles contained elemental carbon, with elemental carbon to total carbon ratios ranging from 0.83 to 0.99 regardless of engine type. For each engine, the exhaust particles were grouped into particle types comprising of particles with similar chemical composition. The majority of the identified particle types were detected in all engines, with similar number fractions.

A dominant fraction of ice residuals collected in cirrus clouds contain metallic compounds (Cziczo et al., 2013). Moreover, it has been showed that some metallic compounds in particles can be responsible for their and cause effects on human health (Pagan et al., 2003). Therefore, the soot particles were analysed for metallic compounds, which were only internally mixed and found in more than 36 % of soot particles. The elements Cr, Fe, Mo, Na, Ca, Al, V, Ba, Co, Cu, Ni, Pb, Mg, Mn, Si and Ti were detected in particles from all engines, whereas Zr was only detected in particles from two of the engines. These results suggest that aircraft engine emissions could be a considerable source of potential INP in the upper troposphere. Because the fractions of metal-containing particles did not show a size-dependence in our investigated size-range, we conclude that they will be present in smaller particles, too.

Sampling the particles directly behind the engine offered the opportunity to use inductively coupled plasma mass spectrometry to investigate the sources of the detected metallic compounds. The sources considered were kerosene, lubricant oil and debris

from wearing components from the engine, and all compounds were detected in kerosene and/or in oil except for cobalt and zirconium. Based on the element concentration in the samples and their appearance in the engine, we inferred probable sources. Iron, copper, chromium and nickel originate mainly from engine wear too, but other sources cannot be excluded. Molybdenum originates from engine wear, grease or both. The most probable source of calcium, sodium, barium, vanadium, lead and titanium is attributed to be either fuel or oil. However, as the ambient air needed for the combustion usually shows detectable concentrations of calcium and sodium, it has to be considered as an additional potential source of these elements. The results did not point to a main source for aluminium, silicon, magnesium and manganese. We conclude that cobalt, zirconium or the combination of both elements could be possibly used as an atmospheric tracer for aircraft emissions.

5.1.2 Effective density and mass–mobility exponents of particulate matter in aircraft turbine exhaust: dependence on engine thrust and particle size

The effective density and the fractal dimension were determined for the non-volatile particles emitted by a CFM56-7B26/3 aircraft engine using two DMA-CPMA-CPC systems, one operated by the author and the other by EPMA. This engine is widely used and representative for modern single annular combustor engines. The DMA-CPMA-CPC systems measured the size-resolved mass of the particles, and two systems were used to cover the entire engine thrust range as well as the complete particle size range in the time available. At constant engine thrust, the effective density decreased with increasing particle mobility size (d_m), and for a certain particle size the effective density generally increased with increasing thrust. With increasing thrust, it ranged from $1075 \, \text{kg/m}^3$ to $1490 \, \text{kg/m}^3$ for 30 nm size particles and $530 \, \text{kg/m}^3$ to $1020 \, \text{kg/m}^3$ for 75 nm. Particles larger than 100 nm were only measured at thrusts levels greater than 67 % due to low concentrations at lower thrust, and the effective density approaches $\sim 800 \, \text{kg/m}^3$ for $d_m = 150$ nm. The measured fractal dimensions ranged from 1.85 to 2.32 for thrust levels <30 % and from 2.54 to 2.79 for thrust levels >30 %, which implies more closely packed soot agglomerates at higher engine thrust.

The measured mass distributions were unimodal, except for particles with d_m smaller than 30 nm, where it was assumed that the selected mobility size was close to the size of one primary particle. When the number of primary particles was one, the effective density approaches the material density, corresponding to the measured maximum value

of 1865 ± 291 kg/m^3. Furthermore, our results imply that the primary particle size decreases with decreasing thrust. This was inferred from the observation that the minimum mobility size (obtained by extrapolating the effective densities distribution to the assumed material density) decreased with decreasing thrust. This outcome agrees with a study by Liati et al. (2014) performed in the same campaigns using transmission electron microscopy to analyse exhaust particles at different engine thrust.

The determined effective densities and mass-mobility exponents were compared to values obtained by Johnson et al. (2015) during an earlier campaign at the Zurich Airport in the same test cell for the exhaust particles emitted by a CFM56-5B4/2P engine using a CPMA-DMA-CPC system. For particles emitted by the CFM56-7B26/3 and the CFM56-5B4/2P engine with $d_m > 40$ nm, the effective densities agreed within the uncertainty range whereas for smaller particles our measurements (CFM56-7B26/3) showed higher effective densities. The fractal dimensions obtained at ~20 % thrust differed significantly between the two engines with values of ~2.7 and ~2.2 for the exhaust particles emitted by the CFM56-5B4/2P and the CFM56-7B26/3 engine, respectively. This indicates that the particles emitted by the CFM56-5B4/2P engine were more closely packed in the range of these low thrust levels. We attribute these differences to differences in the engine combustion processes. However, it cannot be excluded that variations in the experimental set-up also contributed to some extent.

5.1.3 Determination of PM mass emissions from an aircraft turbine engine using particle effective density

Accurate and standardized measurement of aircraft emissions in terms of PM mass is important for the certification of aircraft engines and climate and air quality models. In addition to the method used for the determination of PM mass, losses in the sampling system have to be considered. EMPA was responsible for the characterization of the entire experimental set-up in order to evaluate it with regard to its use as a certification standard, and the effective density distributions used for this evaluation was collected in a collaboration between ETH and EMPA. To determine PM mass concentrations at the instruments and total actual emissions of the PM mass behind the engine exit, the particle effective densities were measured for the entire thrust range of a CFM56-7B26/3 engine. The mean effective density is the ratio of the total PM mass to the total PM volume, and it was determined for each thrust level by weighting the measured effective density distribution with the PM volume derived from the Particle Size Distribution

(PSD) measurements. The mean effective density was within 10 % of the unit density (1000 kg/m^3). Thus, the unit particle density is a good approach to convert PSDs into PM mass for the CFM56-7B26/3 engine. The determined PM mass concentrations agreed well with real-time BC mass data measured by a Micro Soot Sensor and a laser-induced incandescence instrument. The measured effective density distributions and the unit density were further used to predict PM mass losses in the sampling system using a line loss correction model. This model uses a particle penetration function estimated from the size-dependent particle transport efficiency. Using the effective density distributions, the predicted loss of PM mass within the experimental set-up was ~60 % at idle and ~27 % for high thrust ≥80 %. These values were within 20 % at idle and 5 % at high thrust compared to the predicted PM loss using the unit density.

5.2 Outlook

This section provides ideas and thoughts for potential further research based on the findings of this thesis. The suggestions are meant to promote scientists in field of atmospheric science and experimentalists measuring aircraft exhaust to invest its implication on air quality, climate and human health.

In chapter 2 it was shown that a considerable fraction of the analyzed particles from a widely used aircraft engine contained different metallic compounds that were internally mixed with the soot particles. Cziczo et al. (2009) showed that for example lead-containing soot particles can effectively act as ice nucleating particles, which implies that metal-containing soot particles directly emitted from aircraft can potentially initiate ice formation. Based on these findings, the role of metal-containing aircraft exhaust particles in ice nucleation processes in general needs to be clarified. We therefore recommend performing experiments on the ice-nucleating properties of fresh soot particles that contain individual metallic compounds we have detected in aircraft exhaust. This can be done using a continuous flow diffusion chamber (DeMott et al., 2015) such the ice nucleation chamber presented by Stetzer et al. (2008).

The particle types identified for the PM aircraft emissions presented in chapter 2 can be used to identify ambient particles from aircraft engine emissions and distinguish them from soot particles of other sources. Our results presented in chapter 2 showed that the origin of cobalt and zirconium were detected in the exhaust particles are engine wearing. Thus, they could serve as tracers for PM aircraft engine emissions and to identify soot particles from aircraft engines.

The identification of soot particles from aircraft emissions in the atmosphere can in turn be used to investigate these particles after ageing and compare their chemical composition size, mass and information on morphology to the new measurements of fresh particles provided here. Sampling of aged particles can be done near airports or behind aircraft in flight. Another approach is to artificially generate such particles by mimicking the ageing process in-situ using a reaction chamber that simulates atmospheric ageing as presented by Platt et al. (2013). The results would give insight into the timescale of important transformation processes such as the restructuring and the uptake of organic material of the soot particles. The results would give insight into the timescale of important transformation processes such as the restructuring and the uptake of organic material of the soot particles.

Aircraft exhaust is important with respect the air quality near airport (Keuken et al., 2015) and also on larger scales (Yim et al., 2015). It was shown that particles containing metals such as vanadium, iron, copper and nickel can cause epithelial injuries (Pagan et al., 2003) and Janssen et al. (2012) stressed that BC probably acts as a carrier for toxic substances. We therefore recommend investigating the toxicity of soot particles containing the detected metals (cp. chapter 2) in the aircraft engine emissions. Such particles can be produced in the lab and such investigations would substantially contribute to the understanding of the effects of PM aircraft emissions on human health.

For the experiments presented chapter 3 and 4 two DMA-CPMA-CPC systems were used due to time limitations. Ideally, future measurements should use a CPMA-DMA-CPC instead in order to reduce time needed for one measurement, allowing the simultaneous determination of mass and size. The results showed that the unit particle density is a reasonable and convenient approach to convert particle size distributions to PM mass for the CFM56-7B26/3 engine. Thus, the information on the physical properties of the engine exhaust particles provided in these chapters could be used in emission protocols. Since the CFM56-7B26/3 engine is representative of modern single annular combustor engines, this finding is possibly applicable to a large fraction of aircraft engines. Nevertheless, we suggest collecting data from more different engine types to confirm this.

ACKNOWLEDGEMENTS

This thesis would not have been possible without the dedicated support of many people that crossed my way during the last three and a half years.

- First, I thank my supervisor Berko Sierau. He helped and encouraged me not only scientifically but also in managing such a PhD project. He shared his sophisticated expertise with the laboratory instruments and tought me useful skills in managing projects.

- Ulrike Lohmann who gave me the great opportunity to carry out this PhD project and to participate to her group. Her scientific competence and know-how always resulted in fruitful discussions during our meetings.

- All my co-authors, from whom I always got supportive input, who helped me improve the analysis and gain new insights evaluating the results. They taught me that many eyes see more than only two, and that collaboration (though not always straightforward) is essential to move forward in science.

- Frithjof Siegerist from SR Technics who was always very helpful during the measurement campaigns. He never considered himself too good for hurrying around the airport to provide us with material we needed. Moreover, he was interested in our measurements which, combined with his knowledge on aircraft engines, always resulted in beneficial discussions.

- Hannes Wydler, our group's technician. Whenever there were troubles in the lab, he provided the necessary calm not to lose one's head and the ideas to find an adequate solution.

- Jim Atkinson who helped to improve my written english and provided me with critical feedback and Fabian Mahrt who put much effort in the maintenance and in improving the performance of the ATOFMS.

- Andreas Petzold who agreed to be my co-examiner at my PhD defence and showed high flexibility under changing circumstances.

- My parents who have always supported my decicions and encouraged me unconditionally.

- Nicole, my then-girlfriend and now-wife, who provided me with the necessary sympathy and back up when things were messy and I needed someone to lend me an ear or two. Her independent advice helped me to see things from a different point of view when I was stuck deeply in my work.

Curriculum vitae

Abegglen Manuel, born 17 March 1983 in Münsterlingen, citizen of Iseltwald (BE), Switzer-land.

Education

03/2016 (expected)	PhD, Swiss Federal Institute of Technology, Zurich (ETHZ), Switzerland, Institute for Atmospheric and Climate Science (IAC).
04/2012	MSc in Environmental Science, Swiss Federal Institute of Technology, Zurich (ETHZ), Switzerland, Department of Environmental System Science.
03/2009	BSc in Environmental Science, Swiss Federal Institute of Technology, Zurich (ETHZ), Switzerland, Department of Environmental System Science.
07/2002	High School, Romanshorn, Switzerland, Eidgenössische Matur.

Professional experience

09/2011–04/2012	Internship at the office for "Environment and Energy" of the canton St. Gallen (AFU), division for "Energy and Air/Air quality".

Publications

Abegglen, M., Durdina, L., Brem, B. T., Wang, J., Rindlisbacher, T., Corbin, J. C., Lohmann, U. & Sierau, B.: *Effective density and mass-mobility exponents of particulate matter in aircraft turbine exhaust: Dependence on engine thrust and particle size.* Journal of Aerosol Science, 88, 135-147. doi: http://dx.doi.org/10.1016/j.jaerosci.2015.06.003, 2015.

Durdina, L., Brem, B. T., Abegglen, M., Lobo, P., Rindlisbacher, T., Thomson, K. A., Smallwood, G. J., Hagen, D. E., Sierau, B. & Wang, J.: *Determination of PM mass emissions from an aircraft turbine engine using particle effective density.* Atmospheric Environment, 99, 500–507, http://dx.doi.org/10.1016/j.atmosenv.2014.10.018, 2014.

Lobo, P., Smallwood, G. J., Rindlisbacher, T., Siegerist, F., Black, E. A., Yu, Z., Mensah, A. A., Hagen, D. E., Miake-Lye, R. C., Thomson, K. A., Brem, B. T., Corbin, J. C., Abegglen, M., Sierau, B., Whitefield, P. D. & Wang, J. *Measurement of Aircraft Engine Non-Volatile PM Emissions: Results of the Aviation-Particle Regulatory Instrumentation Demonstration Experiment (A-PRIDE) 4 Campaign*. Aerosol Science and Technology, 49:7, 472-484, DOI: 10.1080/02786826.2015.1047012, 2015.

Submitted to the Journal of Atmospheric Environment: Abegglen M, Brem B., Ellenrieder M., Durdina L., Rindlisbacher T., Wang J., Lohmann U. and Sierau B.: *Chemical characterization of freshly emitted particulate matter from aircraft exhaust using single particle mass spectrometry.*

Oral presentations

M. Abegglen, B. Sierau, B. Brem, J. Wang, T. Rindlisbacher and U. Lohmann. *Chemical characterization of particulate matter aircraft turbine engine exhaust using single particle mass spectrometry.* 4th International Conference on Transport, Atmosphere and Climate (TAC-4), Bad Kohlgrub, Germany, June 2015.

M. Abegglen, B. Brem, J. Wang, T. Rindlisbacher, U. Lohmann and B. Sierau. *Chemical characterization of particulate matter aircraft turbine engine exhaust using single particle mass spectrometry.* 19th ETH-Conference on Combustion Generated Nanoparticles (NPC), Zurich, Switzerland, June/July 2015.

Poster presentations

M. Abegglen, B. Sierau, A. A. Mensah, J. Wang, L. Durdina, M. Gysel, U. Lohmann. *Effective density measurements of different fresh soot types.* European Aerosol Conference (EAC), Prague, Czech Republic, September 2013.

M. Abegglen, L. Durdina, B. Brem, T. Rindlisbacher, J. Wang, U. Lohmann, and B. Sierau. *Effective density measurements of aircraft exhaust.* European Geosciences Union (EGU), Vienna, Austria, April/May 2014.

REFERENCES

Abegglen, M., L. Durdina, B. T. Brem, J. Wang, T. Rindlisbacher, J. C. Corbin, et al., 2015: Effective density and mass–mobility exponents of particulate matter in aircraft turbine exhaust: Dependence on engine thrust and particle size. *Journal of Aerosol Science, 88*, 135-147. doi: http://dx.doi.org/10.1016/j.jaerosci.2015.06.003

Agrawal, H., A. A. Sawant, K. Jansen, J. Wayne Miller, & D. R. Cocker Iii, 2008: Characterization of chemical and particulate emissions from aircraft engines. *Atmospheric Environment, 42*(18), 4380-4392. doi: http://dx.doi.org/10.1016/j.atmosenv.2008.01.069

Anderson, B. E., 2011: Alternative Aviation Fuel Experiment (AAFEX). NASA/TM, 2011–217059. National Aeronautics and Space Administration, Langley Research Center, Hampton, Va.

Barrett, S. R. H., R. E. Britter, & I. A. Waitz, 2013: Impact of aircraft plume dynamics on airport local air quality. *Atmospheric Environment, 74*, 247-258. doi: http://dx.doi.org/10.1016/j.atmosenv.2013.03.061

Beyersdorf, A. J., M. T. Timko, L. D. Ziemba, D. Bulzan, E. Corporan, S. C. Herndon, et al., 2013: Reductions in aircraft particulate emissions due to the use of Fischer–Tropsch fuels. *Atmos. Chem. Phys. Discuss., 13*(6), 15105-15139. doi: 10.5194/acpd-13-15105-2013

Birch, M. E., 2002: Occupational Monitoring of Particulate Diesel Exhaust by NIOSH Method 5040. *Applied Occupational and Environmental Hygiene, 17*(6), 400-405. doi: 10.1080/10473220290035390

Boies, A. M., M. E. J. Stettler, J. J. Swanson, T. J. Johnson, J. S. Olfert, M. Johnson, et al., 2015: Particle Emission Characteristics of a Gas Turbine with a Double Annular Combustor. *Aerosol Science and Technology, 49*(9), 842-855. doi: 10.1080/02786826.2015.1078452

Bond, T. C., S. J. Doherty, D. W. Fahey, P. M. Forster, T. Berntsen, B. J. DeAngelo, et al., 2013: Bounding the role of black carbon in the climate system: A scientific assessment. *Journal of Geophysical Research: Atmospheres*, n/a–n/a. doi: 10.1002/jgrd.50171

Boucher, O., D. Randall, P. Artaxo, C. Bretherton, G. Feingold, P. Forster, et al., 2013: Clouds and Aerosols. In: *Climate Change 2013: The Physical Science Basis. Contribution of Working Group I to the Fifth Assessment Report of the Intergovernmental Panel on Climate Change* [Stocker, T.F., D. Qin, G.-K. Plattner, M. Tignor, S.K. Allen, J. Boschung, A. Nauels, Y. Xia, V. Bex and P.M. Midgley (Eds.)]. Cambridge University Press, Cambridge, United Kingdom and New York, NY, USA.

Braun, A., F. E. Huggins, S. Seifert, J. Ilavsky, N. Shah, K. E. Kelly, et al., 2004: Size-range analysis of diesel soot with ultra-small angle X-ray scattering. *Combustion and Flame, 137*(1–2), 63-72. doi: http://dx.doi.org/10.1016/j.combustflame.2004.01.003

Brem, B., L. Durdina, F. Siegerist, P. Beyerle, K. Bruderer, T. Rindlisbacher, et al., 2015: Effects of fuel aromatic content on non-volatile particulate emissions of an in-

production aircraft gas turbine. *Environmental Science & Technology*. doi: 10.1021/acs.est.5b04167

Brundish, K. D., A. R. Clague, C. W. Wilson, R. C. Miake-Lye, R. C. Brown, J. Wormhoudt, et al., 2007: Evolution of Carbonaceous Aerosol and Aerosol Precursor Emissions Through a Jet Engine. *Journal of Propulsion and Power, 23*(5), 959-970. doi: 10.2514/1.27502

Burkhardt, U., & B. Kärcher, 2011: Global radiative forcing from contrail cirrus. *Nature Climate Change, 1*, 54-58. doi: 10.1038/nclimate1068

Burtscher, H., 2005: Physical characterization of particulate emissions from diesel engines: a review. *Journal of Aerosol Science, 36*, 896-932. doi: 10.1016/j.jaerosci.2004.12.001

Cape, J. N., M. Coyle, & P. Dumitrean, 2012: The atmospheric lifetime of black carbon. *Atmospheric Environment, 59*, 256-263. doi: 10.1016/j.atmosenv.2012.05.030

Cheng, M.-D., E. Corporan, M. J. DeWitt, C. W. Spicer, M. W. Holdren, K. A. Cowen, et al., 2008: Probing Emissions of Military Cargo Aircraft: Description of a Joint Field Measurement Strategic Environmental Research and Development Program. *Journal of the Air & Waste Management Association, 58*, 787-796. doi: 10.3155/1047-3289.58.6.787

Corbin, J. C., U. Lohmann, B. Sierau, A. Keller, H. Burtscher, & A. A. Mensah, 2015: Black carbon surface oxidation and organic composition of beech-wood soot aerosols. *Atmos. Chem. Phys., 15*(20), 11885-11907. doi: 10.5194/acp-15-11885-2015

Corporan, E., A. Quick, & M. J. DeWitt, 2008: Characterization of particulate matter and gaseous emissions of a C-130H aircraft. *J Air Waste Manag Assoc, 58*(4), 474-483.

Cozic, J., S. Mertes, B. Verheggen, D. J. Cziczo, S. J. Gallavardin, S. Walter, et al., 2008: Black carbon enrichment in atmospheric ice particle residuals observed in lower tropospheric mixed phase clouds. *Journal of Geophysical Research: Atmospheres, 113*(D15), n/a-n/a. doi: 10.1029/2007JD009266

Crayford, A., M. Johnson, R. Marsh, Y. Sevcenco, D. Walters, P. Williams, et al., 2012: Studying, Sampling and Measuring of Aircraft Particulate Emissions III–Specific Contract 02: SAMPLE III-SC. 02.

Cziczo, D. J., K. D. Froyd, C. Hoose, E. J. Jensen, M. Diao, M. A. Zondlo, et al., 2013: Clarifying the Dominant Sources and Mechanisms of Cirrus Cloud Formation. *Science, 340*(6138), 1320-1324. doi: 10.1126/science.1234145

Cziczo, D. J., O. Stetzer, A. Worringen, M. Ebert, S. Weinbruch, M. Kamphus, et al., 2009: Inadvertent climate modification due to anthropogenic lead. *Nature Geosci, 2*(5), 333-336. doi: http://www.nature.com/ngeo/journal/v2/n5/suppinfo/ngeo499_S1.html

Dastanpour, R., & S. N. Rogak, 2014: Observations of a Correlation Between Primary Particle and Aggregate Size for Soot Particles. *Aerosol Science and Technology, 48*(10), 1043-1049. doi: 10.1080/02786826.2014.955565

DeCarlo, P. F., J. G. Slowik, D. R. Worsnop, P. Davidovits, & J. L. Jimenez, 2004: Particle Morphology and Density Characterization by Combined Mobility and Aerodynamic Diameter Measurements. Part 1: Theory. *Aerosol Science and Technology, 38*, 1185-1205. doi: 10.1080/027868290903907

Demirdjian, B., D. Ferry, J. Suzanne, O. B. Popovicheva, N. M. Persiantseva, & N. K. Shonija, 2007: Heterogeneities in the Microstructure and Composition of Aircraft Engine Combustor Soot: Impact on the Water Uptake. *Journal of Atmospheric Chemistry, 56*(1), 83-103. doi: 10.1007/s10874-006-9043-9

DeMott, P. J., 1990: An Exploratory Study of Ice Nucleation by Soot Aerosols. *Journal of Applied Meteorology, 29*(10), 1072-1079. doi: 10.1175/1520-0450(1990)029<1072:AESOIN>2.0.CO;2

DeMott, P. J., D. J. Cziczo, A. J. Prenni, D. M. Murphy, S. M. Kreidenweis, D. S. Thomson, et al., 2003: Measurements of the concentration and composition of nuclei for cirrus formation. *Proceedings of the National Academy of Sciences, 100*(25), 14655-14660. doi: 10.1073/pnas.2532677100

DeMott, P. J., A. J. Prenni, G. R. McMeeking, R. C. Sullivan, M. D. Petters, Y. Tobo, et al., 2015: Integrating laboratory and field data to quantify the immersion freezing ice nucleation activity of mineral dust particles. *Atmos. Chem. Phys., 15*(1), 393-409. doi: 10.5194/acp-15-393-2015

Diehl, K., & S. K. Mitra, 1998: A laboratory study of the effects of a kerosene-burner exhaust on ice nucleation and the evaporation rate of ice crystals. *Atmospheric Environment, 32*(18), 3145-3151. doi: http://dx.doi.org/10.1016/S1352-2310(97)00467-6

Duda, D. P., P. Minnis, K. Khlopenkov, T. L. Chee, & R. Boeke, 2013: Estimation of 2006 Northern Hemisphere contrail coverage using MODIS data. *Geophysical Research Letters, 40*(3), 612-617. doi: 10.1002/grl.50097

Durdina, L., B. T. Brem, M. Abegglen, P. Lobo, T. Rindlisbacher, K. A. Thomson, et al., 2014: Determination of PM mass emissions from an aircraft turbine engine using particle effective density. *Atmospheric Environment, 99*, 500-507. doi: 10.1016/j.atmosenv.2014.10.018

EASA, 2012: SAMPLE III: Contribution to aircraft engine PM certification requirement and standard; Second Specific Contract − Final Report.

Ehara, K., C. Hagwood, & K. J. Coakley, 1996: Novel method to classify aerosol particles according to their mass-to-charge ratio—Aerosol particle mass analyser. *Journal of Aerosol Science, 27*, 217-234. doi: 10.1016/0021-8502(95)00562-5

EPA, 2010: Report to Congress on Black Carbon. Washington DC: U.S. Environmental Protection Agency. Available at: http://www.epa.gov/blackcarbon/.

Epshteyn, Y., & T. J. Risdon, 2010: Molybdenum disulfide in lubricant applications − a review. In: The 12th lubricating grease conference (NLGI-India Chapter) (pp. 1-12). Goa, India.

Ferge, T., E. Karg, A. Schröppel, K. R. Coffee, H. J. Tobias, M. Frank, et al., 2006: Fast Determination of the Relative Elemental and Organic Carbon Content of Aerosol Samples by On-Line Single-Particle Aerosol Time-of-Flight Mass Spectrometry. *Environmental Science & Technology, 40*, 3327-3335. doi: 10.1021/es050799k

Ferry, D., C. Rolland, D. Delhaye, F. Barlesi, P. Robert, P. Bongrand, et al., 2011: Jet exhaust particles alter human dendritic cell maturation. *Inflammation Research, 60*(3), 255-263. doi: 10.1007/s00011-010-0262-9

Fordyce, J. S., & D. W. Sheibley, 1975: Estimate of Contribution of Jet Aircraft Operations To Trace Element Concentration at or near Airports. *Journal of the Air Pollution Control Association, 25*(7), 721-724. doi: 10.1080/00022470.1975.10470131

Friedlander, S. K. (2000). *Smoke, Dust, and Haze: Fundamentals of Aerosol Dynamics* (2 ed.): Oxford University Press, USA.

Gard, E., J. E. Mayer, B. D. Morrical, T. Dienes, D. P. Fergenson, & K. A. Prather, 1997: Real-Time Analysis of Individual Atmospheric Aerosol Particles: Design and Performance of a Portable ATOFMS. *Analytical Chemistry, 69*(20), 4083-4091. doi: 10.1021/ac970540n

Gelencser, A. (2004). Major Carbonaceous Particle Types and their Sources *Carbonaceous Aerosol* (Vol. 30, pp. 45-147): Springer Netherlands.

Ghazi, R., & J. S. Olfert, 2013: Coating Mass Dependence of Soot Aggregate Restructuring due to Coatings of Oleic Acid and Dioctyl Sebacate. *Aerosol Science and Technology, 47*(2), 192-200. doi: 10.1080/02786826.2012.741273

Gilmour, P. S., A. Ziesenis, E. R. Morrison, M. A. Vickers, E. M. Drost, I. Ford, et al., 2004: Pulmonary and systemic effects of short-term inhalation exposure to ultrafine carbon black particles. *Toxicology and Applied Pharmacology, 195*(1), 35-44. doi: http://dx.doi.org/10.1016/j.taap.2003.10.003

Giorio, C., A. Tapparo, M. Dall'Osto, R. M. Harrison, D. C. S. Beddows, C. Di Marco, et al., 2012: Comparison of three techniques for analysis of data from an Aerosol Time-of-Flight Mass Spectrometer. *Atmospheric Environment, 61*, 316-326. doi: 10.1016/j.atmosenv.2012.07.054

Gross, D. S., R. Atlas, J. Rzeszotarski, E. Turetsky, J. Christensen, S. Benzaid, et al., 2010: Environmental chemistry through intelligent atmospheric data analysis. *Environmental Modelling & Software, 25*(6), 760-769. doi: http://dx.doi.org/10.1016/j.envsoft.2009.12.001

Gross, D. S., M. E. Gälli, P. J. Silva, & K. A. Prather, 2000: Relative Sensitivity Factors for Alkali Metal and Ammonium Cations in Single-Particle Aerosol Time-of-Flight Mass Spectra. *Analytical Chemistry, 72*(2), 416-422. doi: 10.1021/ac990434g

Gross, J. H. (2011). *Mass Spectrometry: a textbook* (2nd ed.): Springer Berlin Heidelberg.

Hagen, D., P. Whitefield, J. Paladino, M. Trueblood, & H. Lilenfeld, 1998: Particulate sizing and emission indices for a jet engine exhaust sampled at cruise. *Geophysical Research Letters, 25*(10), 1681-1684. doi: 10.1029/97GL03504

Han, C., Y. Liu, J. Ma, & H. He, 2012: Key role of organic carbon in the sunlight-enhanced atmospheric aging of soot by O(2). *Proceedings of the National Academy of Sciences of the United States of America, 109*(52), 21250-21255. doi: 10.1073/pnas.1212690110

Hatch, L. E., K. A. Pratt, J. A. Huffman, J. L. Jimenez, & K. A. Prather, 2014: Impacts of Aerosol Aging on Laser Desorption/Ionization in Single-Particle Mass Spectrometers. *Aerosol Science and Technology, 48*(10), 1050-1058. doi: 10.1080/02786826.2014.955907

Haynes, I., 1997: Hastelloy® X Alloy [Brochure]. Kokomo, IN: Author.

Healy, R. M., J. Sciare, L. Poulain, M. Crippa, A. Wiedensohler, A. S. H. Prévôt, et al., 2013: Quantitative determination of carbonaceous particle mixing state in Paris using single-particle mass spectrometer and aerosol mass spectrometer measurements. *Atmos. Chem. Phys., 13*(18), 9479-9496. doi: 10.5194/acp-13-9479-2013

Hendricks, J., B. Kärcher, & U. Lohmann, 2011: Effects of ice nuclei on cirrus clouds in a global climate model. *Journal of Geophysical Research: Atmospheres, 116*(D18), n/a-n/a. doi: 10.1029/2010JD015302

Hendricks, J., B. Kärcher, U. Lohmann, & M. Ponater, 2005: Do aircraft black carbon emissions affect cirrus clouds on the global scale? *Geophysical Research Letters, 32*(12), n/a-n/a. doi: 10.1029/2005GL022740

Herndon, S. C., J. T. Jayne, P. Lobo, T. B. Onasch, G. Fleming, D. E. Hagen, et al., 2008: Commercial Aircraft Engine Emissions Characterization of in-Use Aircraft at Hartsfield-Jackson Atlanta International Airport. *Environmental Science & Technology, 42*, 1877-1883. doi: 10.1021/es072029+

Heymsfield, A., D. Baumgardner, P. DeMott, P. Forster, K. Gierens, & B. Kärcher, 2010: Contrail Microphysics. *Bulletin of the American Meteorological Society, 91*(4), 465-472. doi: 10.1175/2009BAMS2839.1

Highwood, E. J., & R. P. Kinnersley, 2006: When smoke gets in our eyes: the multiple impacts of atmospheric black carbon on climate, air quality and health. *Environment international, 32*(4), 560-566. doi: 10.1016/j.envint.2005.12.003

Hinds, W. C. (1999). *Aerosol Technology: Properties, Behavior, and Measurement of Airborne Particles* (2nd ed.): John Wiley & Sons.

Howard, J. B., & W. J. Kausch Jr, 1980: Soot control by fuel additives. *Progress in Energy and Combustion Science, 6*(3), 263-276. doi: http://dx.doi.org/10.1016/0360-1285(80)90018-0

Howard, R. P., J. C. Wormhoudt, & P. D. Whitefield, 1996: Experimental characterization of gas turbine emissions at simulated flight altitude conditions. Final report, January 1995-April 1996 *Other Information: PBD: Sep 1996* (pp. Medium: P; Size: 158 p.).

Hsu, H.-H., G. Adamkiewicz, E. Andres Houseman, J. Vallarino, S. J. Melly, R. L. Wayson, et al., 2012: The relationship between aviation activities and ultrafine particulate matter concentrations near a mid-sized airport. *Atmospheric Environment, 50*, 328-337. doi: http://dx.doi.org/10.1016/j.atmosenv.2011.12.002

ICAO, 2008: Annex 16 to the Convention on International Civil Aviation: Environmental Protection: Volume II Aircraft Engine Emissions. (3rd).

ICAO, 2013: Environmental Report. Aviation and Climate Change.

ICAO, 2014: ICAO Aircraft Engine Emissions Databank. Issue 20B. http://easa.europa.eu/environment/edb/datasheets/docs/edb-emissions-databank.xls.

IPCC, 1999: Aviation and the global atmosphere. A special report of Intergovernmental Panel on Climate Change working groups I and III. In J. E. Penner, D. H. Lister, D. J. Griggs, D. J. Dokken, & M. McFarland (Eds.). Cambridge, UK and New York, NY, USA: Cambridge University Press, UK.

IPCC, 2007: Climate Change 2007 - The Physical Science Basis: Working Group I Contribution to the Fourth Assessment Report of the Intergovernmental Panel on Climate Change. In S. Solomon, D. Qin, M. Manning, Z. Chen, M. Marquis, K. B. Averyt, M. Tignor, & H. L. Miller (Eds.): Cambridge University Press, UK.

Ivlev, L. S. (2010). Atmospheric Aerosols *Aerosols - Science and Technology* (pp. 343-378): Wiley-VCH Verlag GmbH & Co. KGaA.

Janssen, N. A., M. E. Gerlofs-Nijland, T. Lanki, R. O. Salonen, F. Cassee, G. Hoek, et al. (2012). *Health effects of black carbon*. World Health Organization, Copenhagen.

Jeong, C. H., M. L. McGuire, K. J. Godri, J. G. Slowik, P. J. G. Rehbein, & G. J. Evans, 2011: Quantification of aerosol chemical composition using continuous single particle measurements. *Atmos. Chem. Phys., 11*(14), 7027-7044. doi: 10.5194/acp-11-7027-2011

Jimenez, J. L., M. R. Canagaratna, N. M. Donahue, A. S. H. Prevot, Q. Zhang, J. H. Kroll, et al., 2009: Evolution of Organic Aerosols in the Atmosphere. *Science, 326*(5959), 1525-1529. doi: 10.1126/science.1180353

Johnson, T. J., J. S. Olfert, J. P. R. Symonds, M. Johnson, T. Rindlisbacher, J. J. Swanson, et al., 2015: Effective Density and Mass-Mobility Exponent of Aircraft Turbine Particulate Matter. *Journal of Propulsion and Power, 31*(2), 573-582. doi: 10.2514/1.B35367

Johnson, T. J., J. P. R. Symonds, & J. S. Olfert, 2013: Mass–Mobility Measurements Using a Centrifugal Particle Mass Analyzer and Differential Mobility Spectrometer. *Aerosol Science and Technology, 47*, 1215-1225. doi: 10.1080/02786826.2013.830692

Jones, J. M., L. I. Darvell, T. G. Bridgeman, M. Pourkashanian, & A. Williams, 2007: An investigation of the thermal and catalytic behaviour of potassium in biomass combustion. *Proceedings of the Combustion Institute, 31*(2), 1955-1963. doi: http://dx.doi.org/10.1016/j.proci.2006.07.093

Junge, C., 1955: The size distristribution and aging of natural aerosols as determined from electrical and optical data on the atmosphere. *Journal of Meteorology, 12(1)*, 13-25.

Kärcher, B., O. Möhler, P. J. DeMott, S. Pechtl, & F. Yu, 2007: Insights into the role of soot aerosols in cirrus cloud formation. *Atmos. Chem. Phys., 7*(16), 4203-4227. doi: 10.5194/acp-7-4203-2007

Kärcher, B., T. Peter, M. Biermann, & U. Schumann, 1996: The Initial Composition of Jet Condensation Trails. *Journal of the Atmospheric Sciences, 53*, 3066-3083. doi: 10.1175/1520-0469(1996)053<3066:TICOJC>2.0.CO;2

Keuken, M. P., M. Moerman, P. Zandveld, J. S. Henzing, & G. Hoek, 2015: Total and size-resolved particle number and black carbon concentrations in urban areas near Schiphol airport (the Netherlands). *Atmospheric Environment, 104*, 132-142. doi: http://dx.doi.org/10.1016/j.atmosenv.2015.01.015

Khalizov, A. F., H. Xue, L. Wang, J. Zheng, & R. Zhang, 2009: Enhanced Light Absorption and Scattering by Carbon Soot Aerosol Internally Mixed with Sulfuric Acid. *The Journal of Physical Chemistry A, 113*, 1066-1074. doi: 10.1021/jp807531n

Kim, S. C., J. Wang, W. G. Shin, J. H. Scheckman, & D. Y. H. Pui, 2009: Structural Properties and Filter Loading Characteristics of Soot Agglomerates. *Aerosol Science and Technology, 43*(10), 1033-1041. doi: 10.1080/02786820903131081

Kinsey, J. S., Y. Dong, D. C. Williams, & R. Logan, 2010: Physical characterization of the fine particle emissions from commercial aircraft engines during the Aircraft Particle Emissions eXperiment (APEX) 1–3. *Atmospheric Environment, 44*(17), 2147-2156. doi: http://dx.doi.org/10.1016/j.atmosenv.2010.02.010

Kinsey, J. S., M. D. Hays, Y. Dong, D. C. Williams, & R. Logan, 2011: Chemical Characterization of the Fine Particle Emissions from Commercial Aircraft Engines

during the Aircraft Particle Emissions eXperiment (APEX) 1 to 3. *Environmental Science & Technology, 45*(8), 3415-3421. doi: 10.1021/es103880d

Kinsey, J. S., M. T. Timko, S. C. Herndon, E. C. Wood, Z. Yu, R. C. Miake-Lye, et al., 2012: Determination of the emissions from an aircraft auxiliary power unit (APU) during the Alternative Aviation Fuel Experiment (AAFEX). *Journal of the Air & Waste Management Association, 62*(4), 420-430. doi: 10.1080/10473289.2012.655884

Kiselev, A., C. Wennrich, F. Stratmann, H. Wex, S. Henning, T. F. Mentel, et al., 2010: Morphological characterization of soot aerosol particles during LACIS Experiment in November (LExNo). *Journal of Geophysical Research: Atmospheres, 115*, n/a–n/a. doi: 10.1029/2009JD012635

Knaapen, A. M., P. J. A. Borm, C. Albrecht, & R. P. F. Schins, 2004: Inhaled particles and lung cancer. Part A: Mechanisms. *International Journal of Cancer, 109*(6), 799-809. doi: 10.1002/ijc.11708

Kolaitis, L. N., F. J. Bruynseels, R. E. Van Grieken, & M. O. Andreae, 1989: Determination of methanesulfonic acid and non-sea-salt sulfate in single marine aerosol particles. *Environmental Science & Technology, 23*(2), 236-240. doi: 10.1021/es00179a018

Kulkarni, P., P. A. Baron, & K. Willeke. (2011). *Aerosol Measurement: Principles, Techniques, and Applications* (3rd ed.): John Wiley & Sons.

Lack, D., H. Moosmüller, G. McMeeking, R. Chakrabarty, & D. Baumgardner, 2014: Characterizing elemental, equivalent black, and refractory black carbon aerosol particles: a review of techniques, their limitations and uncertainties. *Analytical and Bioanalytical Chemistry, 406*(1), 99-122. doi: 10.1007/s00216-013-7402-3

Lamb, D., & J. Verlinde. (2011). *Physics and Chemistry of Clouds*. Cambridge, UK: Cambridge University Press.

Lambe, A. T., A. T. Ahern, J. P. Wright, D. R. Croasdale, P. Davidovits, & T. B. Onasch, 2015: Oxidative aging and cloud condensation nuclei activation of laboratory combustion soot. *Journal of Aerosol Science, 79*, 31-39. doi: http://dx.doi.org/10.1016/j.jaerosci.2014.10.001

Lee, B. P., Y. J. Li, R. C. Flagan, C. Lo, & C. K. Chan, 2013: Sizing Characterization of the Fast-Mobility Particle Sizer (FMPS) Against SMPS and HR-ToF-AMS. *Aerosol Science and Technology, 47*(9), 1030-1037. doi: 10.1080/02786826.2013.810809

Lee, D. S., D. W. Fahey, P. M. Forster, P. J. Newton, R. C. N. Wit, L. L. Lim, et al., 2009: Aviation and global climate change in the 21st century. *Atmospheric Environment, 43*, 3520-3537. doi: 10.1016/j.atmosenv.2009.04.024

Li, Y., J. Xue, K. Johnson, T. Durbin, M. Villela, L. Pham, et al., 2014: Determination of Suspended Exhaust PM Mass for Light-Duty Vehicles. doi: 10.4271/2014-01-1594

Liati, A., B. T. Brem, L. Durdina, M. Vögtli, Y. Arroyo Rojas Dasilva, P. Dimopoulos Eggenschwiler, et al., 2014: Electron Microscopic Study of Soot Particulate Matter Emissions from Aircraft Turbine Engines. *Environmental Science & Technology, 48*(18), 10975-10983. doi: 10.1021/es501809b

Lighty, J. S., J. M. Veranth, & A. F. Sarofim, 2000: Combustion Aerosols: Factors Governing Their Size and Composition and Implications to Human Health. *Journal of the Air & Waste Management Association, 50*, 1565-1618. doi: 10.1080/10473289.2000.10464197

Liscinsky, D. S., A. Bhargava, M. B. M.B. Colket, D. C. D.C. Hautman, H. H. Hollick, & B. True, 2010: Effect of particle sampling technique and transport on particle penetration at the high temperature and pressure conditions found in gas turbine combustors and engines. *NASA contractor report, NASA/CR-2010-NNC07CB03C*.

Liu, D.-Y., K. A. Prather, & S. V. Hering, 2000: Variations in the Size and Chemical Composition of Nitrate-Containing Particles in Riverside, CA. *Aerosol Science and Technology, 33*(1-2), 71-86. doi: 10.1080/027868200410859

Liu, Z., J. Swanson, D. B. Kittelson, & D. Y. H. Pui, 2012: Comparison of Methods for Online Measurement of Diesel Particulate Matter. *Environmental Science & Technology, 46*(11), 6127-6133. doi: 10.1021/es3003537

Liu, Z. G., V. N. Vasys, M. E. Dettmann, J. J. Schauer, D. B. Kittelson, & J. Swanson, 2009: Comparison of Strategies for the Measurement of Mass Emissions from Diesel Engines Emitting Ultra-Low Levels of Particulate Matter. *Aerosol Science and Technology, 43*(11), 1142-1152. doi: 10.1080/02786820903219035

Lobo, P., L. Durdina, G. J. Smallwood, T. Rindlisbacher, F. Siegerist, E. A. Black, et al., 2015: Measurement of Aircraft Engine Non-Volatile PM Emissions: Results of the Aviation - Particle Regulatory Instrument Demonstration Experiment (A-PRIDE) 4 Campaign. *Aerosol Science and Technology*, 00-00. doi: 10.1080/02786826.2015.1047012

Lobo, P., D. E. Hagen, & P. D. Whitefield, 2011: Comparison of PM emissions from a commercial jet engine burning conventional, biomass, and fischer-tropsch fuels. *Environmental Science and Technology, 45*(24), 10744-10749. doi: 10.1021/es201902e

Lobo, P., D. E. Hagen, & P. D. Whitefield, 2012: Measurement and analysis of aircraft engine PM emissions downwind of an active runway at the Oakland International Airport. *Atmospheric Environment, 61*, 114-123. doi: http://dx.doi.org/10.1016/j.atmosenv.2012.07.028

Lobo, P., D. E. Hagen, P. D. Whitefield, & D. J. Alofs, 2007a: Physical Characterization or Aerosol Emissions from a Commercial Gas Turbine Engine. *Journal of Propulsion and Power, 23*, 919-929. doi: 10.2514/1.26772

Lobo, P., P. Whitefield, D. Hagen, S. Herndon, J. Jayne, E. Wood, et al., 2007b: The Development of Exhaust Speciation Profiles for Commercial Jet Engines, Final Report. *Contract*(04-344).

Lushnikov, A. A. (2010). Introduction to Aerosols *Aerosols - Science and Technology* (pp. 1-41): Wiley-VCH Verlag GmbH & Co. KGaA.

Ma, X., C. D. Zangmeister, J. Gigault, G. W. Mulholland, & M. R. Zachariah, 2013: Soot aggregate restructuring during water processing. *Journal of Aerosol Science, 66*, 209-219. doi: 10.1016/j.jaerosci.2013.08.001

Mandelbrot, B. (1982). *The fractal geometry of nature*: W.H. Freeman.

Maricq, M. M., 2007: Coagulation dynamics of fractal-like soot aggregates. *Journal of Aerosol Science, 38*, 141-156. doi: 10.1016/j.jaerosci.2006.11.004

Maricq, M. M., & N. Xu, 2004: The effective density and fractal dimension of soot particles from premixed flames and motor vehicle exhaust. *Journal of Aerosol Science, 35*, 1251-1274. doi: 10.1016/j.jaerosci.2004.05.002

Martins, J. V., P. Artaxo, C. Liousse, J. S. Reid, P. V. Hobbs, & Y. J. Kaufman, 1998: Effects of black carbon content, particle size, and mixing on light absorption by aerosols from biomass burning in Brazil. *Journal of Geophysical Research: Atmospheres, 103*(D24), 32041-32050. doi: 10.1029/98JD02593

Masiol, M., & R. M. Harrison, 2014: Aircraft engine exhaust emissions and other airport-related contributions to ambient air pollution: A review. *Atmospheric Environment, 95*, 409-455. doi: http://dx.doi.org/10.1016/j.atmosenv.2014.05.070

Mathis, U., M. Mohr, R. Kaegi, A. Bertola, & K. Boulouchos, 2005: Influence of Diesel Engine Combustion Parameters on Primary Soot Particle Diameter. *Environmental Science & Technology, 39*, 1887-1892. doi: 10.1021/es049578p

Mauney, T., F. Adams, & M. R. Sine, 1984: Carbonaceous Particles in the Atmosphere 1983 Laser microprobe mass spectrometry of environmental soot particles. *Science of The Total Environment, 36*, 215-224. doi: http://dx.doi.org/10.1016/0048-9697(84)90269-9

Mazaheri, M., T. E. Bostrom, G. R. Johnson, & L. Morawska, 2013: Composition and Morphology of Particle Emissions from in-use Aircraft during Takeoff and Landing. *Environmental Science & Technology, 47*, 5235-5242. doi: 10.1021/es3046058

Mazaheri, M., G. R. Johnson, & L. Morawska, 2011: An inventory of particle and gaseous emissions from large aircraft thrust engine operations at an airport. *Atmospheric Environment, 45*, 3500-3507. doi: 10.1016/j.atmosenv.2010.12.012

Miljevic, B., N. C. Surawski, T. Bostrom, & Z. D. Ristovski, 2012: Restructuring of carbonaceous particles upon exposure to organic and water vapours. *Journal of Aerosol Science, 47*, 48-57. doi: 10.1016/j.jaerosci.2011.12.005

Miller, R. A., 1997: Thermal barrier coatings for aircraft engines: history and directions. *Journal of Thermal Spray Technology, 6*(1), 35-42. doi: 10.1007/BF02646310

Minnis, P., D. F. Young, D. P. Garber, L. Nguyen, W. L. Smith, & R. Palikonda, 1998: Transformation of contrails into cirrus during SUCCESS. *Geophysical Research Letters, 25*(8), 1157-1160. doi: 10.1029/97GL03314

Myhre, G., D. Shindell, F.-M. Bréon, W. Collins, J. Fuglestvedt, J. Huang, et al., 2013: Anthropogenic and Natural Radiative Forcing. In: *Climate Change 2013: The Physical Science Basis. Contribution of Working Group I to the Fifth Assessment Report of the Intergovernmental Panel on Climate Change* [Stocker, T.F., D. Qin, G.-K. Plattner, M. Tignor, S.K. Allen, J. Boschung, A. Nauels, Y. Xia, V. Bex and P.M. Midgley (Eds.)]. Cambridge University Press, Cambridge, United Kingdom and New York, NY, USA.

NIOSH, 2003: Method 5040 in the NIOSH Manual of Analytical Methods (NMAM): Elemental Carbon (Diesel Particulate).

Okada, S., C.-B. Kweon, J. C. Stetter, D. E. Foster, M. M. Shafer, C. G. Christensen, et al. (2003). Society of Automotive Engineering, Inc.

Olfert, J. S., & N. Collings, 2005: New method for particle mass classification—the Couette centrifugal particle mass analyzer. *Journal of Aerosol Science, 36*, 1338-1352. doi: 10.1016/j.jaerosci.2005.03.006

Olfert, J. S., J. P. R. Symonds, & N. Collings, 2007: The effective density and fractal dimension of particles emitted from a light-duty diesel vehicle with a diesel oxidation catalyst. *Journal of Aerosol Science, 38*, 69-82. doi: 10.1016/j.jaerosci.2006.10.002

Onasch, T. B., J. T. Jayne, S. Herndon, D. R. Worsnop, R. C. Miake-Lye, I. P. Mortimer, et al., 2009: Chemical Properties of Aircraft Engine Particulate Exhaust Emissions. *Journal of Propulsion and Power, 25*, 1121-1137. doi: 10.2514/1.36371

Pagan, I., D. L. Costa, J. K. McGee, J. H. Richards, J. A. Dye, & M. J. Dykstra, 2003: Metals Mimic Airway Epithelial Injury Induced by in Vitro Exposure to Utah Valley Ambient Particulate Matter Extracts. *Journal of Toxicology and Environmental Health, Part A, 66*(12), 1087-1112. doi: 10.1080/15287390390213908

Park, K., F. Cao, D. B. Kittelson, & P. H. McMurry, 2003a: Relationship between Particle Mass and Mobility for Diesel Exhaust Particles. *Environmental Science & Technology, 37*, 577-583. doi: 10.1021/es025960v

Park, K., D. B. Kittelson, & P. H. McMurry, 2003b: A closure study of aerosol mass concentration measurements: comparison of values obtained with filters and by direct measurements of mass distributions. *Atmospheric Environment, 37*(9–10), 1223-1230. doi: http://dx.doi.org/10.1016/S1352-2310(02)01016-6

Park, K., D. B. Kittelson, M. R. Zachariah, & P. H. McMurry, 2004: Measurement of Inherent Material Density of Nanoparticle Agglomerates. *Journal of Nanoparticle Research, 6*, 267-272. doi: 10.1023/B:NANO.0000034657.71309.e6

Pastor, S. H., J. O. Allen, L. S. Hughes, P. Bhave, G. R. Cass, & K. A. Prather, 2003: Ambient single particle analysis in Riverside, California by aerosol time-of-flight mass spectrometry during the SCOS97-NARSTO. *Atmospheric Environment, 37, Supplement 2*, 239-258. doi: http://dx.doi.org/10.1016/S1352-2310(03)00393-5

Peck, J., M. T. Timko, Z. Yu, H.-W. Wong, S. C. Herndon, P. E. Yelvington, et al., 2012: Measurement of Volatile Particulate Matter Emissions From Aircraft Engines Using a Simulated Plume Aging System. *Journal of Engineering for Gas Turbines and Power, 134*(6), 061503-061503. doi: 10.1115/1.4005988

Petzold, A., M. Fiebig, L. Fritzsche, C. Stein, U. Schumann, C. W. Wilson, et al., 2005: Particle emissions from aircraft engines – a survey of the European project PartEmis. *Meteorologische Zeitschrift, 14*, 465-476. doi: 10.1127/0941-2948/2005/0054

Petzold, A., R. Marsh, M. Johnson, M. Miller, Y. Sevcenco, D. Delhaye, et al., 2011: Evaluation of Methods for Measuring Particulate Matter Emissions from Gas Turbines. *Environmental Science & Technology, 45*(8), 3562-3568. doi: 10.1021/es103969v

Petzold, A., J. A. Ogren, M. Fiebig, P. Laj, S.-M. Li, U. Baltensperger, et al., 2013: Recommendations for reporting "black carbon" measurements. *Atmos. Chem. Phys., 13*, 8365-8379. doi: 10.5194/acp-13-8365-2013

Petzold, A., & F. P. Schröder, 1998: Jet Engine Exhaust Aerosol Characterization. *Aerosol Science and Technology, 28*(1), 62-76. doi: 10.1080/02786829808965512

Platt, S. M., I. El Haddad, A. A. Zardini, M. Clairotte, C. Astorga, R. Wolf, et al., 2013: Secondary organic aerosol formation from gasoline vehicle emissions in a new mobile environmental reaction chamber. *Atmos. Chem. Phys., 13*(18), 9141-9158. doi: 10.5194/acp-13-9141-2013

Popovicheva, O. B., & A. M. Starik, 2007: Aircraft-generated soot aerosols: Physicochemical properties and effects of emission into the atmosphere. *Izvestiya, Atmospheric and Oceanic Physics, 43*(2), 125-141. doi: 10.1134/S0001433807020016

Pruppacher, H. R., & J. D. Klett. (2010a). The Atmospheric Aerosol and Trace Gases *Microphysics of Clouds and Precipitation* (Vol. 18, pp. 216-286): Springer Netherlands.

Pruppacher, H. R., & J. D. Klett. (2010b). Equilibrium Between Water Vapor, Water, Aqueous Solutions, and Ice in Bulk *Microphysics of Clouds and Precipitation* (Vol. 18, pp. 100-125): Springer Netherlands.

Qiu, C., A. F. Khalizov, B. Hogan, E. L. Petersen, & R. Zhang, 2014: High Sensitivity of Diesel Soot Morphological and Optical Properties to Combustion Temperature in a Shock Tube. *Environmental Science & Technology, 48*(11), 6444-6452. doi: 10.1021/es405589d

Rebotier, T. P., & K. A. Prather, 2007: Aerosol time-of-flight mass spectrometry data analysis: A benchmark of clustering algorithms. *Analytica Chimica Acta, 585*, 38-54. doi: 10.1016/j.aca.2006.12.009

Ris, C. (2008, 2008-10-20). U.S. EPA Health Assessment for Diesel Engine Exhaust: A Review.

Rissler, J., M. E. Messing, A. I. Malik, P. T. Nilsson, E. Z. Nordin, M. Bohgard, et al., 2013: Effective Density Characterization of Soot Agglomerates from Various Sources and Comparison to Aggregation Theory. *Aerosol Science and Technology, 47*, 792-805. doi: 10.1080/02786826.2013.791381

Rogers, F., P. Arnott, B. Zielinska, J. Sagebiel, K. E. Kelly, D. Wagner, et al., 2005: Real-Time Measurements of Jet Aircraft Engine Exhaust. *Journal of the Air & Waste Management Association, 55*, 583-593. doi: 10.1080/10473289.2005.10464651

Rudich, Y., N. M. Donahue, & T. F. Mentel, 2007: Aging of Organic Aerosol: Bridging the Gap Between Laboratory and Field Studies. *Annual Review of Physical Chemistry, 58*, 321-352. doi: 10.1146/annurev.physchem.58.032806.104432

SAE, 2013: Aerospace Information Report 6241: Procedure for the Continuous Sampling and Measurement of Non-volatile Particle Emissions from Aircraft Turbine Engines.

Scheckman, J. H., & P. H. McMurry, 2011: Deposition of silica agglomerates in a cast of human lung airways: Enhancement relative to spheres of equal mobility and aerodynamic diameter. *Journal of Aerosol Science, 42*(8), 508-516. doi: 10.1016/j.jaerosci.2011.05.003

Schindler, W., C. Haisch, H. Beck, R. Niessner, J. Eberhard, & D. Rothe, 2004: A Photoacoustic Sensor System for Time Resolved Quantification of Diesel Soot Emissions. *SAE Technical Paper*. doi: 10.4271/2004-01-0968

Schmid, O., D. E. Hagen, P. D. Whitefield, M. B. Trueblood, A. P. Rutter, & H. V. Lilenfeld, 2004: Methodology for Particle Characterization in the Exhaust Flows of Gas Turbine Engines. *Aerosol Science and Technology, 38*(11), 1108-1122. doi: 10.1080/027868290507222

Schmidt-Ott, A., 1988: New approaches to in situ characterization of ultrafine agglomerates. *Journal of Aerosol Science, 19*, 553-563. doi: 10.1016/0021-8502(88)90207-8

Schmidt-Ott, A., U. Baltensperger, H. W. Gäggeler, & D. T. Jost, 1990: Scaling behaviour of physical parameters describing agglomerates. *Journal of Aerosol Science, 21*, 711-717. doi: 10.1016/0021-8502(90)90037-X

Schumann, U., 1996: On Conditions for Contrail Formation from Aircraft Exhausts. *Meteorologische Zeitschrift / DLR, Inst. f. Physik der Atmosphäre, Report No. 44, 5*, 4-23.

Shapiro, M., P. Vainshtein, D. Dutcher, M. Emery, M. Stolzenburg, D. B. Kittelson, et al., 2012: Characterization of agglomerates by simultaneous measurement of mobility, vacuum aerodynamic diameter and mass. *Journal of Aerosol Science, 44*, 24-45. doi: 10.1016/j.jaerosci.2011.08.004

Silva, P. J., R. A. Carlin, & K. A. Prather, 2000: Single particle analysis of suspended soil dust from Southern California. *Atmospheric Environment, 34*(11), 1811-1820. doi: http://dx.doi.org/10.1016/S1352-2310(99)00338-6

Silva, P. J., D.-Y. Liu, C. A. Noble, & K. A. Prather, 1999: Size and Chemical Characterization of Individual Particles Resulting from Biomass Burning of Local Southern California Species. *Environmental Science & Technology, 33*(18), 3068-3076. doi: 10.1021/es980544p

Silva, P. J., & K. A. Prather, 2000: Interpretation of Mass Spectra from Organic Compounds in Aerosol Time-of-Flight Mass Spectrometry. *Analytical Chemistry, 72*(15), 3553-3562. doi: 10.1021/ac9910132

Snelling, D. R., G. J. Smallwood, F. Liu, Ö. L. Gülder, & W. D. Bachalo, 2005: A calibration-independent laser-induced incandescence technique for soot measurement by detecting absolute light intensity. *Applied optics, 44*(31), 6773-6785. doi: 10.1364/AO.44.006773

Sorensen, C. M., 2001: Light Scattering by Fractal Aggregates: A Review. *Aerosol Science and Technology, 35*(2), 648-687. doi: 10.1080/02786820117868

Sorensen, C. M., 2011: The Mobility of Fractal Aggregates: A Review. *Aerosol Science and Technology, 45*, 765-779. doi: 10.1080/02786826.2011.560909

Spencer, M. T., & K. A. Prather, 2006: Using ATOFMS to Determine OC/EC Mass Fractions in Particles. *Aerosol Science and Technology, 40*, 585-594. doi: 10.1080/02786820600729138

Stettler, M. E. J., J. J. Swanson, S. R. H. Barrett, & A. M. Boies, 2013: Updated Correlation Between Aircraft Smoke Number and Black Carbon Concentration. *Aerosol Science and Technology, 47*, 1205-1214. doi: 10.1080/02786826.2013.829908

Stetzer, O., B. Baschek, F. Lüönd, & U. Lohmann, 2008: The Zurich Ice Nucleation Chamber (ZINC)-A New Instrument to Investigate Atmospheric Ice Formation. *Aerosol Science and Technology, 42*(1), 64-74. doi: 10.1080/02786820701787944

Symonds, J. (2010). Calibration of Fast Response Differential Mobility Spectrometers. http://www.npl.co.uk/upload/pdf/20100608_mansa_symonds.pdf.

Terzano, C., F. Di Stefano, V. Conti, E. Graziani, & A. Petroianni, 2010: Air pollution ultrafine particles: toxicity beyond the lung. *Eur Rev Med Pharmacol Sci, 14*(10), 809-821.

Timko, M. T., T. B. Onasch, M. J. Northway, J. T. Jayne, M. R. Canagaratna, S. C. Herndon, et al., 2010a: Gas Turbine Engine Emissions—Part II: Chemical Properties of Particulate Matter. *Journal of Engineering for Gas Turbines and Power, 132*(6), 061505-061505. doi: 10.1115/1.4000132

Timko, M. T., Z. Yu, T. B. Onasch, H. W. Wong, R. C. Miake-Lye, A. J. Beyersdorf, et al., 2010b: Particulate Emissions of Gas Turbine Engine Combustion of a Fischer−Tropsch Synthetic Fuel. *Energy & Fuels, 24*(11), 5883-5896. doi: 10.1021/ef100727t

Toner, S. M., D. A. Sodeman, & K. A. Prather, 2006: Single Particle Characterization of Ultrafine and Accumulation Mode Particles from Heavy Duty Diesel Vehicles Using Aerosol Time-of-Flight Mass Spectrometry. *Environmental Science & Technology, 40*, 3912-3921. doi: 10.1021/es051455x

Touri, L., H. Marchetti, I. Sari-Minodier, N. Molinari, & P. Chanez, 2013: The airport atmospheric environment: respiratory health at work. *European Respiratory Review, 22*(128), 124-130. doi: 10.1183/09059180.00005712

TSI, 2004a: MS-Analyze software instruction manual.

TSI, I., 2004b: Series 3800 Aerosol Time-of-Flight Mass Spectrometers with Aerodynamic Focusing Lens Technology. Shoreview, MN.

Vander Wal, R. L., & V. M. Bryg, 2014: Chemistry Characterization of Jet Aircraft Engine Particulate by XPS: Results from APEX III.

Vander Wal, R. L., V. M. Bryg, & C.-H. Huang, 2014: Aircraft engine particulate matter: Macro- micro- and nanostructure by HRTEM and chemistry by XPS. *Combustion and Flame, 161*(2), 602-611. doi: http://dx.doi.org/10.1016/j.combustflame.2013.09.003

Westerdahl, D., S. A. Fruin, P. L. Fine, & C. Sioutas, 2008: The Los Angeles International Airport as a source of ultrafine particles and other pollutants to nearby communities. *Atmospheric Environment, 42*(13), 3143-3155. doi: http://dx.doi.org/10.1016/j.atmosenv.2007.09.006

Whitby, K. T., 1978: The physical characteristics of sulfur aerosols. *Atmospheric Environment (1967), 12*(1–3), 135-159. doi: http://dx.doi.org/10.1016/0004-6981(78)90196-8

Wiedensohler, A., 1988: An approximation of the bipolar charge distribution for particles in the submicron size range. *Journal of Aerosol Science, 19*, 387-389. doi: 10.1016/0021-8502(88)90278-9

Wierzbicka, A., P. T. Nilsson, J. Rissler, G. Sallsten, Y. Xu, J. H. Pagels, et al., 2014: Detailed diesel exhaust characteristics including particle surface area and lung deposited dose for better understanding of health effects in human chamber exposure studies. *Atmospheric Environment, 86*, 212-219. doi: 10.1016/j.atmosenv.2013.11.025

Wilkerson, J. T., M. Z. Jacobson, A. Malwitz, S. Balasubramanian, R. Wayson, G. Fleming, et al., 2010: Analysis of emission data from global commercial aviation: 2004 and 2006. *Atmos. Chem. Phys., 10*, 6391-6408. doi: 10.5194/acp-10-6391-2010

Williams, P. I., J. D. Allan, P. Lobo, H. Coe, S. Christie, C. Wilson, et al., 2012: Impact of Alternative Fuels on Emissions Characteristics of a Gas Turbine Engine – Part 2: Volatile and Semivolatile Particulate Matter Emissions. *Environmental Science & Technology, 46*, 10812-10819. doi: 10.1021/es301899s

Xiong, C., & S. K. Friedlander, 2001: Morphological properties of atmospheric aerosol aggregates. *Proceedings of the National Academy of Sciences, 98*, 11851-11856. doi: 10.1073/pnas.211376098

Yim, S. H. L., G. L. Lee, I. H. Lee, F. Allroggen, A. Ashok, F. Caiazzo, et al., 2015: Global, regional and local health impacts of civil aviation emissions. *Environmental Research Letters, 10*, 034001. doi: 10.1088/1748-9326/10/3/034001

Yim, S. H. L., M. E. J. Stettler, & S. R. H. Barrett, 2013: Air quality and public health impacts of UK airports. Part II: Impacts and policy assessment. *Atmospheric Environment, 67*, 184-192. doi: http://dx.doi.org/10.1016/j.atmosenv.2012.10.017

Zhang, R., A. F. Khalizov, J. Pagels, D. Zhang, H. Xue, & P. H. McMurry, 2008: Variability in morphology, hygroscopicity, and optical properties of soot aerosols during atmospheric processing. *Proceedings of the National Academy of Sciences, 105*, 10291-10296. doi: 10.1073/pnas.0804860105

Zheng, Z., T. D. Durbin, J. Xue, K. C. Johnson, Y. Li, S. Hu, et al., 2014: Comparison of Particle Mass and Solid Particle Number (SPN) Emissions from a Heavy-Duty Diesel Vehicle under On-Road Driving Conditions and a Standard Testing Cycle. *Environmental Science & Technology, 48*(3), 1779-1786. doi: 10.1021/es403578b

Zhou, C., & J. E. Penner, 2014: Aircraft soot indirect effect on large-scale cirrus clouds: Is the indirect forcing by aircraft soot positive or negative? *Journal of Geophysical Research: Atmospheres, 119*(19), 11,303-311,320. doi: 10.1002/2014JD021914